Synthesis of Novel Graphene Oxide-Based Nanocomposite for Antibiotics Removal in Water Purification

モハマド ファイズル イダハム ビン モハマド ズルキプリ

Ph.D. Thesis on

Synthesis of Novel Graphene Oxide-Based Nanocomposite for Antibiotics Removal in Water Purification

by

MOHD FAIZUL IDHAM BIN MOHD ZULKIPLI

Supervised by

Assoc. Prof. Osama Eljamal

Water and Environmental Engineering Laboratory (WEEL)
Department of Earth System Science and Technology (ESST)
Interdisciplinary Graduate School of Engineering Sciences (IGSES)
Kyushu University

Japan

September 2023

This page is intentionally left blank.

Abstract

The metabolism of antibiotics in the human body is suboptimal, leading to the eventual release of residual parent compounds into the environment and wastewater treatment facilities via excretion in urine and feces. The occurrence of these compounds in aquatic ecosystems leads to significant environmental contamination and can destabilize ecological balance by promoting the proliferation of antibiotic-resistant bacteria (ARB) and antibiotic-resistance genes (ARG), which threaten human health. Therefore, this study addressed antibiotic waste contamination in water using graphene oxide (GO) and GO nano zero-valent iron (nZVI/GO) nanocomposite. The **first project** aimed to optimize the chemical synthesis of GO based on time and material cost-saving protocols in order to produce ideal GO for treating water contaminated with ciprofloxacin (CIP) and to explore its removal conditions. The study's outcomes prove that the synthesis conditions impacted the performance of GO produced against CIP removal. Facile GO chemical synthesis was successfully developed by empirically optimizing each synthesis stage's parameters while considering the excellent CIP removal performance. CIP removal condition assessment reveals that O–GO can remove a significant portion, up to 98%, of 100 mg/L CIP when administered at a dosage of 0.6 g/L with a pH range of 5-9. Interestingly, O–GO offered the most material cost-effective of just 0.2195 JPY for 1 mg of CIP elimination. Moreover, O–GO exhibited an 83 % CIP desorption efficiency using 1M NaOH solution. The **second project** concentrated on developing the GO-precipitated nZVI nanocomposite (nZVI/GO) and assessing the impact of GO precursor on the nanocomposite's efficiency in removing Chloramphenicol (CAP) from water. The finding found that the GO precursor utilized in the fabrication of nZVI/GO nanocomposite substantially impacts its morphological characteristics and performance in CAP removal. O-GO offered a great supporter for nZVI precipitation and improved CAP removal efficiency. The 0.25 g/L dose of nZVI/O-GO nanocomposite exhibited superior removal efficiency in eliminating 100 mg/L CAP, with a maximum removal rate of 90% at a natural pH and 91% at a pH 5. Moreover, the nZVI/O–GO nanocomposite presented good CAP removal stability across a wide pH range and exceptional recyclability.

This page is intentionally left blank.

Acknowledgments

In the name of Allah, The Most Gracious and The Most Merciful.

First and foremost, all glory, absolute praise, prostrations, and supplications are due to Allah, who aided me at every stage of my endeavor and enabled me to see it through to completion.

My most profound appreciation goes to my Ph.D. supervisor, Assoc. Prof. Dr. Osama ELJAMAL for his invaluable advice, patience, continuous support, and constant encouragement throughout my doctoral study at Kyushu University (KU). His vast wisdom and wealth of experience have inspired me throughout my studies and daily life.

In addition, I would like to extend my deep appreciation to Prof. Dr. Atsuhiko Isobe and Assoc. Prof. Dr. Hooman Farzaneh for reviewing the thesis and providing insightful comments and ideas on the presented work.

I would also like to express my appreciation to all the Water and Environmental Engineering Laboratory (WEEL) members for their prompt and professional assistance whenever needed.

Moreover, I would like to express my gratitude to the Japanese Ministry of Education, Culture, Sports, Science, and Technology (MEXT) and the Japan International Cooperation Agency (JICA) for their financial support during my postgraduate studies.

I would like to offer my appreciation to my father, my wife, and my children. With their tremendous understanding and encouragement over the past few years, I can complete my study.

Finally, my sincere thank goes out to my friends and everyone who has been there for me emotionally and intellectually.

Mohd Faizul Idham

This page is intentionally left blank.

Table of Contents

List of Figures

List of Tables

Chapter 1

Introduction

1.1. Background

Water is not only necessary for environmental sustainability and the development of the country's economy, but it is also a fundamental necessity for all life on earth, including humans, animals, and plants. Water makes up 70 % of the human body's composition, making it essential for operating body system functions, including temperature regulation, blood circulation, oxygen transfer, and food digestion. Consistently consuming enough clean water may offer the essential mineral source in the body's balance and assist in eliminating harmful toxins, allowing the body to operate under ideal circumstances. Water conditions that are safe and free of biological and chemical contaminants promote public health care practices to prevent waterborne diseases such as diarrhea, acute respiratory infections, and various chronic tropical illnesses [1].

Water covers three-quarters of the earth's surface, and surface water accounts for 80 % of the world's daily water consumption. Irrigation and public supplies for daily usage make up the vast preponderance of its primary applications. According to the World Health Organization (WHO) and the United Nations Children's Fund (UNICEF), 159 million people worldwide still rely on surface water as a source of drinking water [2]. However, the safety and purity of this surface water are still in doubt, raising concerns about its use as a source of drinking water because of the extensive surface water contamination brought on by industrialization growth yearly. In Malaysia, for instance, it has been reported that 42 % of its river basins are classified as “polluted rivers,” while 11 % have been considered to be “severely polluted rivers” [3]. WHO reported that more than 2 billion people worldwide consume water from contaminated surface water for daily consumption and as a beverage, posing health threats to the population [1]. The global clean water crisis is anticipated to grow due to worsening pollution and rising demand for clean water due to population growth, urbanization, industrialization, and climate change, leading to global health, economic, and social crises [1].

Physical, chemical, biological, and radioactive contaminants are the four main categories of severe pollutants affecting drinking water contamination caused by surface water pollution. This pollution, notably chemical pollution, is one of the most crucial environmental issues, receiving significant concern all over the world. Chemical pollution in surface water has a two-pronged deleterious impact on public health and economic

development due to the continual rise in the quantity and cumulative concentration of anthropogenic, bioaccumulative, and toxic contaminants. Today's rapid industrialization and the development of numerous chemical-based products have led to the emergence of new advance contaminants such as pharmaceuticals, pesticides, and microplastics, exacerbating surface water chemical pollution and jeopardizing public health with waterborne diseases. It is grievous to report that waterborne infections caused by water pollution account for 29% of all child fatalities, or more than 2 million child deaths [4].

Antibiotics are increasingly used to prevent and treat bacterial infections in the clinical, animal husbandry, and agricultural sectors. Nevertheless, its usage that contaminates surface water with antibiotics is still inadequately addressed. Many reports worldwide reveal the release of antibiotic residues and the presence of antibiotics at alarming concentrations in surface water [5]–[8]. The widespread use of antibiotics and the inefficient handling of their waste in the healthcare and pharmaceutical industries cause antimicrobial resistance (AMR), adversely affecting health and treatment costs [9]. Untreated antibiotic waste released into the environment can infiltrate wastewater systems and adversely affect microbial populations and ecosystems. As a consequence, antibiotic-resistance genes (ARG) and antibiotic-resistant bacteria (ARB) are formed, creating a habitat in the wastewater treatment system [7], [10], [11]. Its accumulation from pathogenic and non-pathogenic bacteria in the microbial population that forms the resistome can promote the emergence of novel waterborne infectious diseases that eventually lead to hazardous global epidemics, threatening the universal health system [6].

One of the essential humanitarian goals is consistent access to hygienic and economical water, which is still a critical worldwide concern in the 21st century. Responding to the emerging threats in preserving clean water resources and decontaminating polluted water resources is imperative in the era of rapid industrialization growth to ensure the continuity of life and good health for the present and future generations. All parties need to play a role and participate in overcoming this water pollution issue, whether at the preservation, treatment, or conservation levels. Hence, research from the materials engineering field can also contribute to resolving this global issue by delivering a comprehensive study of functional materials to remove impurities from contaminated water sources.

1.2. Emerging contaminants

1.2.1. Definition

Emerging contaminants (ECs) are a phrase often used in the water quality domain to describe pollutants detected in the environment [8], [12]. It is also known as contaminants of emerging concerns (CECs) in some publications and scholarly articles. ECs are classified as any artificial or natural chemicals or microbes that are often not strictly controlled and regulated under present environmental legislation but whose existence can potentially affect human health and environmental ecology adversely [13], [14]. Chemicals nowadays are necessary for contemporary living, allowing contaminants to emerge and reach people through new sources or paths. It has been estimated that over 80,000 chemicals are manufactured and consumed only in the United States (US) [15]. These hazardous chemicals can flow and remain in wastewater and elsewhere because water treatment facilities are typically not designed to eliminate them [16], [17]. This situation raises community consciousness regarding the harm of releasing chemical substances into the environment.

1.2.2. Classification of emerging contaminants

Generally, ECs increasingly prevalent in the aqueous environment can be classified into the following categories [18].

I. Human and veterinary pharmaceuticals (Antibiotics, vaccines, human blood plasma fractions, prescription medicines, and steroid hormones).

II. Artificial chemicals (Food additives, household cleaning products, and antimicrobial substances)

III. Personal care products (cosmetics, surfactants, and domestic biocides).

IV. Disinfection agents (Nitrosamine, trihalomethanes, and halo acetic acids).

V. Biocides and their derivatives (pesticides [plants and agricultural preventive agents])

VI. Algal toxins (toxic discharged from some algae: Cyanotoxins, microcystin)

VII. Chemical and bioterrorism contraptions (Biological and Chemical weapons).

Those compounds are all categorized as ECs because of no comprehensive standards and the scarcity of toxicological information [19]. Some types of these ECs are identified as carcinogens due to their ability to disrupt endocrine systems and potentially trigger other detrimental processes [14]. The ECs are generated from various sources, including hospital wastewater, agricultural and urban runoff, daily household products, discharges from industrial effluents, and wastewater treatment plant effluents [20]. These omnipresent toxins can enter the water cycle after being released as waste by runoff directly flowing into surface water, through effluent discharge, or as groundwater that seeps and infiltrates, which subsequently enters the public water supply system.

1.2.3. Water pollution by emerging contaminants

Prior communities traditionally did not concern about the effects of ECs pollution on the environmental water due to the lack of knowledge and exposure regarding the long-term risk to the ecosystem. Formerly, there was a stigma in the community that diluting was the answer to this chemical contamination. However, this perception is wildly erroneous, so ECs' water pollution has recently become a pressing concern. The existence of this contaminant may be identified not just in water but can also be detected in submerged sediments.

Untreated water has been reported to contain more than 121 uncontrolled chemicals and pathogenic microorganisms, with at least 25 discovered in water treatment facilities [18]. Many variables influence the concentration of ECs in water, including the pattern of water usage and consumption per capita, population density, and the quality of water drainage. Even though certain ECs are detected in low concentrations (ng/L to µg/L), prolonged exposure and their high cumulative concentrations can adversely affect ecosystem health and sustainability [19]. The release and persistence of these ECs in the aquatic environment without any specific treatment expose fish and other aquatic species to peril and presents a risk to non-aquatic species through bioaccumulation in the food chain [21]–[23]. For instance, some studies have linked exposure to ECs in water sources to developmental abnormalities, reproductive disorders, and the disruption of endocrine systems [7], [24]–[27].

In conclusion, water pollution with ECs is a complex and pressing issue requiring an immediate response. Since ECs are extraordinarily persistent and can sustainably remain in an aqueous environment, it is challenging to eliminate the contaminant with standard water treatment or wastewater treatment [28]. Moreover, conventional water treatment plants are not designated to remove this contaminant. Consequently, developing new strategies and technologies for managing and treating these ECs thoroughly in water bodies is essential.

1.3. Pharmaceutical contamination.

1.3.1. Pharmaceuticals in human civilization: A brief history.

Records of medicinal preparations based on plants, animals, or minerals found in ancient Chinese, Hindu, and Mediterranean civilizations are the earliest pharmaceutical records in the world [29]. In the 28th century BC, the legendary emperor Shennong wrote an herbal compendium describing the antifever capabilities of medicinals derived from the *Dichroa Febrifuga* plant species [29]. Scientists and pharmacists at the alchemy school in Alexandria developed various inorganic compounds, including lead carbonate, arsenic, and mercury, as medicinal agents in the 2nd century BC, demonstrating the rapid evolution of pharmaceutical product innovation in Egypt [30]. Nevertheless, creating medical agents with these compounds was too hazardous to employ. The pharmaceutical practice began proliferating in the West after the dark and the middle eras in the 16th century AD. In 1546, the first pharmacopeia, or compendium of medicinal preparations and their constituent parts, was published in Germany. Anesthetics are the earliest recorded modern pharmaceuticals where morphine, ether, chloroform, and cocaine were first used in 1804, 1842, 1847, and 1860 respectively [30]. Later, in 1865, phenol (carbolic acid) was introduced to prevent infection by medical scientist Joseph Lister [29].

1.3.2. Pharmaceutical definition

Pharmaceuticals are chemicals used for human or animal health care, such as diagnosis, prophylaxis, treatment, and disease recuperation [30]. [30]. In addition, it is also used to recover, rectify, or alter organic functions [31]. Antibiotics, fractions of human blood

plasma, vaccines, synthetic vitamins, medicines, and steroid hormones can be categorized as pharmaceutical products [29].

1.3.3. Sources of most pharmaceutical pollution.

The extensive application of pharmaceutical by-products in human life and animal husbandry has detrimental environmental implications, categorizing it as one of the ECs. Most pharmaceutical active compounds reach the aquatic ecosystem through various anthropogenic and natural sources, either directly or indirectly [31]. Hospital effluents, pharmaceutical industrial discharges, and effluent released from conventional wastewater treatment plants are examples of direct sources of pharmaceutical pollution in environmental water, while waste dumpsites and septic tanks are examples of indirect sources. Nonetheless, hospital wastewater is recorded as a significant source of pharmaceutical metabolites that flow into the environment [32].

1.3.4. Pharmaceutical pollution in water

In addition to directly disposing of medication waste, human and animal excrement are the principal pathway for migrating pharmaceutical pollutants into the aqueous environment solution. While this active pharmaceutical compound undergoes metabolic activity when ingested, the body does not entirely metabolize it [33]. These active compounds eventually reach the human excretory system and are released into the environment via urine and feces [33]. These active pharmaceutical compounds can persist in the water for an extended period because most of these compounds have extremely low octanol-to-water partition coefficients (log K_{ow} <1), making them extraordinarily polar and very soluble in water [20], [34].

The existence of pharmaceutical ECs in natural water and urban wastewater raises concerns for environmental experts worldwide because traditional wastewater treatment plants cannot effectively remove pharmaceutical pollutants. Koumaki et al. [35] reported that treated sewage sludge contains various ECs, such as antibiotics. Cabeza et al. [36] analyzed treated wastewater in Barcelona, Spain, and found 38 pharmaceuticals. This finding confirms that wastewater treatment facilities are unable to cope with pollution brought on by ECs. The detection of ECs with a high concentration in the water sample suggests that the release of treated wastewater from the water treatment facility is the

source and cause of the EC's spread into the environment [37]. This situation leads to a chain of pollution in the environment aqueous and further threatens human drinking water sources' ecological stability and safety.

1.4. Antibiotics

1.4.1. Definition of antibiotics

Antibiotics are antimicrobial substances used on humans and animals to prevent or treat certain bacterial or microorganism infections [38]. Antibiotics' disease prevention and treatment mechanism is divided into two: directly killing bacteria and inhibiting their growth and their recurrence from spreading throughout the body system [39]. Some antibiotics are inappropriate for people with specific health conditions, pregnant women, or lactating mothers. Unnecessary antibiotic consumption or excessive consumption without following the recommended dosage does not guarantee good health and may even have adverse side effects for the user [40], [41]. There are several ways to use antibiotics, including oral ingestion and topical application (e.g., eye and ear drops). Antibiotics may be administered intravenously or by injection for more severe infections [39].

1.4.2. Overview of antibiotics in water pollution

Antibiotics are medications of either natural or synthetic origin that can kill (bactericide) or impede bacteria growth. Introducing antibiotics into therapeutic use is often regarded as the most remarkable medical breakthrough of the 21st century. China is recorded as the world's leading producer and consumer of antibiotics [40]. Antibiotic usage grew by 65% globally between 2000 and 2015, and its total usage is predicted to rise by 202% globally from 2015 to 2030 [42]. The continuous increase in antibiotic consumption would be disastrous for the ecosystem if no regulatory reforms and appropriate measures are implemented to reduce the harmful impact of antibiotic waste discharge into the environment.

Antibiotics can be released into the aquatic environment in their pure state or as metabolites from various potential sources, such as aquaculture, industry, hospitals, animal breeding practices, and human and animal excreta [43]. For instance, the presence of various antibiotics, such as amoxicillin, caffeine, chloramphenicol, ciprofloxacin,

dexamethasone, nitrofurazone, and sulfamethoxazole, has been reported in surface water in some areas of Malaysia. Ciprofloxacin and chloramphenicol were the most commonly detected antibiotics in these areas [6]. Unfortunately, conventional wastewater treatment plants cannot remove antibiotic residues that ultimately induce the discharge of this contaminant into the aqueous environment [41]. Antibiotics are able to be wholly degraded into poisonous compounds and incredibly bioactive in the environment, potentially contaminating the aquatic and terrestrial food chains [40]. This unfavorable circumstance jeopardizes the ecosystem's safety and the environment's health.

Due to the rampant abuse of antibiotics and their widespread usage globally, antibiotic resistance has rapidly increased, making it more difficult to treat certain infections caused by ARGs or ARBs [44]. Increased antibiotic usage positively correlates with the high bulk of resistant microbes. Drug-resistant infections already account for more than 700,000 annual fatalities, and this figure is anticipated to rise to 10 million by 2050 if no nourished efforts are implemented to eradicate antibiotics and reduce the content of AMR in environmental water [40], [44]–[46].

1.4.3. Antibiotic resistance development and its implications

Antibiotic resistance develops when a given prescription loses its ability to inhibit pathogenic bacteria' recurrence effectively [44]. When bacteria replicate even in the presence of antibiotics at therapeutic dosages, these bacteria are called antibiotic-resistance bacteria [47]. The presence of antibiotics in the body system is to annihilate bacteria. However, bacteria tend to develop resistance naturally toward antibiotics assaults, and this resistance process occurs through gene-level mutations [44], [47]. Usually, antibiotics can destroy most bacteria in a colony, but genetically mutated bacterial colonies resist their effectiveness. These bacterial colonies can accumulate many resistance properties over time and resist various classes of antibiotics [43]. Resistance may develop with different structurally corresponding substances with identical chemical structures [44], [47].

Antibiotic-resistant microorganisms (superbugs) have emerged as a global threat, leading to an increasing number of life-threatening infections and high mortality rates [47]. World Health Organization (WHO) has cautioned that infections will become more prevalent

in the post-antibiotic decade and may even be lethal if the antibiotic resistance crisis is not addressed [48]. Globally, more individuals are killed by multidrug-resistant bacteria, with 63,000 American patients dying annually from bacterial infections and an estimated 25,000 patients dying from ARBs in Europe [47]. The estimated costs of ARB infections might lead to higher healthcare expenses and lost productivity.

1.4.4. Classification of antibiotics

Antibiotics often exhibit comparable potency, toxicity, and potential allergenic tendencies within the systemic class. Hundreds of different antibiotic varieties can be classified based on certain elements. Most can be classified into 7 groups, as shown in Table 1.1. Classifying antibiotics is essential for determining the appropriate treatment for bacterial infections. Understanding the various groups can also aid in predicting possible side effects and medication interactions.

Table 1.1. Classification of antibiotics and their use.

Group	Examples	Use
Penicillins	Penicillin, amoxicillin, co-amoxiclav, flucloxacillin, and phenoxymethylpenicillin	It is commonly employed for the treatment of various infections, such as cutaneous infections, respiratory tract infections, and urogenital infections.
Cephalosporins	Cephalexin	This antibiotic is commonly used to treat diseases, even severe conditions like sepsis and meningitis.
Aminoglycosides	Gentamicin and tobramycin	These medications are exclusively administered in hospitals to treat severe infections like sepsis. However, they may elicit adverse effects, including renal and auditory impairment. The injection is the most common method of administration, but specific ear and eye infections may also be treated with drops.

Tetracyclines	Tetracycline, doxycycline, and lymecycline	The antibiotic exhibits efficacy in addressing a range of infectious diseases, albeit its predominant application pertains to cutaneous disorders such as acne and rosacea.
Macrolides	Azithromycin, erythromycin, and clarithromycin	The medicines effectively address respiratory infections affecting the lungs and chest. It may be an option for individuals with an allergy to penicillin or those grappling with resistant bacteria.
Fluoroquinolones	Ciprofloxacin and levofloxacin	Used to treat various infections, primarily used to treat respiratory and urinary tract infections. The adverse effects of these antibiotics are significant.
Others	Chloramphenicol, fusidic acid, nitrofurantoin, and trimethoprim	Chloramphenicol is suggested for ocular and otic infections, while fusidic acid is employed for treating cutaneous and ocular infections. Nitrofurantoin and trimethoprim are frequently employed for the treatment of urinary tract infections.

1.4.5. Ciprofloxacin and water contamination: Overview and its contamination pathway.

Ciprofloxacin (CIP, $C_{17}H_{18}FN_3O_3$) is one of the most often used antibiotics for bacterial disease prevention and treatment in humans and animals. It was invented in 1983 by Bayer A.G. and was finally approved in 1987 by the United States Food and Drug Administration (USFDA) [38], [49]. CIP is a broad-spectrum antibiotic prescription of the fluoroquinolone family (FQs) with a generic chemical structure identical to that depicted in Figure 1.1 [50]. It treats bacterial infections in clinical practice and has exceptional antibacterial activity and favorable pharmacokinetic properties. CIP is effective against various bacterial illnesses, including specific skin, bone, and soft tissue infections, upper and lower respiratory infections, urinary tract infections, pneumonia, sexually transmitted diseases (such as gonorrhea and chancroid), anthrax, plague, and

salmonellosis [51]. Its versatility in aiding disease treatment makes it recommended by the WHO as second-line tuberculosis (TB) treatment medication [39], [44].

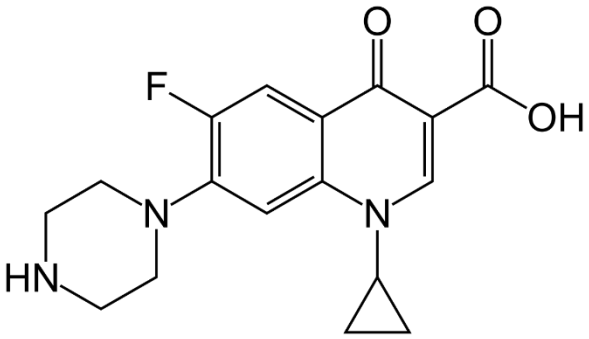

Figure 1.1. Chemical structure of ciprofloxacin

While there is no doubting the benefits of this antibiotic in treating various bacterial infections, using it may have adverse side effects, particularly if it is not taken according to the guidelines or misused. Some possible symptoms of its mild side effects include nausea, diarrhea, mild vertigo, headaches, or sleep difficulties. Moreover, using this antibiotic may result in more severe side effects, such as abnormal bruising or bleeding and symptoms of kidney and liver problems [38]. Furthermore, CIP may raise the risk of developing tendinitis, a condition characterized by the liquefaction of connective tissue between bone and muscle or tendon rupture. Also, its usage raises the possibility of nerve damage and muscular weakening [39].

CIP has an average half-life of 4 hours in the body system while 6 hours for people aged 60 years and above [41]. Between 40% and 50% of CIP is excreted from the body through urine as an unaltered medication. Approximately 20% to 35% of CIP from an oral dose is excreted in the feces [41]. Eventually, urine and feces carrying CIP enter the sewage system and threaten the microbial ecology [43]. Wastewater from hospitals had CIP concentrations between 30 and 100 mg/L [45], whereas industrial wastewater had concentrations between 2.45 x 10^4 mg/L and 6.34 x 10^4 mg/L [52]. Since CIP is a biologically active compound, its persistent discharge into environmental water sources can promote AMR formation, raising concerns and endangering global health security.

1.4.6. Chloramphenicol and water contamination: Overview and its contamination pathway.

Chloramphenicol (CAP, $C_{11}H_{12}C_{l2}N_2O_5$) is a broad-spectrum antibiotic effective against anaerobic, gram-positive, and gram-negative bacteria [53]. It was first extracted from *Streptomyces Venezuelae* in 1947, and later in 1948, it was first introduced into clinical practice [54]. CAP is used preemptively to prevent surgical wound infections because of its antibacterial and protein synthesis inhibitor properties. It is also often used for managing and treating superficial eye infections such as otitis externa and bacterial conjunctivitis. In addition, it is commonly used to treat typhoid and cholera and to cure more severe and life-threatening illnesses such as those brought on by *Haemophilus* influenza [55]. Figure 1.2 depicts the chemical structure of the organochlorine compound CAP, which consists of a nitrobenzene ring, an amide link, and two alcohol functional groups.

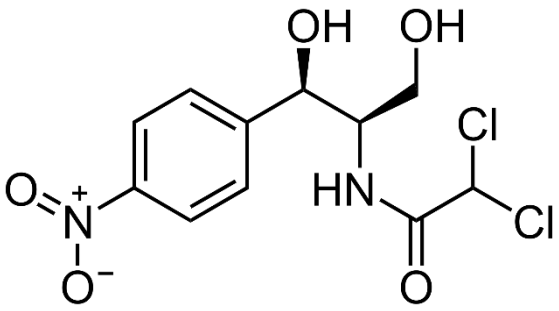

Figure 1.2. Chemical structure of chloramphenicol

CAP is classified in the antimicrobial class, working by inhibiting the recurrence of bacteria. The therapeutic mechanism involves CAP diffusing through the bacterial cell wall and reversibly binding to the bacterial 50S ribosomal subunit [47]. The binding interferes with peptidyl transferase activity, stemming amino acids from being transferred to the expanding peptide chain and preventing the formation of peptide bonds. Consequently, bacterial protein synthesis can be impeded, halting their replicating ability [47], [56].

Even though the many benefits exhibited by CAP in treating harmful diseases, its abuse, systemic intake, and long-term exposure draw hematological severe adverse effects such

as aplastic anemia, which can be fatal [57]. In addition, it may also induce several other unfavorable side effects, such as neurotoxicity, severe metabolic acidosis, ototoxicity, gastrointestinal problems, and bone marrow suppression [58], [59].

Due to the impressive performance of CAP, it is extensively employed in human and veterinary medicine. Like other antibiotics, CAP is not entirely metabolized and excreted through urine and feces. Hospital wastewater dominates the entry of CAP into the aquatic environment, with CAP concentrations in this effluent reaching several milligrams per liter [55], [60]. Unfortunately, due to improper use and inappropriate disposal, CAP is also detected in surface water, groundwater, and even drinking water, which is detrimental to human health. CAP has been detected in surface water with concentrations ranging from 30-80 ng/L and 0.6–11.2 µg/L in Kenya and China, respectively [61]. Moreover, CAP was found in sewage effluent treatment facilities in Germany and China, with concentrations of 0.56 µg/L and 47 µg/L, respectively [61]. In Tunisia, CAP was also detected in saltwater. CAP was also detected in urine samples from toddlers and pregnant women in eastern China [55], [60]. Due to its low cost, high efficiency, and good pharmacokinetic properties, the increasing global usage of CAP increases the annual cumulative concentration of CAP pollution. Unfortunately, CAP cannot be efficiently removed using standard water treatment facilities owing to its limited biodegradability. The excessive presence of chloramphenicol in water treatment systems raises the amount of chloramphenicol resistance genes, ultimately endangering ecological stability and public health.

1.5. nZVI

1.5.1. Brief Contextual Information of nZVI

Nanoscale zero-valent iron is among the most prevalent nanomaterials for environmental water purification in America and Europe because of its relative natural abundance and lesser toxicity [62]. Zero-valent iron (ZVI) particles with a 1 to 100 nm diameter are known as nanoscale ZVI (nZVI) [24]. Compared to its microscale ZVI equivalent, nZVI is more versatile by exhibiting a unique core-shell structure, stronger reactivity, and greater mobility toward various pollutants [63]. In addition, nanoscale nZVI particles have a greater specific surface area (SSA), providing more active sites that are also

advantageous for environmental applications [63]–[65]. nZVI has recently emerged as a promising nanomaterial to remove widespread contaminants from aqueous solutions. Therefore, the potential of nZVI has been studied more thoroughly until now to be employed in the sector of wastewater effluent purification polluted with contaminants based on heavy metals, pharmaceuticals, and halogenated organic compounds [28], [66]–[69].

1.5.2. Characteristics of nZVI

The nanoscale effect led to increased susceptibility to the oxidation of reactive nZVI particles [68]. Therefore, each nZVI comprises two distinct structures, as shown in Figure 1.3(a): the core and unique outer shell structures enveloping the individual core. Fe^0 makes up the core of the nZVI particle, while iron oxides like ferrous oxide (FeO), ferric oxide (Fe_2O_3), ferrous ferric oxide (Fe_3O_4), and iron hydroxides like ferrihydrite (FeOOH) make up the exterior surface of the particle core [70]. The natural thickness of the iron oxide layer is estimated to be in the range of 2–4 nm based on the standard iron oxidation pathway [71]. This oxide layer plays a role in reducing the rate of the nZVI oxidation process when exposed to the air. Nevertheless, the nZVI particles interact through magnetic forces, electrostatic attraction, and Van der Waals interactions, causing them to aggregate, form chain structures, and agglomerate [72], [73]. The structure of nZVI particles in their natural state can be seen in Figure 1.3 (b). These nZVI particles have sizes on the nanometer scale, between 20 and 100 nm in diameter [71]. The particle sizes vary depending on the precursors employed and the synthesis technique condition [74]. nZVI can be identified via XRD analysis regarding the pronounced peak of the (110) crystal plane typically found at $2\theta = 45^\circ$, as shown in Figure 1.3(c) [75]. In addition, the XRD pattern of nZVI also displays soft peaks at $2\theta = 65^\circ$ and 82°, corresponding to the (200) and (211) Fe^0 crystal planes, respectively. These nZVI peaks may shift slightly after being modified or utilized for specific applications.

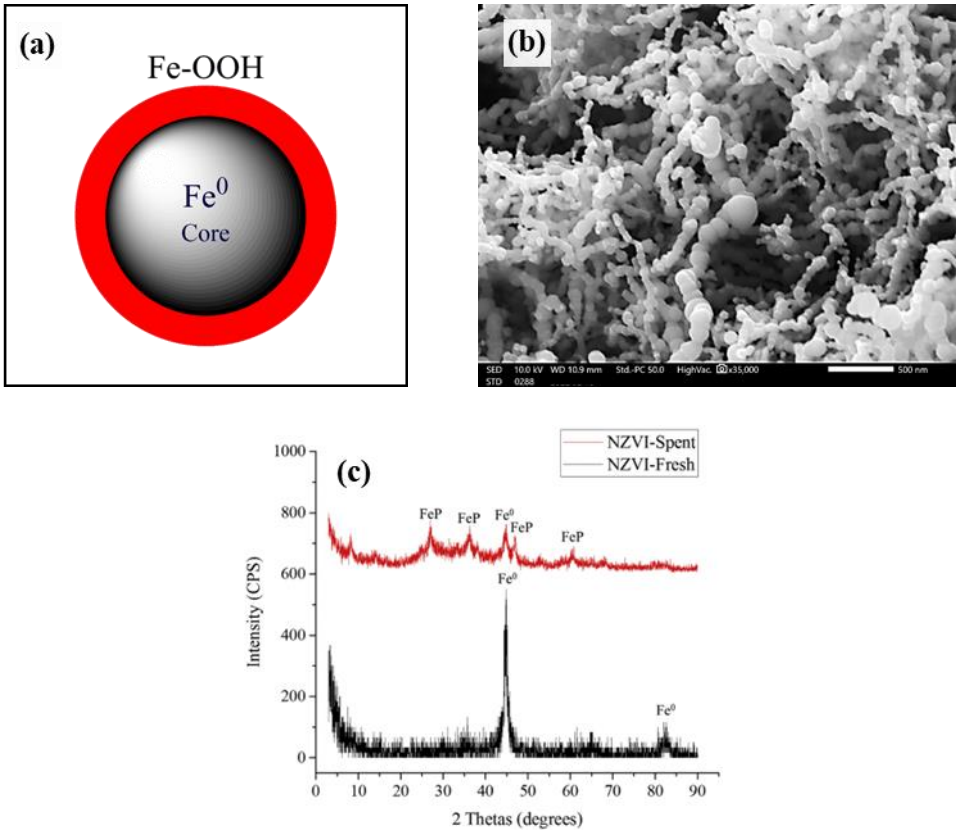

Figure 1.3. nZVI characteristic: (a) nZVI basic structure; (b) SEM image of nZVI; (c) XRD pattern of nZVI [75].

1.5.3. Suitability factors of nZVI quality for water treatment applications

Many distinctive qualities of nZVI make it appropriate for applications involving contaminant removal. The nZVI structure, consisting of zero-valent iron (Fe^0) core and coated with iron oxide as the outer shell, is capable of a reduction process at the core, while the outer shell operates as a reaction site for electrostatic interaction and chemisorption adsorption mechanism [76]. Mineralization, adsorption, reduction, and precipitation are some of the standard removal processes used by nZVI that have been crucial in removing contaminants [77]. nZVI can promptly form an electrostatic reaction with contaminants because of its susceptibility in the ionization process at varying pH solutions. The iron oxide shell attracts negatively charged (anions) and positively charged (cations) impurities since it is positively charged in low pH solutions while negatively charged in high pH solutions [78], [79].

Recent studies have revealed that nZVI exhibits ligand-like characteristics when dissolved in water. nZVI can activate activating ambient molecular oxygen (O_2) using "two-electron" and "single-electron" oxidation reactions to generate reactive oxygen species (ROSs), where these products are capable of effectively degrading or mineralizing contaminants. Chemical Eqs. (1.1)–(1.4) show the oxidation process to produce ROSs, which are hydrogen peroxide (H_2O_2), superoxide anion ($\bullet O_2^-$), and hydroxyl radical (•OH) [62].

$$Fe^0 + O_2 + 2H^+ \xrightarrow{2\bar{e}} Fe^{2+} + H_2O_2 \quad (1.1)$$

$$Fe^{2+} + O_2 \xrightarrow{\bar{e}} Fe^{3+} + \cdot O_2 \quad (1.2)$$

$$Fe^{2+} + \cdot O_2 + 2H^+ \xrightarrow{\bar{e}} Fe^{3+} + H_2O_2 \quad (1.3)$$

$$Fe^{2+} + H_2O_2 + H^+ \xrightarrow{\bar{e}} Fe^{3+} + H_2O + \cdot OH \quad (1.4)$$

1.5.4. nZVI limitation

Natural nZVI has the benefit of being tiny and having superior reducibility, which makes it an excellent adsorbent choice for removing contaminants from water [80]. However, the use of nZVI in environmental remediation applications encounters some challenges.

In practical applications, nZVI removes contaminants through an electron transfer or contact reaction where the water solution is the medium [81], [82]. Nevertheless, nZVI particles are not effectively preserved in air and water because they readily corrode and oxidize when exposed to oxygen, forming passive film layers such as iron (III) hydroxide, maghemite, goethite, lepidocrocite, and hematite [83], [84]. This passivation drives Fe^0 to vanish rapidly, reducing the nZVI's redox reactivity. The complete oxidation of nZVI leads to a decline in its reactivity, thereby diminishing its efficacy in the remediation of water contamination from targeted contaminants.

Strong Van der Waals forces and magnetic attraction provide the nZVI particles with a high reaction capacity [85], [86]. When nZVI is used in water, Brownian motion leads to random collisions between nZVI particles, resulting in aggregation. This phenomenon reduces the number of specific surface sites for the adsorption of contaminants. These agglomerated particles make their density higher than water's, thereby decreasing the mobility of nZVI.

Based on some of the nZVI limitations, modifications need to be considered and implemented to surmount these drawbacks, and nZVI can serve as an excellent material for water treatment.

1.5.5. nZVI reinforcement

The drawbacks shown by nZVI, such as particulate agglomeration, can be significantly diminished by reinforcing nZVI with additional components, such as carbon-based materials [87]–[89], clay minerals [73], [85], polymers [90], carbon-organic frameworks (COF) [91], and metal-organic frameworks (MOF) [92], [93]. The benefits of supporting materials can compensate for the shortcomings of nZVI. For instance, nZVI can be stabilized, and oxidation and aggregation can be diminished by depositing the nZVI into the porous structure of the supporting material. In addition, reinforcing materials with specific functional groups also have their impurity removal capability, which can enhance the nZVI composite's performance in removing contaminants. Thus, reinforced nZVI often offers more advantages, such as improved contaminant removal performance and stronger reactivity and stability, than unreinforced or bare nZVI.

Clay minerals, including zeolite, bentonite, montmorillonite, and kaolinite, are frequently employed as reinforcing agents for nZVI and improve water contaminant removal. This material is used to get over nZVI's drawback of quickly aggregating. Depositing nZVI particles in the pores of this mineral reduces the contact between nZVI and oxygen, slowing down the rapid oxidation of Fe^0 and enhancing the nZVI performance in eliminating contaminants. In addition to this factor, the SSA and porosity of the composite increased, revealing a more significant reactive site than the original mineral without nZVI [88], [94]. Moreover, incorporating nZVI with this support material is able to

deliver better removal efficacy compared to nZVI alone since the mineral itself has a good adsorption capacity against contaminants such as heavy metals [73], [87].

Carbonaceous materials also have the potential to serve as a support material for nZVI because of their well-known qualities of having a large surface area and being inexpensive, besides excellent dispersion in water [81], [95], [96]. This carbonaceous material includes carbon nanotubes (CNT), biochar, activated carbon (AC), and graphene oxide (GO). Carbonaceous materials with various precursors are the focus of ongoing research into how well nZVI composites can remove contaminants. Studies have been done on the efficiency and practicality of using biochar and activated carbon from biomass sources like rice husk [75], [97] and corn agro-waste [81], [98] as an nZVI support material. Dong et al. [98] used an oxidant, alkali, and acid to treat the surface of biochar synthesized from cornstalk, resulting in an nZVI-biochar composite that effectively improves the removal of chromium (Cr) from water. Using this carbonaceous material and nZVI has positively impacted the composite's characteristics, with a large specific surface area, a more significant negative, and increased functional groups appropriate for water treatment applications. Agglomeration of nZVI can also be minimized by employing carbon materials such as mesoporous carbon and graphene-based materials because nZVI particles can penetrate pores and fold on the material's surface.

Diverse support materials confer distinct features and capabilities for contaminant removal on the modified nZVI. Reinforced nZVI exhibits better dispersion properties, antioxidant capacity, and higher environmental contaminant removal than bare nZVI. Further extensive investigations are required to determine if the components utilized to support nZVI are suitable for removing more particular contaminants.

1.6. Graphene oxide (GO)

1.6.1. A brief overview of graphene oxide

Graphene oxide (GO) appeared as one of the most promising and versatile materials this decade because it has outstanding mechanical, chemical, electrical, and thermal properties, leading to its extensive application in various sectors, such as energy and electronics optics and water treatment. GO is a compound of carbon, oxygen, and

hydrogen atoms [99]. It is a carbonaceous material with densely packed, sp^2-bonded carbon atoms in a hexagonal crystal lattice two-dimensionally structure [100], [101]. GO is a nanomaterial generated through the oxidation of graphite, having a planar single-atom layer thick sheet with a thickness of around 1.1 ± 0.2 nm [102]. Utilizing a potent oxidizing agent in GO production generates lattices of oxygen-containing functional groups (OCFG) on the GO surface and edge, such as hydroxyl carboxyl and epoxy groups [102], [103]. These groups make the surface of GO hydrophilic, enabling it to disperse in water and other solvents [104], [105]. In addition, hydrogen bonding, coordination, and electrostatic interactions enable GO to engage favorably with metal ions and organic impurities in the presence of these functional groups. Moreover, the advantages of GO, which have a large surface area, numerous active sites, and a superior delocalized electron system, make it very beneficial to apply in water treatment.

1.6.2. Structural and morphology of GO

Graphene oxide has a layered structure that can be described as a stack of graphene sheets that OCFGs bond together [72]. The number of OCFGs can vary depending on the synthesis method, but typically it is between 10–30 % of the total carbon atoms. Different functional groups may be located in the basal plane than those on the sheet edge. Functional groups like carboxy, phenol, and carbonyl are often located on the sheet edge, whereas functional groups like hydroxyl and epoxy are typically on the GO basal plane [102]. The variety of OCFG influences the characteristics of the GO towards an application. The GO structure's heterogeneity and stoichiometry vary depending on the synthesis and the reaction nature [106].

Graphene's structure significantly influences the GO's physical and chemical characteristics. The mineral analyses revealed that when oxidation levels increased, the graphitic quality of the formed GO reduced. Graphite's early oxidation stage produced hydroxyl and carboxyl functional groups in the lattice, which were ultimately converted to epoxide functional groups toward the end of the oxidation [102]. Moreover, these functional groups make the material very hydrophilic, allowing easy dispersion in water or other solvents [107]. Figure 1.4(a) shows the chemical structure of GO.

The morphology of GO is essential for understanding its properties and behavior in various applications. The morphology of GO is complex and irregular due to the grafting of OCFGs on the surface. The presence of these functional groups introduces structural defects and distortions in the graphene lattice, leading to a crumpled, irregular, and wrinkled morphology, as shown in Figure 1.4(b) [108]. The features of these morphologies lead to the GO's large surface area. Nanoscale wrinkles and folds may serve as nanosize passageways for transporting tiny organic compounds like water molecules [109].

X-Ray Diffraction (XRD) can evaluate GO nanosheet formation and probable phase. The presence of prominent diffraction peaks located within the 2θ range of 8° to 12°, corresponding to the (002) crystal plane, provided evidence of the successful oxidation of graphite to GO. For instance, the diffraction peaks of GO nanoparticles were discovered by Liu et al. [109] and Shan et al. [110] to be at $2\theta = 10.84°$ and $2\theta = 10.6°$, respectively, within the typical characteristic peak of GO powder. Due to the presence of OCFGs, the predicted interlayer spacing of GO powder (0.34 nm) is less than the observed value (0.84 nm) [99]. An example of the GO XRD pattern is depicted in Figure 1.4(c).

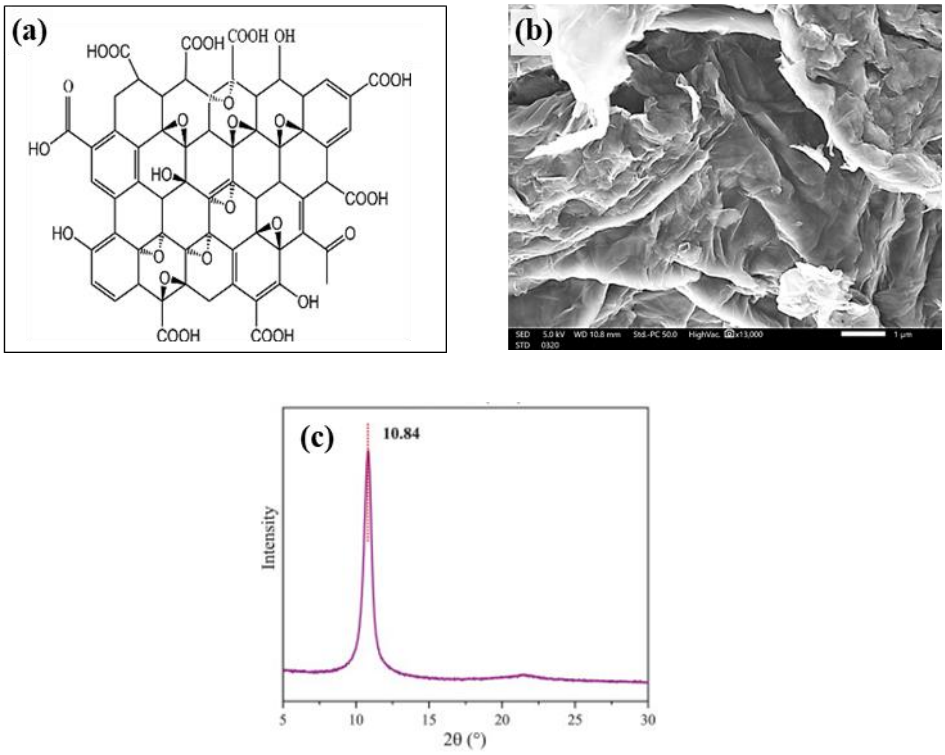

Figure 1.4. Characterization of GO: (a) Chemical Structure [108]; (b) morphology of GO under SEM; (c) XRD pattern [109]**.**

1.6.3. GO properties

GO possesses various unique qualities, including expansive surface area, exceptional mechanical strength, remarkable thermal stability and conductivity, and good electrical conductivity. The remarkable GO properties provide a broad number of potential applications, including those in electronics, energy storage, catalysis, and biomedical. Moreover, the OCFGs on the GO surface make it attainable to alter the material's features, such as its hydrophilicity, to suit specific applications. The specific GO properties could be concluded as follows:

I. **Mechanical properties**: Due to imperfections and the presence of some functional groups, graphene oxide is often more brittle and less mechanically resistant than graphene. The diffusion of functional groups and the degree of oxidation affect the mechanical characteristics of GO. On average, GO has a fracture strength of 80 MPa and a modulus of 32 GPa, demonstrating its impressive strength and impermeability [102].

II. **Physical:** Plenty of free π electrons are presented on GO, and the material's planar shape encourages cycloaddition and carbine insertion. Compared to graphene, GO is less hydrophobic. The establishment of hydrogen bonding and complexation with various metal ions and certain organic compounds was facilitated by anionic carboxylate groups on their lattice edges.

III. **Thermal:** GO is thermally stable and retains its structural integrity and functional properties up to a specific temperature (200–300°C), beyond which it starts to decompose and lose OCFG. GO exhibits diffusive conductivity at high temperatures, but at low temperatures, it exhibits ballistic conductivity [102]. It has relatively low electronic heat conductivity as well.

IV. **Optical**: OCFGs on the GO surface led to high absorption in the UV-visible spectrum. The degree of oxidation and the type of present functional groups affect the absorption intensity.

V. **Electrical**: GO naturally exhibits inherent semiconducting properties. The electrical conductivity of GO is poorer than that of graphene due to the presence of insulating OCFGs.

VI. **Chemical**: The stacking of GO's structure into a π–π form enables interaction with other molecules. Because of OCFGs, GO can encounter various chemical reactions, including functionalization with other molecules and reduction of GO to graphene.

VII. **Biological**: GO has the propensity to get impregnated with medicinal substances that contain aromatic rings and interact with deoxyribonucleic acid (DNA) and ribonucleic acid (RNA).

VIII. **Water solubility:** OCFGs render GO hydrophilic, allowing for easy water dispersion [105].

1.6.4. Synthesis and its Impact on GO Performance

Although graphene and GO's uniqueness has recently piqued much attention from material engineers and scientists, the GO synthesis method has an extensive evolutionary narrative that goes back many decades. In brief, Brodie created bulk graphite oxide for the first time in 1855 at Oxford University by combining graphite with fuming nitric acid (HNO_3) and potassium chlorate ($KClO_3$) as precursors together in a distiller while a water bath system kept at the temperature of 60 °C [111]. Then in 1898, Staudenmaier increased the acidity of the mixture to improve Brodie's method by using concentrated H_2SO_4 [111]–[113]. However, this method took a prolonged time and was risky since it produced very harmful volatile chlorine dioxide (ClO_2) gas [114]. Subsequently, in 1958, Hummers and Offeman proposed a different technique by employing H_2SO_4 and $KMnO_4$ to reduce the GO generation's deleterious level [11], [114]. The Hummers technique is the most often used method among researchers to produce GO.

In summary, the Hummer process involves combining a specific quantity of concentrated sulphuric acid (H_2SO_4), sodium nitrate ($NaNO_3$), and graphite in an ice-bath apparatus with a constant ambient temperature controlled at 0–4 °C. Under vigorous agitating, potassium permanganate ($KMnO_4$) is gently inserted into the mixture. Then, the mixture's temperature is maintained between 35 and 38 °C for an appropriate duration, and an amount of deionized or distilled water is added to the mixture subsequently. The mixture's temperature is subsequently raised to 98 °C and maintained for some specific period. The mixture's residual manganese dioxide and permanganate are transformed into soluble manganese sulfate by adding an amount of 30% hydrogen peroxide (H_2O_2) solution. Finally, distilled water was used to wash the resulting GO many times.

Each parameter and precursor used in GO production affects the reaction and delivers different performance effects of GO toward its application. Consequently, numerous researchers have looked at altering the Hummer technique to generate GO. As an example, phosphoric acid (H_3PO_4) was employed in the GO synthesis process in the research of Cao et al. [115] and Lebron et al. [116]. Han et al. [117] streamlined the GO synthesis process and reduced the time required by removing many stages and using $NaNO_3$ as an additional oxidizing agent. Sun et al. [118] have incorporated ascorbic acid for reduction purposes. Yuan et al. [119] used ultrasonic to determine the oxidation reaction rate and

found that the oxidation and exfoliation processes are crucial for creating more functional GO in their investigation. The impact of various oxidative circumstances on the oxygen content and distribution of OCFGs on GO was examined by Muzyka et al. [120]. They found that, even while employing the same oxidation procedure, the chemical structure of GO may be altered by altering the reaction circumstances. F et al. [121] emphasized that the sonication step in GO synthesis is necessary for creating superior GO nanocomposite films used in applications of UV light-blocking. The sonication method was improved by Arabpour et al. [122] to promote oxidation and produce high-quality GO in removing ECs (Methylene Blue). The addition of the H_2O_2 process to the Hummers technique can significantly alter the characteristics of GO, as demonstrated by Yoo & Park [123].

Numerous studies have been carried out to enhance the GO synthesis by modifying temporal parameters, phases, and precursors; nonetheless, the approach shown remains identical to Hummer's original method. Although researchers have introduced various ways to improve GO synthesis, research on low-cost GO manufacturing procedures, producing high-quality GO that satisfies current standards, and environmental friendliness is yet underway.

1.6.5. Challenges and future research perspectives

GO has been extensively studied for its potential applications in water treatment due to its remarkable physicochemical features, such as changeable surface chemistry, large surface area, and outstanding adsorption capacity. However, some challenges regarding using GO also need to be addressed.

Hummer method is the chemical exfoliation approach, extensively used and the most preferred approach by most researchers for synthesizing GO-based nanomaterials [124], [125]. Unfortunately, utilizing this method to produce GO-based nanomaterials consumes a lengthy time. Therefore, future research considerations should investigate the significance of the sub-processes of this method and evaluate whether the usage of chemicals should be raised or lessened to reduce manufacturing costs and expedite the production of GO–based adsorbents. It is also entirely reliable and essential to scrutinize

the impact of subprocess duration on GO performance in an application to develop a time- and cost-effective process, which is very beneficial to the manufacturing industry.

Regenerating GO after adsorbing contaminants can be challenging, as it may require harsh chemicals or high-temperature conditions. These conditions drive to defect of the GO, which diminishes its adsorption efficiency. In addition, collecting spent GO adsorbent employed for regeneration in water treatment applications is a significant additional challenge. Gathering the spent GO for regeneration might not be accessible after it has been dispersed in water due to the hydrophilic nature of GO. Therefore, this issue needs to be resolved for GO to be appropriately collected after it has been utilized for regeneration or subsequent treatment actions.

1.7. The research aims and objectives.

This study aims to produce a reasonable GO for antibiotic removal from water with a facile synthesis, saving time and material costs. Also, this study aims to develop a nanocomposite based on nZVI and GO that excels in removing antibiotics from water.

There are two primary research projects in this study. The first research project sought to develop practical GO for treating water contaminated with ciprofloxacin by optimizing the chemical synthesis of GO based on time- and material-cost-saving protocols. The first project's objectives are as follows:

I. To explore the influence of synthesis parameters on GO performance for CIP removal.

II. To develop facile GO chemical synthesis by empirically optimizing the synthesis parameters based on time- and material-cost-saving protocols.

III. To generate a novel GO with a low material cost and compatibility with efficient CIP removal applications.

IV. To characterize the surface morphology and physiochemical features of optimized GO.

V. To compare the performance of GO produced through the optimized synthesis with various GO samples synthesized using conventional and functionalization methods.

VI. To investigate the effects of CIP removal conditions, including the GO dosage, contaminant pH, CIP's initial concentration, and working temperature, on CIP removal by batch experiments.

VII. To elucidate the mechanism of CIP removal by employing a kinetics study, a desorption experiment using various eluents, Fourier transform infrared (FTIR) spectroscopy, and statistical methods.

While the second research project focuses on developing the GO-precipitated nZVI nanocomposite (nZVI/GO) and assessing the impact of GO precursor components on the nanocomposite's efficiency in removing CAP from water. Several objectives have been specified for the second research project, as follows:

I. To explore the influence of the GO precursor component on the surface morphology of the GO precipitated nZVI nanocomposite (nZVI/GO).

II. To investigate the significance of the GO precursor by exploring its influence as a mechanical supporter of nZVI to eliminate CAP.

III. To develop a GO-precipitated nZVI nanocomposite (nZVI/GO) with excellent CAP removal performance using the most effective GO precursor.

IV. To characterize the surface morphology and physiochemical features of the nZVI/GO nanocomposite at various mass ratios.

V. To optimize the CAP removal conditions, including mass ratio, dosage, initial pH, initial concentration, and working temperature, by nZVI/GO nanocomposite.

VI. To elucidate the CAP removal mechanism of the nZVI/GO nanocomposite by employing a kinetics analysis, a desorption experiment using various eluents, Fourier transforms infrared (FTIR) spectroscopy, thermodynamics, and statistical methods.

VII. To evaluate the performance of the nZVI/GO nanocomposite in CAP removal from natural water and its recyclability.

1.8. Thesis Outline

The doctoral thesis structure comprises five main chapters outlined as follows:

Chapter 1 begins with background information on emerging contaminants, pharmaceuticals, and global water pollution issues due to these substances. Then this chapter also presents more specific details related to antibiotics, including the contamination pathway of ciprofloxacin and chloramphenicol in environmental water. In addition, this chapter explains the information regarding graphene oxide, the impact of synthesis on GO performance, challenges, and research perspectives related to GO. Furthermore, the background of nZVI and its suitability and limitations for water treatment application are also discussed in this chapter. Then, chapter 1 is closed with a summary of the aims and objectives of this Ph.D. work.

Chapter 2 provides a list of the materials and chemicals used in the experiment. In addition, this chapter thoroughly describes the methodologies for synthesizing GO and nZVI-based materials. Also described are characterization methods and equipment for depicting the physicochemical characteristics of the materials. The batch experiment operation under various antibiotic pollutants removal conditions and desorption batch experiment is also covered in detail in this chapter. Moreover, the kinetic principles and thermodynamic models for CIP and CAP removal by these GO and nZVI-based nanomaterials are also presented.

Chapter 3 presents in detail the findings of synthesis optimization in producing a practical GO for CIP removal. This chapter systematically reports findings regarding the effect of conditions at each synthesis stage on GO performance in CIP removal. In addition, the comparative findings of the CIP removal performance of GO with optimized synthesis and GO manufactured conventionally are also included in this chapter. Then this chapter also reports the results of the GO's reactivity assessment for ideal CIP removal conditions. In addition, the results of desorption experiments performed on optimized GO are also contained in this chapter. Moreover, several series of analyses,

including kinetic, thermodynamic, and cost analyses, are also discussed in detail in this chapter. Finally, the physicochemical properties of GO are discussed in this chapter, such as morphology, functional element group availability, surface elemental composition, and crystallinity.

Chapter 4 discusses the use of nZVI/GO nanocomposite for CAP removal from water by nZVI/GO nanocomposite. The physicochemical characteristics of GO, nZVI, and nZVI/GO nanocomposite are discussed thoroughly at the beginning of this chapter. Subsequently, the efficiencies of nZVI/GO nanocomposites in removing CAP using various precursors, mass ratios, and dosages are presented. This chapter also addresses the performance of the nZVI/GO nanocomposite against CAP removal under various removal conditions. In addition, this chapter also elaborates on the findings regarding desorption analysis, the condition of the material in the post-CAP removal phase, and the CAP removal mechanism. This chapter ends with a discussion of results related to the stability and recyclability of nanocomposite materials and their practical implications.

At last, **Chapter 5** summarizes the essential findings of all research projects and their potential impact on the field. In addition, this chapter provides an overview of suggestions for future studies to build upon the current findings.

This page is intentionally left blank.

Chapter 2

Research Methodology

2.1. Chemical and materials

Table 2.1 provides every detail of the purchased chemicals and materials used in this research. All the chemicals and materials used were of an analytically acceptable purity for scientific research, and none of those were further refined or modified in any other way. Deionized water (DIW) from the Milli-Q system (18.2 MΩ cm Direct-Q water purification system, Merck KGaA, Germany) was utilized in the solution preparations.

Table 2.1. The list of chemical and material information used in this research.

Chemical/Material Name	**Molecular Formula**	**Specifications**	**Company**
Graphite powder	C	MW=12.01 g/mol, particles size <45 µm, purity >= 99.5%	FUJIFILM Wako Pure Chemical Solution Corporation, Japan
Potassium permanganate	$KMnO_4$	MW= 158.034 g/mol, purity >= 99.3 wt%	FUJIFILM Wako Pure Chemical Solution Corporation, Japan
Sulphuric acid	H_2SO_4	MW= 98.079 g/mol, purity >= 95.0 wt%	FUJIFILM Wako Pure Chemical Solution Corporation, Japan
Hydrochloric acid	HCl	MW= 36.458 g/mol, purity = 35~37 wt%	FUJIFILM Wako Pure Chemical Solution Corporation, Japan
Phosphoric acid	H_3PO_4	MW= 97.994 g/mol, purity >= 88.0 wt%	FUJIFILM Wako Pure Chemical Solution Corporation, Japan
Hydrogen peroxide	H_2O_2	MW= 34.0147 g/mol, purity = 30~35.5 wt%	FUJIFILM Wako Pure Chemical Solution Corporation, Japan

Sodium chloride	NaCl	MW= 58.44 g/mol, purity >= 88.0 wt%	FUJIFILM Wako Pure Chemical Solution Corporation, Japan
Ethanol	C_2H_5OH	MW= 46.07 g/mol, purity >= 99.5 wt%	FUJIFILM Wako Pure Chemical Solution Corporation, Japan
Nitric acid	HNO_3	MW = 63.01, purity = 69 ~ 70%	FUJIFILM Wako Pure Chemicals, Japan
Sodium hydroxide	NaOH	MW= 39.997 g/mol, purity >= 97.0 wt%	Junsei Chemical Co. Ltd, Japan
Ciprofloxacin hydrochloride monohydrate	$C_{17}H_{18}FN_3O_3•HCl•H_2O$	MW= 367.81 g/mol, purity >= 98 wt%	Sigma-Aldrich Co, USA
Ferric chloride hexahydrate	$FeCl_3•6H_2O$	MW= 270.30 g/mol, purity >= 99 wt%	Junsei Chemical Co. Ltd, Japan
Sodium nitrate	$NaNO_3$	MW= 84.9947 g/mol, purity >= 99 wt%	Junsei Chemical Co. Ltd, Japan
Sodium borohydride	NaBH4	MW= 37.83 g/mol, purity >= 98 wt%	Sigma-Aldrich Co, USA
Chloramphenicol	$C_{11}H_{12}Cl_2N_2O_5$	MW= 323.132 g/mol, purity >= 98 wt%	Sigma-Aldrich Co, USA

2.2. Material synthesis methodology

2.2.1. Synthesis of GO for synthesis optimization

The chemical synthesis of the Hummer method was fundamentally used to produce GO in this study. In brief, 1 g of graphite powder was intercalated with 20 mL of concentrated H_2SO_4, and the mixture was vigorously agitated for 10 minutes in an ice bath (=< 4 °C). This step was crucial for ensuring the graphite particles were uniformly mixed with the H_2SO_4 solution. After that, 3 g of $KMnO_4$ was added to the mixture and stirred for 20 min.

It should be noted that $KMnO_4$ was added gradually while the mixture was agitated to keep the temperature stable and prevent it from rising suddenly. The mixture was then heated to 38 °C and stirred for 30 min. Next, 50 mL of DIW was added to dilute the mixture, followed by heating it to 95 °C under the stirring condition for 10 min at the temperature. 3 mL of 30% H_2O_2 was added to terminate the reaction and reduce the leftover manganese dioxide (MnO_2) and permanganate (MnO_4^-) to soluble manganese sulfate ($MnSO_4$). Soluble ions were removed from the mixture by centrifuging. The precipitate was cleaned using a 30% HCl solution and DIW repeatedly until the pH of the supernatant neared neutral. The precipitated product (GO) was dried in an oven at 50 °C for 24 h after cleaning. Figure 2.1 depicts the schematic diagram of the GO synthesis process.

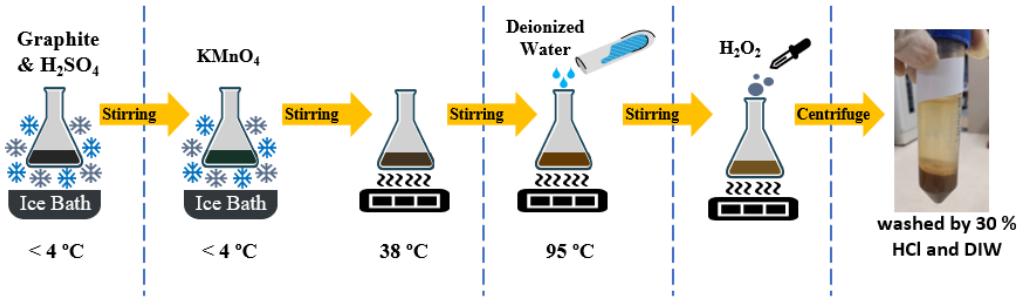

Figure 2.1. Schematic diagram of the GO synthesis process.

2.2.2. Syntheses of conventional and functionalized GO for performance comparison.

An additional 2 GO samples were produced to compare their performance in removing CIP with GO synthesized by the improved approach gained after GO synthesis optimization had been done in this work. The GO sample resulting from the optimized synthesis is identified as "O–GO." The selection of the synthesis to produce two additional GO samples was based on their exceptional performance in removing contaminants from contaminated water in previous studies.

One of the GO synthesis methods presented is a standard synthesis method used by most researchers to produce GO, referred from [126]. The GO sample synthesized through this conventional approach is named "S–GO." The second synthesis technique was an innovative approach introduced by previous researchers [115], in which phosphoric acid

(H_3PO_4) was used as a supplementary oxidation catalyst to functionalize the material's surface with more active functional groups during oxidation. The GO made by this process is marked as "F–GO."

The S–GO and F–GO synthesis techniques use the same principle as the procedure described in the preceding subsection (chapter 2.2.1). Nevertheless, these syntheses use different sub-processes, material amounts, and aging duration combinations for each stage. Meanwhile, the synthesis process of O–GO has been improved by eliminating specific sub-process and not using supplemental oxidation catalysts. Figure 2.2 depicts the schematic illustration of the elemental synthesis of S–GO and F–GO, while Table 2.2 tabulates the detailed conditions related to the variables, materials employed, and duration in each stage of each GO synthesis technique.

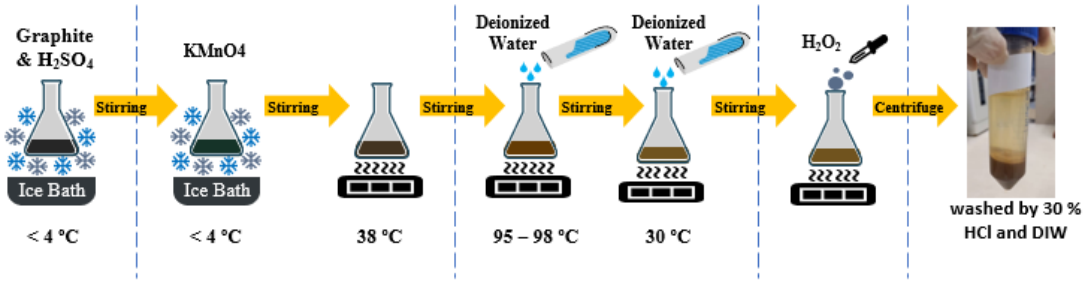

Figure 2.2. Schematic illustration of the elemental synthesis of S–GO and F–GO.

Table 2.2. Detailed synthesis conditions of S–GO, F–GO, and O–GO.

Synthesis Stage	**Process**	**Material / Condition**	**Range**		
			S–GO	F–GO	O–GO
Stage 1:	Oxidizing I	Graphite (g)	1	1	1
H_2SO_4 intercalated graphite		H_2SO_4 (mL)	100	15	20
		Oxidation Catalyst	-	4 mL H_3PO_4	-
		Ice Bath (=<4 °C)	√	√	√
		Stirring Period (min)	5	10	10
Stage 2:	Oxidizing II	$KMnO_4$ (g)	4	2	3
Graphite oxide transformation		Ice Bath (=<4 °C)	√	√	√
		Stirring Period (min)	120	20	10
	Mixing	Reaction Temperature (°C)	38	38	38
		Stirring Period (min)	60	30	20
Stage 3:	Hydrolysis I	DIW (mL)	100	15	50
Graphene Oxide transformation		Reaction Temperature (°C)	95	95	95
		Stirring Period (min)	60	30	5
	Hydrolysis II	DIW (mL)	300	50	-
		Reaction Temperature (°C)	30	30	-
		Stirring Period (min)	30	30	-
Stage 4:	Reducing	30% H_2O_2 (mL)	20	10	3
Reduction					

2.2.3. Synthesis of nZVI

The liquid-phase reduction process with nitrogen purging was used to create nZVI. The reaction environment was controlled at 30 °C using a water bath setup. In brief, 100 mL of DIW was mixed with 2.5 g of $FeCl_3$•$6H_2O$, and the mixture was agitated anaerobically for about 30 min at 400 rpm to produce the nZVI. The reducing solvent was pre-made by dissolving 1.1 g of $NaBH_4$ in 50 mL of DIW to convert ferric iron (Fe^{3+}) to nZVI (Fe^0). To ensure the reduction was fully accomplished, the solution was added to the ferric iron solution at a rate of 20 mL/min and agitated for an additional 5 min. Chemical Eq. (2.1) illustrates how the reaction happened during the reduction of Fe^{3+} [28], [127]. The nucleated product in black powder was then removed using vacuum filtering with a 0.45 μm filter. Before being vacuum dried and utilized, the powdery residue was cleaned with ethanol and DIW. It is essential to note that deionized water was used in this synthesis after being pre-deoxygenated with N_2 for 10 min [28].

$$2FeCl_3 \cdot 6H_2O + 6NaBH_4 + 18H_2O \rightarrow 2Fe^0 \downarrow + 21H_2 \uparrow + 6B(OH)_3 + 6NaCl \qquad (2.1)$$

2.2.4. Synthesis of nZVI/GO nanocomposites

The nZVI/GO nanocomposites were produced utilizing the same nZVI synthesis methodology explained in Chapter 2.2.3. Once the specific amount of GO was exfoliated by sonication in 100 mL of DIW for 2 hours, 2.5 g of $FeCl_3$•$6H_2O$ was added to the mixture. The crumpled GO needed to be thoroughly exfoliated and distributed evenly in the DIW. However, due to the high specific GO volume, an additional 2 h of sonication time was needed to exfoliate 1 g of GO in the same volume of DIW when creating the nZVI/GO nanocomposite with a mass ratio of 1:2 (nZVI:GO). After that, the nZVI/GO nanocomposite samples are represented as nZVI/GO-x, where x denotes the mass ratio of nZVI to GO (nZVI: GO). The nanocomposites were created using 0.05 g, 0.25 g, 0.5 g, and 1 g of GO, with the mass ratios (nZVI: GO) being 10:1, 2:1, 1:1, and 1:2, respectively.

2.3. Characterization

2.3.1. X-Ray Diffraction (XRD)

The crystalline structure of the researched nanomaterials was analyzed by a Rigaku X-ray diffractometer (XRD, TTR, Rigaku, Tokyo, Japan) in the 2θ range of 2–90° with a scan rate of 3° min^{-1} using Cu Kα radiation (λ=1.5418 Å) from X-ray source operated at 300 mA and 50 kV. The sample used for the analysis was powder, and a specific powder specimen holder was used for XRD analysis. Sample preparation was carried out strictly with a method that assures no contaminant affects the analyzed sample. The layers thickness (t_{layer}, nm) of GO samples and the average crystalline size, D_c (nm) of the nZVI-based nanocomposite were determined using the Debye-Scherrer Eq. (2.2) as follows [28], [116], [128]:

$$t_{layer} @ D_c = \frac{0.89\lambda}{\beta \cos \theta_\beta} \quad (2.2)$$

Where λ is the x-ray wavelength (λ=1.5418 Å), β represents the full peak width at half maximum (FWHM, radians), and θ_β denotes the Bragg's angle.

2.3.2. Scanning electron microscopy (SEM) and Energy Dispersive X-ray Spectrum (EDS)

The surface-morphology and elemental composition of the synthesized GO and nZVI-based nanomaterials were characterized via a JSM-IT700HR *InTouchScope* scanning electron microscopy (SEM) incorporated with energy-dispersive x-ray spectroscopy (EDS) devise (JEOL Co., Japan). The surface of the nanomaterial was scanned with an electron beam with an operating voltage range of 5–15 kV to generate high-resolution morphological photographs. Simultaneously, the EDS spectrum with defined elemental peaks was employed to determine their surface's component composition.

2.3.3. Fourier Transform Infrared (FTIR)

The molecular structure and OCFGs on the GO surface were investigated using Fourier transform infrared spectroscopy (FTIR) spectra measured at 700 to 4000 cm^{-1} on a JASCO FT/IR-4200 spectrophotometer before and after the reaction with antibiotic contaminants. The FTIR spectra revealing changes in the intensity and position of specific

peaks indicate the chemical interactions between nanomaterial samples and antibiotics contaminants.

2.4. Experimental design of GO synthesis conditions optimization

2.4.1. GO synthesis variable

This study introduces a novel experimental design and thoroughly analyzes the effects of various precursors and synthesis conditions on the entire synthesis process to develop a practical approach for improving the removal of CIP from water. This analysis makes a unique contribution to the current body of literature. Numerous experiments were conducted, manipulating different variables to optimize the precursors and chemical synthesis conditions empirically. The objective was to produce functional GO nanosheets demonstrating a noteworthy capability for removing contaminants, specifically CIP.

The GO synthesis described in Chapter 2.2.1 was a framework of preliminary procedure to investigate the optimized GO synthesis conditions. In general, the GO synthesis process involves the transformation of graphite into GO. The conditions throughout the synthesis process must be considered to produce high-quality GO suitable for the application. Therefore, the GO synthesis conditions were comprehensively investigated and empirically optimized to elucidate their impact on the GO reactivity and acquire an ideal approach to producing GO based on cost-efficient and time-saving protocols without compromising its performance, particularly in CIP removal. In order to make the synthesis optimization more systematic, this study has categorized the process into 4 primary stages depending on their specific process, as depicted in the synthesis schematic diagram Figure 2.3: graphite to H_2SO_4 intercalated graphite compound transformation, intercalated graphite compound transformation to graphite oxide transformation, transforming graphite oxide to GO, and reduction. A total of 8 synthesis variables from the mentioned stages were evaluated in an orderly manner for synthesis optimization. The synthesis variable ranges are summarized in Table 2.3.

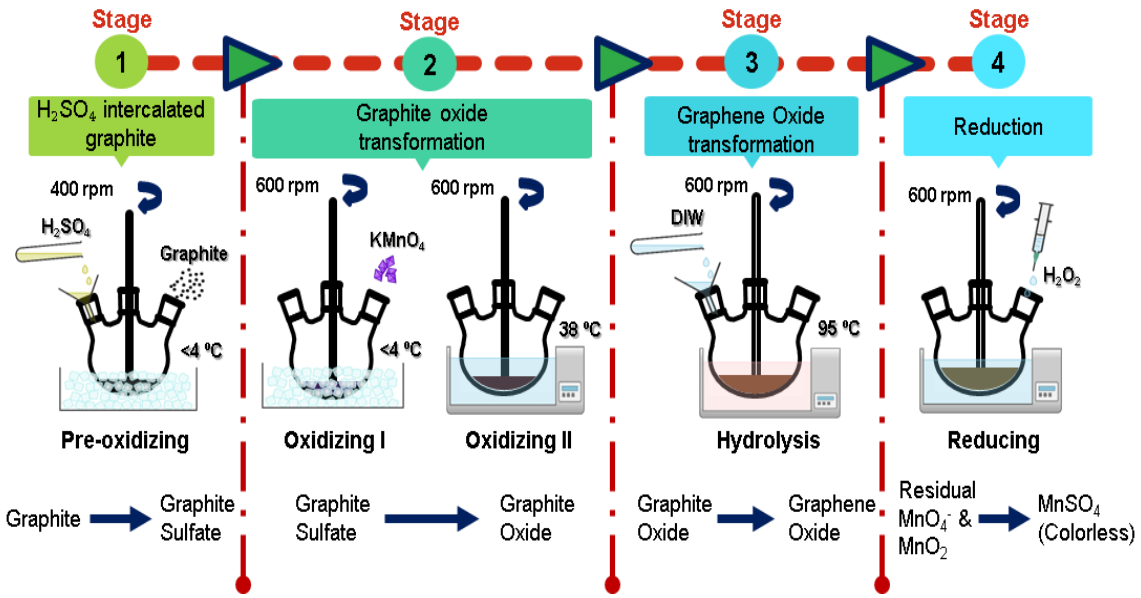

Figure 2.3. Four primary stages of GO synthesis.

Table 2.3. Variable ranges of each synthesis stage.

Stage 1: H_2SO_4 intercalated graphite		**Stage 2: Graphite oxide transformation**			**Stage 3: Graphene Oxide transformation**		**Stage 4: Reduction**
H_2SO_4 (mL)	Mixing Period (min)	$KMnO_4$ (g)	Mixing Period [at temperature <4 ºC] (min)	Aging Period [at 38 ºC] (min)	Deionized Water (mL)	Mixing Period (min)	H_2O_2 (mL)
10, 20, 30, 50	5, 10, 20, 30	1.5, 3, 4.5, 6	5, 10, 20, 30, 60	10, 20,30, 60	25, 50, 100	5, 10, 20, 40	0, 3, 6, 12

2.4.2. CIP removal assessment for synthesis parameter optimization

Batch experiments were conducted to determine the appropriate GO synthesis parameters for ideal CIP removal from water. For this purpose, a standard CIP aqueous solution with 100 mg/L CIP as an initial concentration (C_0) was prepared by diluting a certain quantity of CIP salt in a specific amount of DIW. 50 mg of GO samples were added into the Erlenmeyer flasks containing 200 mL of the CIP solutions with the natural pH (pH_0) of 6.2, giving the GO dosage equivalent to 0.25 g/L. The mixture was swirled for 3 h to attain equilibrium using a magnetic stirrer (RSH-6DN, As One Co., Japan) at 25 °C and 500 rpm before 1 mL of the mixture was retrieved and filtered through a 0.45 μm membrane filter for sampling and analysis. The GO samples with specific synthesis parameters used in this experiment are tabulated in Table 2.4. The ideal GO synthesis parameter was evaluated through the performance of GO samples in CIP removal, represented by the CIP removal capacity at equilibrium (q_e, mg/g) calculated using Eq. (2.3) as follows:

$$q_e = \frac{V\,(C_0 - C_e)}{m} \tag{2.3}$$

where C_0 is CIP's initial concentration (mg/L), C_e can be CIP's equilibrium concentration (mg/L), V denotes the volume (L) of the CIP solution, and m represents the mass (g) of the analyzed GO.

Table 2.4. Specific synthesis parameters used in the empirical optimization.

Exp.	**Stage 1: H_2SO_4 intercalated graphite**		**Stage 2: Graphite oxide transformation**			**Stage 3: Graphene Oxide transformation**		**Stage 4: Reducing**
	H_2SO_4 (mL)	Mixing Period (min)	$KMnO_4$ (g)	Mixing Period [at temperature <4 ºC] (min)	Aging Period [at 38 ºC] (min)	Deionized Water (mL)	Mixing Period (min)	H_2O_2 (mL)
1	10	10	3	20	30	50	10	3
2	20	10	3	20	30	50	10	3
3	30	10	3	20	30	50	10	3
4	50	10	3	20	30	50	10	3
5	20	5	3	20	30	50	10	3
6	20	20	3	20	30	50	10	3
7	20	30	3	20	30	50	10	3
8	20	10	1.5	20	30	50	10	3
9	20	10	4.5	20	30	50	10	3
10	20	10	6	20	30	50	10	3
11	20	10	3	5	30	50	10	3
12	20	10	3	10	30	50	10	3
13	20	10	3	30	30	50	10	3
14	20	10	3	60	30	50	10	3
15	20	10	3	10	10	50	10	3
16	20	10	3	10	20	50	10	3

17	20	10	3	10	60	50	10	3
18	20	10	3	10	20	25	10	3
19	20	10	3	10	20	100	10	3
20	20	10	3	10	20	50	5	3
21	20	10	3	10	20	50	20	3
22	20	10	3	10	20	50	40	3
23	20	10	3	10	20	50	5	0
24	20	10	3	10	20	50	5	6
25	20	10	3	10	20	50	5	12

2.5. Performance Evaluation Test: Assessment for Antibiotics Removal

2.5.1. Assessment of GO reactivity for ideal CIP removal conditions

Batch experiment series was conducted on the optimized GO (O–GO) to evaluate the ideal CIP removal conditions. O–GO with 25 mg/L dosages was initially used by adding 50 mg to 200 mL of the CIP solution. CIP solution with a preliminary determined initial concentration of 100 mg/L and pH_0 of 6.2 (CIP Natural pH) was utilized at 25 °C. Water sampling was done by filtrating 1 mL of the mixture using a 0.45 μm membrane filter at a different contact time interval, t (10, 30, 60, 90, 120, and 180 min). The residue of CIP concentration from the water samples was measured using a UV–vis spectrophotometer (UV-1280, Shimadzu, Japan). The mathematical equations, as presented in Eqs. (2.4) and (2.5(were executed to compute the CIP removal efficiency (%) and CIP removal capacities (q_t, mg/g) at the stipulated time (t), respectively, in assessing optimized GO reactivity toward removing CIP as a targeted contaminant in water.

$$Removal\ Efficiency\ (\%) = \frac{(C_0 - C_t)}{C_0} \times 100\% \tag{2.4}$$

$$q_t = \frac{V\ (C_0 - C_t)}{m} \tag{2.5}$$

where C_0, C_t, V, and m represent the CIP initial concentration (mg/L) and CIP concentration at a specified time, t (mg/L), CIP solution volume (L), and the mass (g) of the analyzed GO, respectively.

The effect of O–GO on the CIP removal reaction condition has been comprehensively explored by manipulating several conditions' variables, as demonstrated in Table 2.5.

Table 2.5. Batch experiments variables for CIP removal assessment.

Reaction condition	Unit	Variable range
Optimized GO dosage	g/L	0.1–1
Initial pH	-	3–11
CIP's initial concentration	mg/L	10–150
Temperature	°C	25–65

2.5.2. Reactivity assessment of the nZVI/GO nanocomposite for ideal CAP removal conditions

A batch experiment was conducted to determine the optimal GO precursor and parameters for eliminating CAP from water. This study utilized 100 mL of CAP solution, with an initial concentration (C_0) of 100 mg/L and an initial pH of 6.2 (CAP nature pH). Subsequently, 25 mg of either nZVI or nZVI/GO was introduced into the solution for experimental purposes. The solution was stirred for three hours at a rate of 500 rpm, utilizing a magnetic stirrer (RSH-6DN, As One Co., Japan) within sealed conical flasks. The temperature was maintained at a constant value of 25°C for the entirety of the experiment. Samples of the solution were extracted at intervals of 10, 20, 30, 60, 90, 120, and 180 minutes. Each sample was filtrated using a 0.45 μm membrane filter for subsequent analysis.

The study comprehensively investigated six conditions, including GO-precursor, nZVI/GO weight ratio, nanomaterial dosage, initial pH, initial CAP concentration, and CAP solution temperature, regarding their impact on the effectiveness of the material in eliminating CAP. More detailed parameters are shown in Table 2.6.

Table 2.6. Batch experiment variables for CAP removal assessment.

Conditions	Unit	Variable range
GO precursor	-	S–GO, F–GO and O–GO
nZVI/GO weight ratio	(nZVI:GO)	10:1, 2:1, 1:1, and 1:2
Initial pH	-	3–11
CAP's initial concentration	mg/L	50–200
Temperature	°C	25–55

The study assessed the performance of nZVI, GO, and nZVI/GO nanocomposites in eliminating CAP by determining their removal efficiency (%) and CAP removal capacities (q_t, mg/g). These values were computed using Eqs. (2.6) and (2.7) as follows:

$$Removal\ Efficiency\ (\%) = \frac{(C_0 - C_t)}{C_0} \times 100\% \quad (2.6)$$

$$q_t = \frac{V\ (C_0 - C_t)}{m} \quad (2.7)$$

where C_0 and C_t are the initial and predetermined time, t, CAP concentrations (mg/L), V is the volume (L) of CAP solution, m represents the mass (g) of the studied material, and q_t denotes the CAP removal capacity (mg/g) at contact time t.

2.5.3. Field-scale application

A field-scale experiment was conducted using natural surface water to evaluate the optimized nanocomposite's practical implications, applicability, and stability for removing CAP. The research methodology involved producing 20 mg/L of CAP-polluted natural surface water using untreated water collected from the Ushikubi River in Fukuoka, Japan, to conduct a specific test. In this study, various dosages (0.05, 0.15, 0.25, and 0.5 g/L) of nanomaterial were administered to the river water contaminated with CAP. The water samples were then analyzed after the reaction.

2.5.4. Iron Leaching Test

This study observed the leaching iron behavior of nZVI and optimized nZVI/O–GO nanocomposite in the CAP solution by quantifying the total iron concentrations (Fe-Total) and dissolved ferrous (Fe^{2+}). The study employed a batch test approach wherein the optimal dosage of nZVI/O–GO nanocomposite samples was added to a 100 mg/L CAP solution. The concentrations of Fe-Total and Fe^{2+} were determined using FerroVer iron (FerroVer reagents) and Ferrous reagents (1,10-phenanthroline) per USEPA guidelines. A direct estimation of ferric ions (Fe^{3+}) concentration can be obtained through the measured concentrations of Fe-Total and Fe^{2+}:

$$[Fe^{3+}]_{\text{concentration}} = [Fe\text{-Total}]_{\text{concentration}} - [Fe^{2+}]_{\text{concentration}} \quad (2.8)$$

2.6. Data Modeling

2.6.1. Kinetics analysis

The proposed reactive nanomaterials' response rate for contaminant removal was analyzed using four kinetic models. The modeling includes pseudo-first-order (PFO), pseudo-second-order (PSO), intraparticle diffusion, and Elovich kinetic models. The following are descriptions of each model's theoretical considerations and conditional assumptions:

2.6.1.1. Pseudo First Order (PFO) Model

Lagergren's first-order equation encapsulates one of the most widely used kinetic models for clarifying the sorption rate in liquid-solid systems.

$$\frac{dq_t}{dt} = k_1(q_e - q_t) \tag{2.9}$$

The PFO model in the following state can be constructed by integrating Eq. (2.9) and applying boundary conditions (t = 0 to t = t and q = 0 to q > 0):

$$\ln(q_e - q_t) = \ln(q_e) - k_1 t \tag{2.10}$$

where q_t represents the contaminants removal capacities (mg/g) at a specific contact time, t (min), q_e indicates the equilibrium removal capacity related to the equilibrium concentration C_e (mg/L), and k_1 is the PFO kinetic constant (min^{-1}) with respect to time, t (min). The active site quantity on the sorbent correspondingly specifies this model's sorption rate.

2.6.1.2. Pseudo Second Order (PSO) Model

The PSO model illustrates the process of determining the adsorption rate and describes the nature of the bonding between sorbent and sorbate. The following equation is the PSO differential equation:

$$\frac{dq_t}{dt} = k_2(q_e - q_t)^2 \quad (2.11)$$

The PSO model in the following state can then be developed by integrating Eq. (2.11) and applying boundary conditions (t = 0 to t = t and q = 0 to q > 0):

$$\frac{t}{q_t} = \frac{1}{k_2 q_e^2} + \frac{t}{q_e} \quad (2.12)$$

Where, k_2 denotes the PSO kinetic constant (g/mg/min). This model can be used to compare and identify the type of sorption based on the acquired experimental data. Chemisorption contributes significantly to the removal mechanism if the model accurately captures the data.

2.6.1.3. Intraparticle diffusion model

The second often-used kinetic model is based on the assumption that sorbent sites have a planar form. Eq. (2.13) defines the intraparticle diffusion model's equation:

$$q_t = k_{intra} t^{0.5} + C \quad (2.13)$$

Where, K_{intra} (mg/g/min$^{1/2}$) represents the intraparticle diffusion rate constant and C (mg/g) is the intraparticle diffusion coefficient related to the thickness of the boundary layer. The model supposes that the sorbate diffusion rate regulates the sorption process inside the sorbent particles' pores.

2.6.1.4. Elovich kinetic model

The Elovich model is often used in systems of gas-solid adsorption. Nonetheless, this research used the model to explain how soluble contaminants may be removed from the water. The Elovich model's fundamental equation is as follows:

$$\frac{dq_t}{dt} = \alpha \exp(-\beta q) \quad (2.14)$$

Eq. (2.15) can be linearized to form the Elovich equation as follows:

$$q_t = \frac{1}{\beta}\ln(1 + \alpha\beta t) \tag{2.15}$$

where α (mg/g/min) designates the initial sorption rate, and β (g/mg) displays a constant proportional to surface coverage and chemical sorption activation energy. This model may be used to explain the kinetic behavior of systems with diverse sorbent surfaces.

2.6.2. Nonlinear Regression and Akaike's Information Criterion Analyses

In order to prevent any errors brought on by the linearization, the models were aligned with the experimental data using the nonlinear regression method. Microsoft Excel was employed to carry out the nonlinear regression.

The Akaike information criterion (AIC) statistical analysis was utilized to determine which model accurately represented the contaminant elimination profile after the experimental data were matched to several models. Eq. (2.16) may be used to calculate AIC, and the model with the lowest value describes the experimental kinetic data numerically as the most acceptable [28], [75].

$$AIC = N\ln\left(\frac{SSE}{N}\right) + 2N_p + \frac{2N_p(N_p + 1)}{N - N_p - 1} \tag{2.16}$$

where N and N_p denote the number of experimental points and model parameters, respectively. *SSE* expresses the sum of square error (SSE) and can be calculated using Eq. (2.17) [28], [75]:

$$SSE = \sum_{t=0}^{t}\left(q_{t,experiment} - q_{t,model}\right)^2 \tag{2.17}$$

Where $q_{t,}$ *experiment* and $q_{t,}$ *model* designate the removal capacities (mg/g) computed from experimental data and regained from the model at a specific contact time t (min), respectively.

2.6.3. Thermodynamics Analysis.

The performance of removing antibiotics was achieved at various temperatures in the thermodynamic analysis. This investigation was conducted to elucidate the removal process and comprehensively understand the interaction between the contaminant and the nanocomposite by applying thermodynamic principles. Therefore, the third thermodynamic principle and conventional Van't Hoff Eqs. (2.18), (2.19) and (2.20) were used to estimate several temperature-dependent thermodynamics parameters, including enthalpy change (H°), Gibbs free energy change (G°), and entropy change (S°) [28], [75], [129].

$$\Delta G° = \Delta H° - T\Delta S° \tag{2.18}$$

$$\Delta G° = -RT \ln K_d \tag{2.19}$$

$$\ln K_d = -\frac{\Delta H°}{RT} + \frac{\Delta S°}{R} \tag{2.20}$$

T symbolizes absolute temperature (K), *R* stands for the universal gas constant (8.314 J K^{-1} mol^{-1}), and K_d designates the distribution coefficient, which is determined using Eq. (2.21) as follows:

$$\ln K_d = \frac{q_e}{C_e} \tag{2.21}$$

where q_e and C_e indicate the equilibrium removal capacity (mg/g) and equilibrium concentration (mg/L), respectively, $\Delta H°$ and $\Delta S°$ were calculated by plotting $ln\ K_d$ against $1/T$ (Van't Hoff plot) and acquiring its slope and interception values, respectively.

2.7. Desorption experiment of antibiotic contaminants

Desorption studies were conducted to explore its regeneration potential in various eluents and to determine the effectiveness of the CIP/CAP adsorption mechanism. Briefly, a certain amount of nanomaterial was inserted into a beaker containing some CIP/CAP

solution volume with a specific concentration. The combination was allowed to react at a temperature of 25 °C and stirred at a speed of 500 rpm for 3 h. Then the mixture was filtered with a 0.45 m filter to collect spent nanomaterial. Then, the spent nanomaterial was rinsed mildly with distilled water before being vacuum dried. Subsequently, a specific amount of the spent sample was inserted into a beaker containing a volume of eluents. The mixture of eluent and the spent sample was vigorously stirred (1000 rpm) at the temperature set to 25 °C. 1 mL of the eluent sample was collected at a specific time (t) and filtered via 0.45 μm membrane filter for further analysis. The eluent for the desorption test was 1 M NaOH, 1 M NaCl, ethanol (EtOH), and DIW.

The CIP/CAP desorption capacities (mg/g) and desorption efficiency (%) of the nanomaterial in the eluents were calculated using Eqs. (2.22) and (2.23) [130], [131]:

$$q_{e,desorption} = \frac{V(C_f)}{m} \tag{2.22}$$

$$Desorption\ Efficiancy\ (\%) = \frac{q_{e,desorption}}{q_{e,removal}} \times 100\% \tag{2.23}$$

where $q_{e,\text{ desorption}}$ and q_e, removal specify the CIP/CAP quantity desorbed from a gram of nanomaterial sample (mg/g) and removal capacities of CIP/CAP (mg/g) at equilibrium, respectively, C_f embodies the CIP/CAP concentration in the eluent (mg/L), V and m represents the eluent volume (L), and the spent nanomaterial sample mass (g), respectively.

2.8. Analytic methods for CIP removal

A calibrated UV-vis spectrophotometer (UV-1280, Shimadzu, Japan) was operated to measure the concentration of CIP and CAP at a detection wavelength of 275 nm and 278 nm, respectively. The concentration of CIP and CAP was determined in batch and desorption experiments by the CIP and CAP calibration curve, as shown in Figure 2.4.

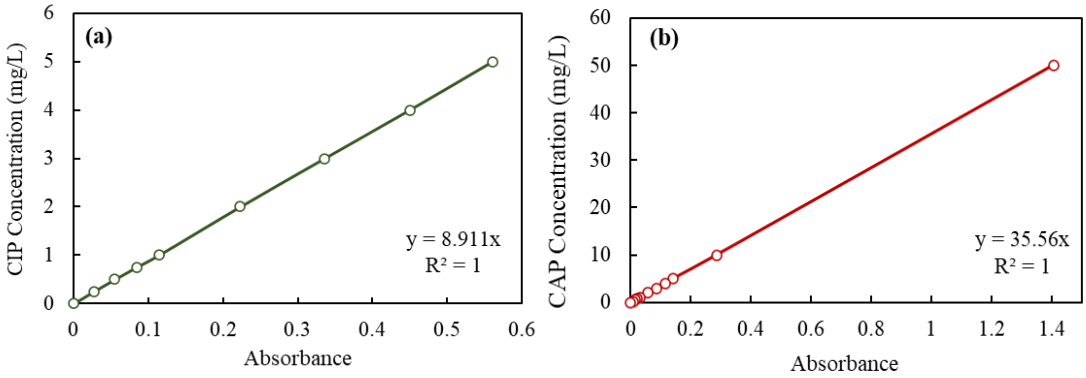

Figure 2.4. Calibration curve: (a) CIP; (b) CAP

1 M NaOH and 1 M HNO_3 solutions were used to regulate and vary the initial pH of the investigated contaminant solution in the batch experiment for exploring the impact of the initial pH of contaminant nanomaterial sample performance. The pH of the contaminant solution was measured using a LAQUA pH meter from HORIBA Advanced Techno, Co., Ltd., Japan. A UV-Vis spectrophotometer (DR3900, HACH Co., USA) was used to measure the amounts of Fe-Total and Fe^{2+}.

This page is intentionally left blank.

Chapter 3

Empirical optimization of the functional graphene-oxide nanosheets chemical synthesis for ciprofloxacin detoxification

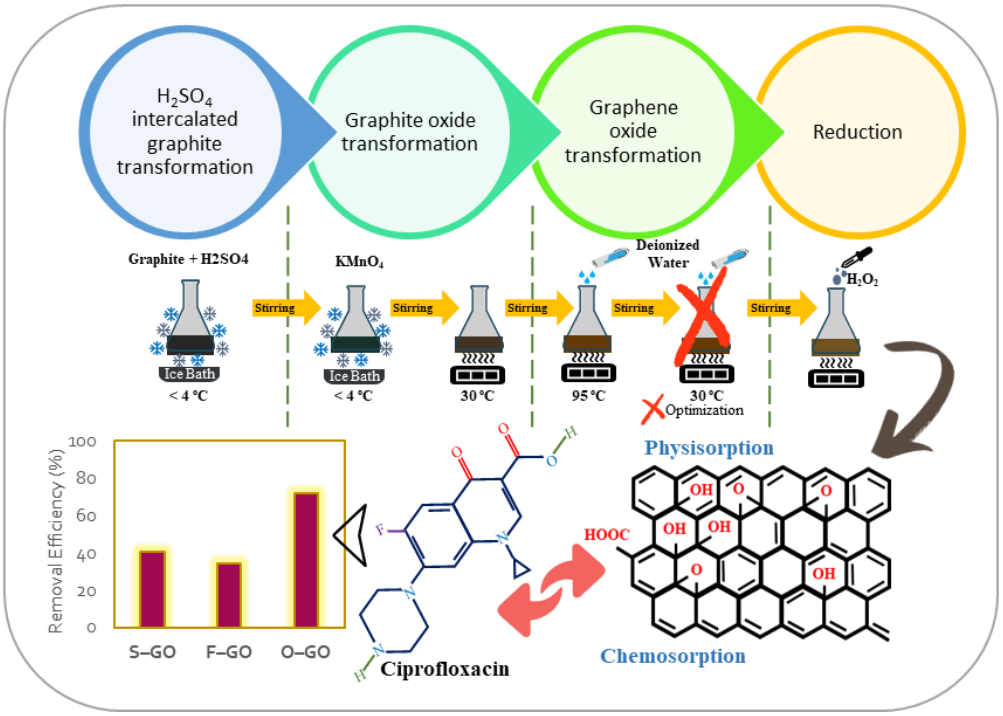

3.1. Empirically optimization of GO synthesis parameters.

3.1.1. Effect of H_2SO_4 intercalated graphite transformation (Stage 1) condition

The sulfate intercalation process of graphite, also known as the formation of graphite sulfate compound from pristine graphite by H_2SO_4, is an essential pre-oxidizing process for the graphite's initial exfoliation process. Pristine graphite comprised of multiple graphene layers is exfoliated in the mentioned process to provide a graphite compound matrix appropriate for deep penetration by the oxidizing agent in the second oxidation process. Therefore, the condition of this stage for the formation of high-performance GO for CIP removal was investigated in this study.

Figure 3.1a depicts the effect of the H_2SO_4 amount on CIP removal performance. The result demonstrates that the H_2SO_4 amount used influenced the GO performance in removing CIP. The GO with the lowest CIP removal performance was synthesized using 10 mL of H_2SO_4 as the initial oxidizing agent. The CIP removal capacity of GO reached its maximum capacity of 294 mg/g when the H_2SO_4 volume was raised to 20 and 30 mL. Increasing the amount of H_2SO_4 up to 50 mL did not further improve GO performance. However, the performance of GO against CIP removal saw a slight deterioration, with its CIP removal capacity of 289 mg/g. This trend suggests that low-volume H_2SO_4 pioneered in the sulfate intercalation process could not produce high-performance CIP removal GO. The minimum amount of H_2SO_4 increased the viscosity, inducing graphite agglomeration. Consequently, H_2SO_4 is unable to disintegrate the graphite molecular overlap, and the mechanics of HSO_4^- movement become inefficient in approaching and penetrating the entire graphite layers. Therefore, the intercalation process can be improved by increasing the dispersion of HSO_4^- ions around the graphite by increasing the volume of the H_2SO_4 solution to allow for optimal graphite oxidation and exfoliation.

The intercalation process between HSO_4^- and molecular graphite is essential to consider in the assessment of GO synthesis because the optimal time can ensure that graphite exfoliation and graphite intercalation can be accomplished with sufficient time before $KMnO_4$ carries out a stronger oxidation reaction in the second stage. Besides the amount of H_2SO_4, the agitating period for reaction in this stage affects the GO's CIP removal performance, as shown in Figure 3.1b. The GO sample recorded 256 mg/g of CIP removal capacity, whose agitating time was 5 min. The synthesized GO performance increased

considerably after the aging time was prolonged to 10 min. It achieved a CIP removal capacity of 294 mg/g and then plateaued as the agitating time increased. This trend indicates that H_2SO_4 molecules would not spontaneously intercalate with graphite molecules and need some appropriate duration for the intercalation process to be carried out perfectly.

Although the graphite intercalation process is disregarded by most researchers related to modern GO, this process is an initial independent process crucial for producing good quality GO [100], [132]. According to Li et al. [100], the process in this stage involves not only the formation of ionic compounds through the intercalation of H_2SO_4 with graphite but also the formation of a small number of functional groups containing oxygen on the base plane of the graphite sheet, affecting the performance of GO in its use. Due to its relevance in producing a suitable graphite medium for subsequent oxidation, this condition stage needs to be evaluated.

Considering the objective of this study is to optimize the GO synthesis towards time and cost-efficient oriented without compromising GO performance against CIP removal, a volume of H_2SO_4 of 20 mL and an agitating time of 10 min were chosen for the succeeding stage study.

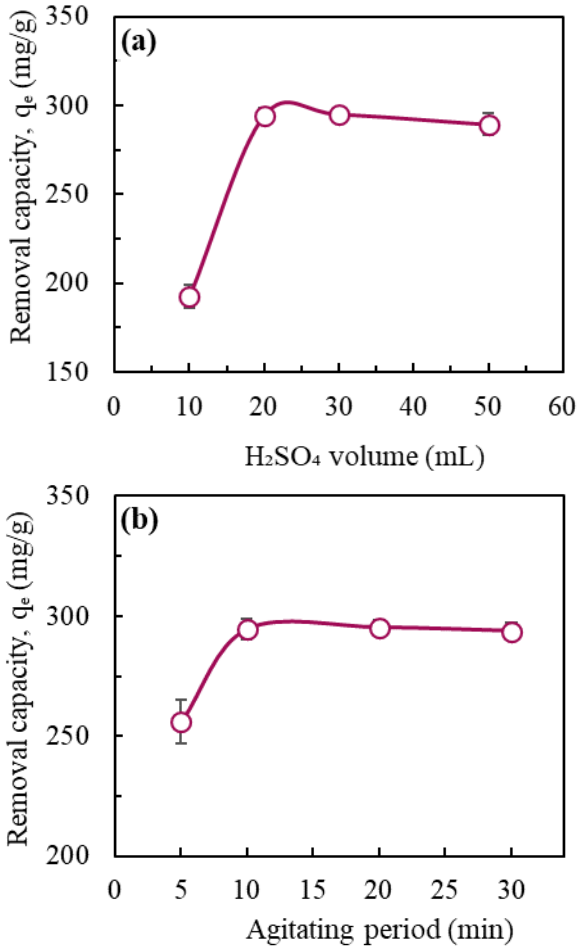

Figure 3.1. Different H_2SO_4–intercalated graphite transformation parameters on GO performance of CIP removal. (a) amount of H_2SO_4; (b) agitating period.

3.1.2. Effect of graphite oxide transformation (stage 2) condition

The second stage of GO synthesis is an essential and complex process involving the transformation of H_2SO_4–intercalated graphite to graphite oxide molecular. In this step, $KMnO_4$ was utilized as the subsequent oxidation agent in conjunction with H_2SO_4 medium to form certain radicals such as •O• and potential oxidation species such as Mn_2O_7, MnO_3^+, MnO_4^- and O_3 [100]. The formation of oxygenous functional groups during the previous intercalation process allowed for either the substitution of existing intercalant molecules or the electrophile MnO_3^+, the main oxidizing species, to diffuse into the H_2SO_4–intercalated graphite interlayer through the electron-rich environment [100], [132]. The oxidation reaction caused by the attack of oxidizing species on graphite affects the oxidation degree of the entire GO formation, which also influences the performance of GO produced for CIP removal. Therefore, several conditions in this stage,

including the amount of $KMnO_4$ and oxidation reaction times at low temperatures (<4 ºC) and 38 ºC, have been investigated, as shown in Figure 3.2, to determine the ideal synthesis for GO with excellent performance in CIP removal.

Figure 3.2a depicts the impact of the $KMnO_4$ amount used in the GO synthesis process on the CIP removal performance. It demonstrates that using 1.5 g of $KMnO_4$ chips in the synthesis produced GO with low reactivity against CIP removal, which is only as much as 138 mg/g removal capacity recorded. The removal capacity of CIP increased sharply, reaching 294 mg/g when the amount of $KMnO_4$ was increased to 3 g. Surprisingly, increasing the amount of $KMnO_4$ further to 4.5 g and 6 g did not substantially improve GO performance, where the CIP removal capacities were recorded at about 305 mg/g and 327 mg/g, respectively. This trend indicates that the GO composition and structure do not change significantly after attaining a specific threshold oxidation level, even with an excessive oxidizing agent, because the diffusion of the oxidizing agent in the graphite interlayer passage is independent of its concentration in the bulk solution [132]. In addition, the oxidized domains incorporated with reactive functional groups such as epoxy and hydroxyl groups become unsustainable in intensely oxidizing environments [100]. Therefore, this outcome suggests that 3 g of $KMnO_4$ is the optimal amount to oxidize 1 g of graphite to produce high-performance GO in removing CIP.

The penetration of the oxidizing agent ($KMnO_4$) into the graphite interlayer during oxidation requires an ideal time to ensure perfect oxidation of the graphite. In order to explore the influence of the oxidation duration at this stage on the CIP removal capacity of GO, the oxidation has been divided into two parts with different reaction conditions. In the first part, the temperature of the reaction conditions was controlled and assured to be below 4 °C by using an ice bath, while for the second part, the reaction temperature was controlled to 38 °C by using a water bath. Figure 3.2b suggests the optimal duration of the oxidation reaction (<4 °C) is 10 min (294 mg/g) since the trend of CIP removal capacity by GO plateaus after the time interval. Although $KMnO_4$ was added to the medium gradually, 5 min for oxidation was insufficient to control the abrupt temperature increase due to the exothermic reaction between $KMnO_4$ and the H_2SO_4 medium. An uncontrolled temperature increase promotes agglomeration, which decreases the degree of oxidation [119], [122] and thus affects GO performance for CIP removal. In addition,

graphite structural defects can also occur due to the carbon structure being liberated to form CO_2 [122].

For the reaction temperature set at 38 °C, Figure 3.2c demonstrates that the performance of GO against CIP removal increases with increasing reaction time. The sudden increase in CIP removal shown by the GO oxidized for 20 minutes (292 mg/g) can be explained by the increase of GO reactive site due to the spontaneous exfoliation that occurred throughout the graphite oxidation. The controlled temperature of medium and vigorous stirring produces a rapid surge, thus accelerating the exfoliation and oxidation of graphite, contributing to the increase in CIP removal. However, extending the reaction time to 30 min and 60 min contributed only to a minimal increase, with the GO's CIP removal capacity recorded as much as 294 mg/g and 296 mg/g, respectively. According to Yuan et al. [119], increasing the oxidation period reduces the reactive OCFG, where this group can interact with nucleophilic species and potentially benefit numerous applications.

Based on the findings discussed in this section, the optimal synthesis conditions, particularly in the graphite oxide transformation stage, are by using 3 g of $KMnO_4$ for oxidizing 1 g of graphite at a reaction temperature below 4 °C for 10 min, followed by a reaction at a controlled temperature of 38 °C for 20 min. These parameters were retained to optimize the subsequent stages of GO synthesis.

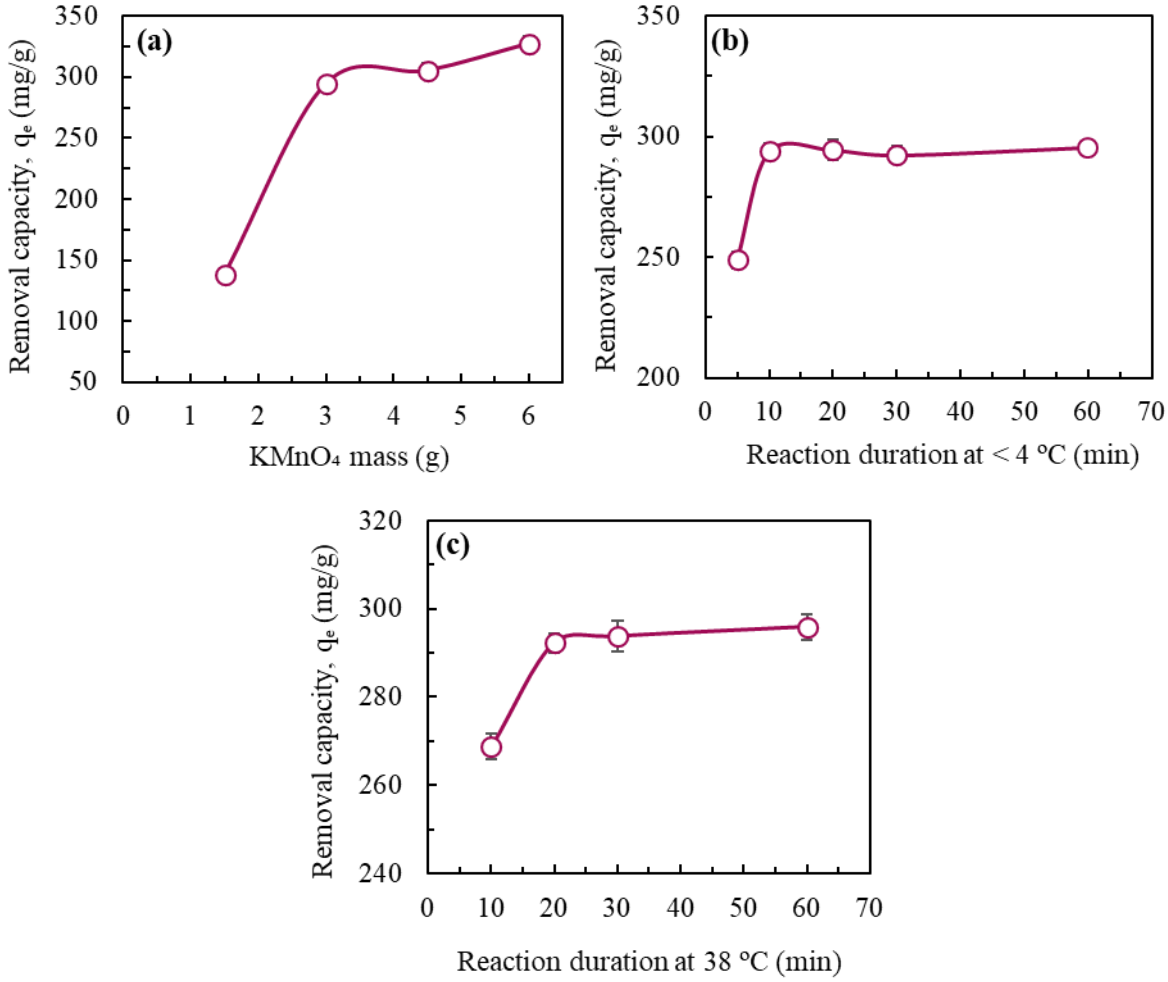

Figure 3.2. Different graphite oxide transformation parameters on GO performance of CIP removal. (a) amount of $KMnO_4$; (b) reaction duration at < 4°C; (c) reaction duration at 38°C.

3.1.3. Effect of graphene oxide transformation (Stage 3) condition

In this stage, the medium consisting of bulk oxidized graphite was further exfoliated to single-layer GO sheets by hydrolyzing with DIW before the compound was heated to 95 °C. This stage also includes the hydrolysis of covalent sulfates, which serve as protective groups and alter oxygen functionalities [132]. The acidic condition of the compound catalyzes the epoxide functional group's hydrolysis to generate hydroxyl functional groups, which are preferable and favorable in some applications [100]. Furthermore, the oxygenous functional groups such as hydroxyl, carboxylic acid, epoxide, and ketone can induce hydrogen bonds with water molecules, improving sample hydrophilicity [119]. The combination of heating and vigorous stirring of the compound could generate a high-speed H_2SO_4-$KMnO_4$ stream and accelerate the diffusion of oxidizing agents in the

interlayer of graphite oxide [119]. Since this stage directly affects the graphite exfoliation and oxidation, the DIW amount and aging duration at the compound temperature of 95 ºC have been investigated for their impacts and optimized to produce a high-quality GO for CIP removal.

Figure 3.3a shows the effect of the amount of DIW used in GO synthesis, specifically in the GO transformation stage, on its performance for removing CIP. Synthesis of GO with 25 mL DIW yielded a GO with a CIP removal efficiency of 251 mg/g. The performance of GO then shows an improvement, reaching 292 mg/g of CIP removal capacity, with higher addition of DIW to 50 mL. The increasing trend of CIP removal by GO might be attributed to the high-speed H_2SO_4-$KMnO_4$ stream generated due to the mixture viscosity reduction when DIW was added, leading to an increase of the oxidant diffusion degree to generate more reactive sites on the GO surface [119]. However, the performance of GO decreased slightly when the amount of DIW was doubled to 100 mL. A high amount of DIW at a high temperature increases the system's heat capacity, which causes oxidation inhibition by thermal-sensitive oxidizing species, such as Mn_2O_7 [100]. Thus, from this finding, 50 mL of DIW is ideal and adequate to produce GO with good CIP removal performance.

Figure 3.3b shows the effect of the agitating period at 95 ºC on the performance of GO in removing CIP. No significant change in GO performance was observed when the sample was agitated for 5 and 10 min, with CIP removal capacities of 291 mg/g and 292 mg/g, respectively. When the aging time was prolonged to 20 min, the removal of CIP by GO increased (295 mg/g), but the increase can be considered minimal. On the other hand, when the agitating time was extended up to 40 min, the performance of GO in removing CIP deteriorated, reaching 281 mg/g. This deterioration occurs because the oxidation rate is challenging to regulate. High compound temperatures can lead to side effects on reactive functional groups, agglomeration, and over-oxidization, especially when exposed for a lengthy period [122]. Due to the high surface energy, the GO hexagonal structure might decompose, forming CO_2 when exposed to high temperatures in an acidic environment over a long period [122]. These stated factors influence the performance of GO for CIP removal. Based on this finding, the shortest reaction period, 5 minutes, is chosen as the optimal period for GO synthesis because it saves time and cost.

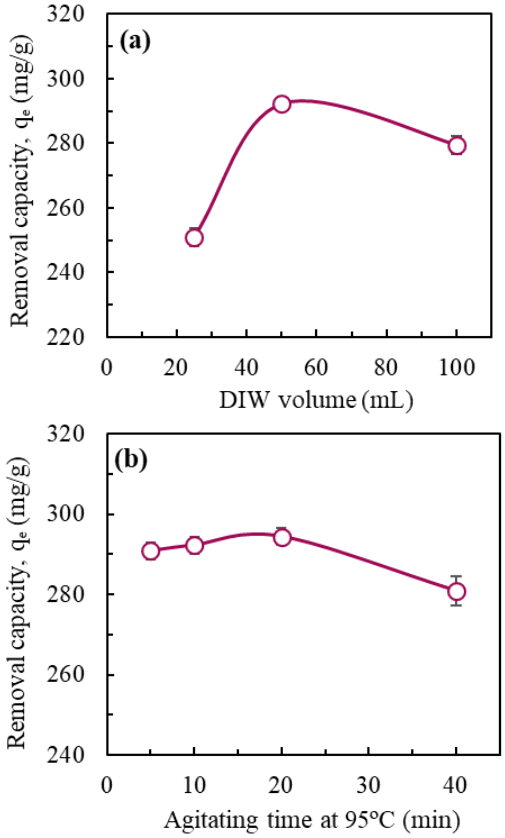

Figure 3.3. Different graphene oxide transformation parameters on GO performance of CIP removal. (a) amount of DIW; (b) agitating time at 95°C.

3.1.4. Effect of reduction (Stage 4) condition

The reduction is one of the primary processes applied in synthesizing GO, purposely to complete the reaction. For this reason, 30% H_2O_2 solution is commonly used as a reductant by most researchers in altering the standard Hummer method to eradicate and transform the residual MnO_4^- and MnO_2 to colorless manganese sulfate ($MnSO_4$). H_2O_2 is a nonplanar molecule with C_2 chemical symmetry distortion, which can cause an interaction between H_2O_2 hydroxyl radicals and the GO disrupted π-conjugated double bonds plane, inducing numerous π-conjugated carbon radicals on GO. Excessive H_2O_2 usage might affect the chemical structure of GO and its properties, which leads to the diversity of GO's performance in various applications. Based on this fact, a range of H_2O_2 solution amounts used in GO synthesis was considered in evaluating their impact on the GO performance for CIP removal.

The effect of using different amounts of H_2O_2 in the final stage of GO synthesis on CIP removal performance is shown in Figure 3.4. The GO synthesized using 3 mL of H_2O_2 shows a higher CIP removal performance (291 mg/g) than without H_2O_2 (262 mg/g). However, the CIP removal performance slightly deteriorated to 284 mg/g when 6 mL of H_2O_2 was used. The decrease in CIP removal performance (265 mg/g) becomes apparent when H_2O_2 is doubled to 12 mL. The result suggests that using H_2O_2 is relevant in synthesizing high-performance GO, and the trend supports the hypothesis that adding H_2O_2 at a certain amount in GO synthesis substantially influences GO's performance of CIP removal. The amount of H_2O_2 plays a role in changing GO properties, which agrees with the finding by Park et al. [123]. Using H_2O_2 in the synthesis causes GO to be degraded by gaining hydroxyl groups. In addition, Park et al. [123] found that increasing the amount of H_2O_2 used for reduction leads some functional groups, such as carboxylic acid and ether, to decompose. The presence and lack of these functional groups in the chemical structure of GO affect its efficacy in CIP removal applications in polluted water.

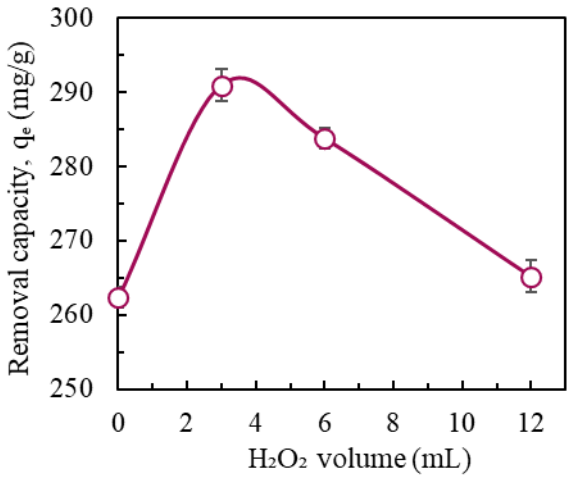

Figure 3.4. Different reduction parameters on GO performance of CIP removal.

3.2. CIP removal profiles of GO samples

Two other GO samples, S–GO and F–GO, were prepared to compare their performance in CIP removal with the GO presented in this work (O–GO), and their removal profiles as a function of time are shown in Figure 3.5. The dramatic incline in removal efficiency indicates the rapid CIP removal exhibited by all GO samples within the first 10 min. Then, the removal profiles plateaued at 30 min of reaction, suggesting that the CIP removals had reached equilibrium. All the samples showed different performances despite being

made of the same material. The CIP removal performance of S–GO is slightly higher than that of F–GO, achieving 34 % and 40 % removal efficiencies at 3 hours, respectively. Nevertheless, the O–GO has a vastly more outstanding removal performance, with a removal efficiency of 72 % in the same period.

These trends demonstrate that the variables of GO synthesis have a diversified impact on its performance, particularly in treating CIP-contaminated water. For instance, it can be observed in the F–GO performance. Cao et al. [115] reported that GO functionalized by H_3PO_4 has an excellent performance in removing copper for water remediation. However, this research discovered that employing H_3PO_4 as an additional oxidation catalyst in GO synthesis provided no advantages in the CIP removal, and the efficiency was even worse than S–GO. H_3PO_4 decomposed and generated various oxygenated functional groups, which may have a preferential attraction towards ionic contaminants. This situation led to the weak electrostatic attraction between GO and CIP, thus affecting its removal performance.

The more promising O–GO's performance, with a nearly 30 % increment in CIP removal efficiency compared to S–GO, proves that the optimization process to produce superior GO for its applications is essential and needs to be emphasized. The ideal combination of the materials amount and synthesis period thread is the primary key to producing favorably efficient GO. The appropriate synthesis period can ensure that graphite is not over or under-oxidized to generate an appropriate GO character for CIP adsorption or removal. The variable combination of oxidants amount, the aging period, and the ambient conditions of the reaction medium with temperature control and vigorous stirring lead to graphite structure deformation, which may promote high exfoliation intensity [122]. This occurrence makes the synthesized GO have a heterogeneous structure with high-intensity oxidation on both the edge and internal provinces. CIP has two functional groups, charged and electro-deficient π-structures, which can react with the functionalized GO edges and the aromatic structure inside GO basal planes, thus making the GO highly reactive toward CIP [133]. Furthermore, as explained in the preceding subtopic, the role of the reduction stage is crucial and contributes to GO's efficiency in CIP removal. The use of H_2O_2 with an arbitrary amount by most researchers not only decomposes the preferred functional group for attracting contaminants but may even cause surface passivation [123].

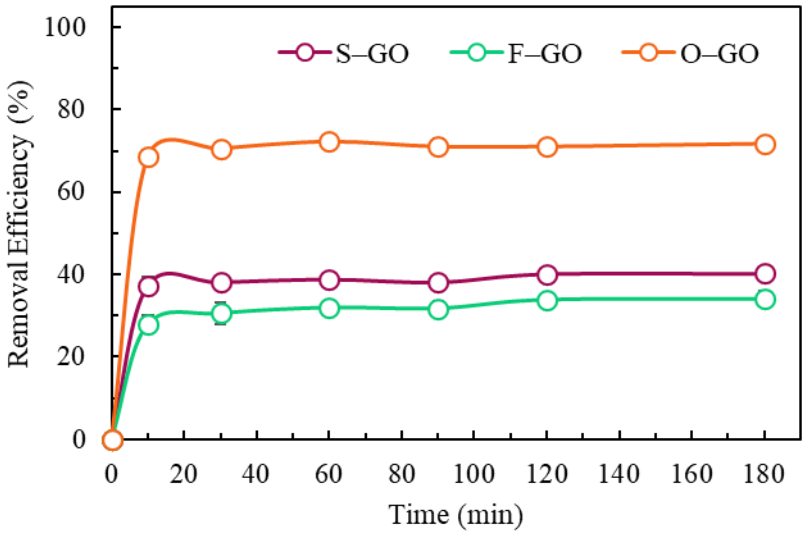

Figure 3.5. Performance of different synthesized GO nanosheet samples on CIP removal.

3.3. CIP removal conditions optimization assessments

3.3.1. Dosage optimizing on CIP removal

The optimal dosage of the O–GO is crucial to be studied because this condition can provide good cost management and facilitate material usage control in actual water treatment applications. Thus, a series of the O–GO dosage in the range of 0.1–1 g/L was studied on CIP removal performance, and its removal profile within 3 h of adsorption is illustrated in Figure 3.6. All other experimental variables were kept constant: the CIP initial concentration of 100 mg/L, nature pH_0 6.2, and temperature of 25 ºC. The findings indicate that increasing the O–GO dosage increases the CIP removal efficiency. CIP was effectively removed with an efficiency of up to 36 % by a low dosage of O–GO (0.1 g/L). By O–GO dosages of 0.25 g/L and 0.5 g/L, removal efficiency rose significantly, attaining 72 % and 93 %, respectively. Furthermore, O–GO with a dosage of 0.6 g/L achieved more outstanding CIP removal with an efficiency of up to 97 %. CIP removal efficiency increases due to more active and available adsorption sites when O–GO dosage increases [14], [131]. However, O–GO performance showed a minimal and insignificant increase in removal efficiency (98–99%), even though the dosage was boosted to 0.75 g/L and 1 g/L. Although both doses indicate outstanding CIP removal efficiency, the difference in removal efficiency compared to O–GO, dosed at 0.6 g/L, is nominal, and those dosages are unprofitable to be applied. Using O–GO dosed at 0.6 g/L is more pragmatic and

beneficial from the material cost perspective. Therefore, by considering these factors and without compromising CIP removal performance, the ideal removal efficiency that O–GO can attain is at a dosage of 0.6 g/L.

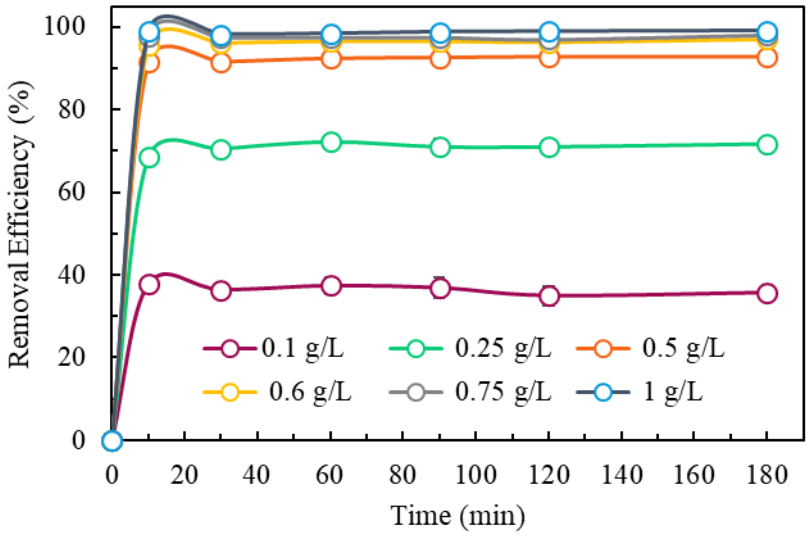

Figure 3.6. The CIP removal efficiency (%) of O–GO at different dosages.

3.3.2. Effect of initial pH on CIP removal

It is essential to evaluate the pH effect on CIP removal because the initial pH of the CIP solution can effectively change the existing speciation (dominant species) of CIP and could affect the surface properties of O–GO. Hence, a batch experiment was performed to investigate the pH effect on O–GO performance in CIP removal at pH 3–11, and the outcomes are shown in Figure 3.7. The results demonstrate no substantial difference in CIP removal efficiency (97–98 %) after 3 h of reaction in the CIP solution with initial pH 5–9, implying that the ideal performance of O–GO for CIP removal can be achieved in the medium with the initial pH range. On the other hand, the CIP removal performance was impaired and deteriorated when the CIP solution was excessively acidic or too alkaline. For the CIP solution with a pH of 3, the CIP removal performance showed a slight drop, with a removal efficiency of about 90 % after 3 h of reaction. Curiously, at pH 11, the removal efficiency of CIP was 98 % at the beginning of the reaction (10 min) but then gradually decreased until a removal efficiency of 83% was reached at 3 h.

The pK_a values of CIP are 5.9 and 8.89 [134]. These values show the dominance of different CIP species in the pH range analyzed in this study, whereby in the pH range of

5.9–8.89, CIP species are mainly present in the zwitterionic form ($CIP^{\pm}$). On the other hand, CIP was dominated by species that presented in cationic (CIP^{+}) and anionic (CIP^{-}) forms at pH < pK_a =5.9 and pH > pK_a =8.89, respectively. At pH 3, part of the alkyl carboxyl (COOH) functional group typically located on the GO surface was protonated to a natural charge ($COOH^0$). In contrast, CIP is presented mainly in the form of CIP^{+}, weakening CIP's electrostatic attraction to the O–GO surface. This situation explains why the CIP removal efficiency at pH 3 was lower than at CIP neutral pH. When the initial pH was raised to pH 5, 80 % of the O–GO carboxyl groups were deprotonated and became negatively charged (COO^{-}). At the same time, CIP^{+} remained dominant in the CIP solution, with its relative distribution getting less, and $CIP^{\pm}$ started to emerge [10], [135]. This tendency makes pH 5–9 more favored for CIP adsorption in water remediation. In strongly alkaline conditions (pH 11), the CIP solution was dominated by CIP^{-}. O–GO removed almost 98 % of CIP at the beginning of the reaction. However, due to the pH being excessively alkaline, the surface of O–GO covered with carboxyl groups was deprotonated and negatively charged (COO^{-}) along the reaction. Thus, the CIP removal efficiency was reduced at this pH, and CIP desorption took over due to electrostatic repulsion between O–GO and CIP^{-}. This finding gives an initial impression that the suitability of the media for desorption and O–GO regeneration is an alkaline media.

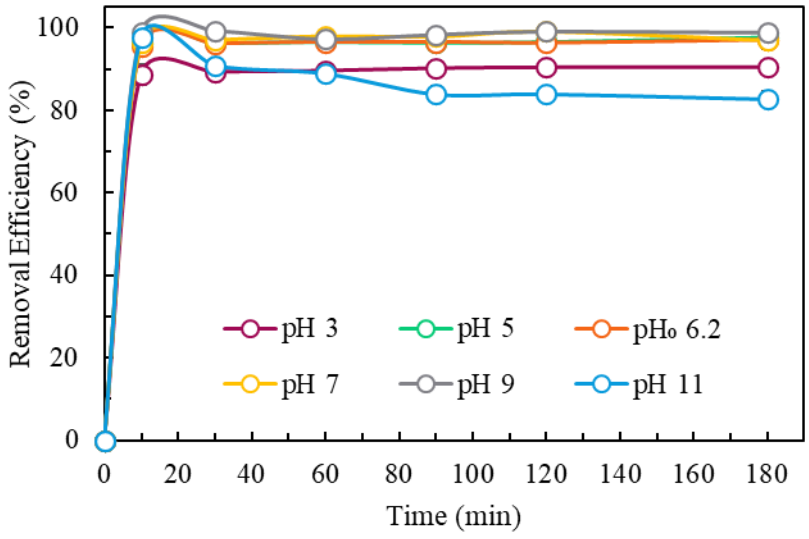

Figure 3.7. Effect of pH on CIP removal efficiency (%) of O–GO.

3.3.3. Effect of initial concentration on CIP removal

A batch experiment was conducted to study the effect of the initial concentration of CIP solution, ranging from 10–150 mg/L, on the O–GO performance in CIP removal. 0.25 g/L and 0.6 g/L dosages of O–GO were used for this purpose, and their performance on CIP removal at different concentrations for both dosages is shown in Figure 3.8a and Figure 3.8b. Both dosages demonstrate that the CIP removal is inversely proportional to the initial concentration of CIP. More than 92 % of low-concentration CIP (10, 25, and 50 mg/L) was removed within 10 min, and almost 100 % of CIP was removed within 60 min by only 0.25 g/L O–GO dosage. The presence of abundant and excess CIP molecules in the aqueous solution accelerated the transfer of CIP mass onto the reactive site of GO [28]. Instead, the efficiency of O–GO decreased to 80 % and 72 % when the initial concentration of CIP increased to 75 mg/L and 100 mg/L. However, when the O–GO dosage was increased to 0.6 g/L, more than 97 % of CIP could be removed for both CIP concentrations within 60 min. On the other hand, the removal efficiency decreased slightly when the CIP concentration was increased to 125 mg/L and 150 mg/L, respectively, to 90 % and 84 %. The trend shows that the removal of CIP decreases when the initial concentration increases, and the increasing O–GO dosage enhances the CIP removal for high-concentration CIP. It is also consistent with the findings reported by previous researchers using different adsorbents or materials and different pharmaceutical contaminants [45], [84], [136]–[138]. The fundamental explanation for the decrease in removal efficiency with increasing CIP concentration is the restricted and decreased availability of adsorbent sites on the O–GO surface owing to CIP saturation [28], [137]. Thus, increasing the O–GO dosage can improve the active site's availability for good adsorption of CIP with high concentration. From the economic perspective, this work found that O–GO with a low dosage (0.25 g/L) is more profitable for the remediation of water with low CIP contamination, but O–GO with a higher dosage (0.6 g/L) is recommended for the remediation of water with high CIP contamination.

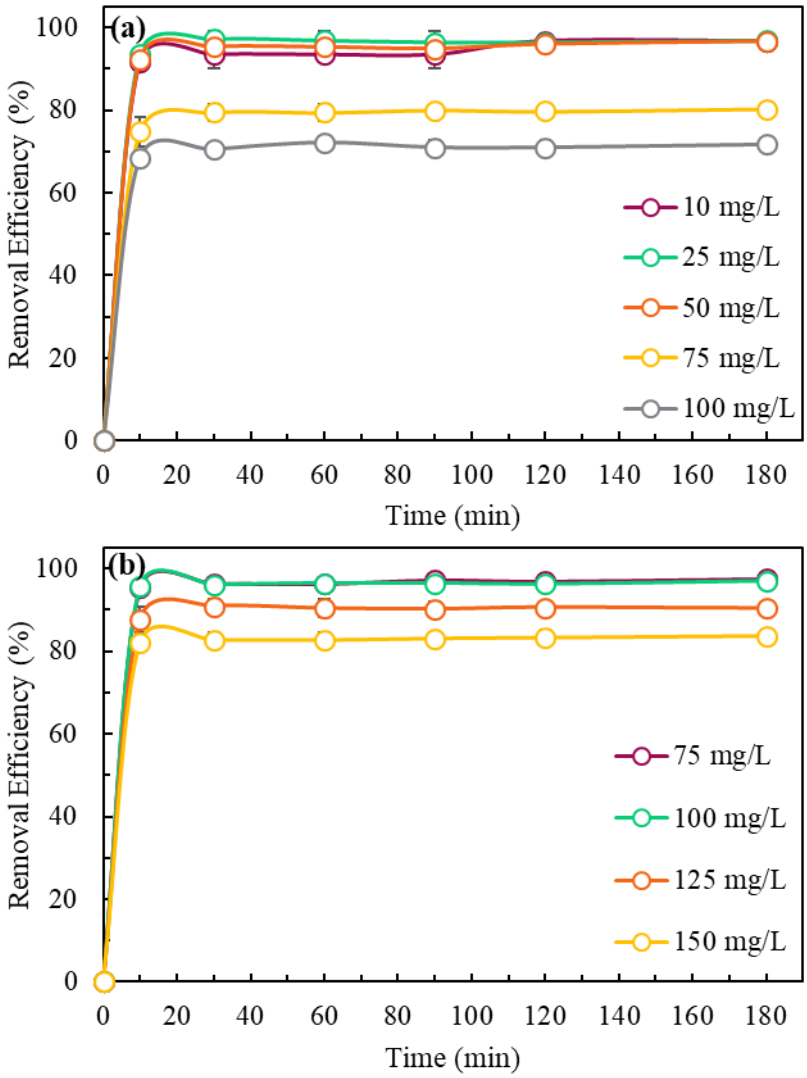

Figure 3.8. The performance of O–GO on CIP removal at different concentrations and dosages: (a) 0.25 g/L; (b) 0.6 g/L.

3.3.4. Kinetics study

The adsorption mechanism and the role of the active site on the O–GO surface were characterized by the fit of kinetics data with 4 models, including PFO, PSO, intraparticle diffusion, and Elovich models, as shown in Figure 3.9. The experimental plots indicate a remarkable resemblance to the plotting of the PFO, PSO, and Elovich models. In contrast, the plotting between the experimental value and the intraparticle diffusion model is qualitatively feeble and imprecise.

The value of the model's regression correlation coefficient (R^2) is one of the kinetic variables that can be calculated and evaluated to determine the compatibility between the

models and the experimental kinetic profile in more detail. The greater the R^2 value, the closer the experimental data and the model are [75][115]. Moreover, the Akaike information criterion (AIC) coefficient was computed to define the quality of each model through a statistical approach to deciding the fit model [127], [131]. Table 3.1 summarizes the CIP removal capacity acquired from experimental and modeling approaches and the R^2 and AIC coefficients of the CIP removal kinetics profile at various initial concentrations. The Elovich model has a greater R^2 (0.9993) coefficient in the 10 mg/L CIP initial concentration kinetics profile than other models, indicating heterogeneity of the O–GO sorption sites, especially at low CIP initial concentration. On the other hand, the experimental data of 25 mg/L CIP fit well with the PFO kinetic model because of the enormous R^2 coefficient value (1.0000), implying that the CIP removal mechanism might be controlled by physisorption, such as electrostatic attraction, Van der Waals bonding, and co-precipitation [28]. In contrast, the PSO and Elovich models more suitably represent the kinetic profile of 50 mg/L CIP because both R^2 coefficients show the highest values. However, evaluating the lowest AIC coefficients for both models shows that PSO is more compatible than the latter. In addition, the same PSO model matches the kinetic profile for the CIP at higher initial concentrations (75 mg/L and 100 mg/L), with R^2 coefficient values of 0.9999 and 0.9998, respectively, suggesting the possible removal mechanism was chemisorption [139], [140]. The outcomes of this study explain that the initial concentration of CIP has various impacts on CIP removal behavior and influences its removal mechanism.

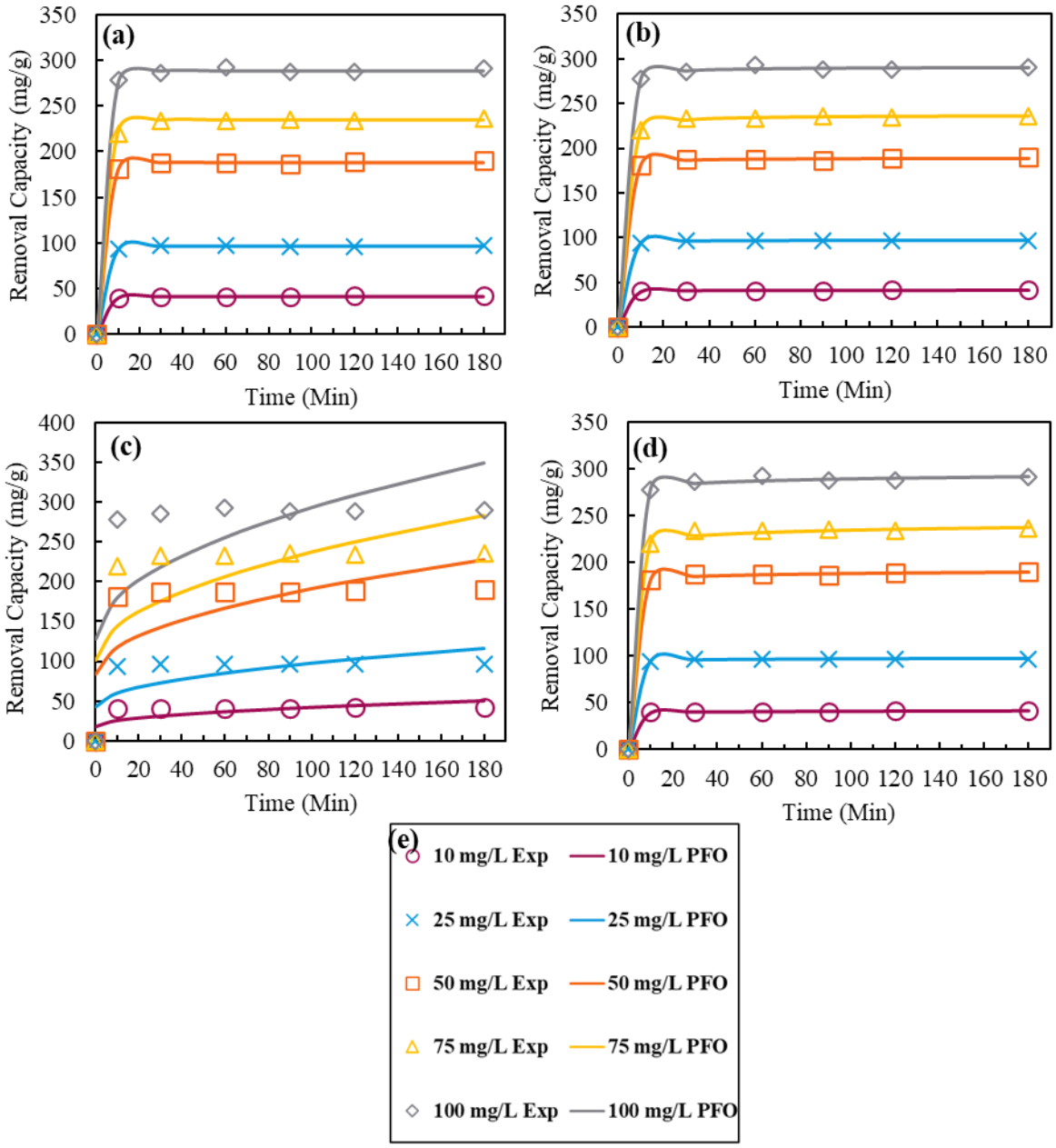

Figure 3.9. Experimental data fittingness of O–GO on kinetics model: (a) Pseudo-first-order (PFO); (b) Pseudo-second-order (PSO); (c) Intraparticle diffusion; (d) Elovich models; (e) legend.

Table 3.1. Experimental data and kinetic parameters of different models for CIP removal by 0.25 g/L of O–GO.

CIP initial concentration (mg/L)	Experimental Data	Pseudo first-order				Pseudo second-order model				Intraparticle diffusion model					Elovich Model				
	Removal capacity (mg · g^{-1}), $q_{e,\,exp}$	q_e,cal (mg · g^{-1})	K_1 (min^{-1})	R^2	AIC_c value	$q_{e,cal}$ (mg · g-1)	K_2 (g · mg^{-1}· min^{-1})	R^2	AIC_c value	$q_{e,cal}$ (mg · g^{-1})	C_{intra} (mg · g^{-1})	K_{intra} (mg · g^{-1} · min$^{1/2}$)	R^2	AIC_c value	$q_{e,cal}$ (mg · g^{-1})	α (mg · g^{-1} · min^{-1})	β (mg · g^{-1})	R^2	AIC_c value
10	42.06	41.21	0.35	0.9983	6.62	41.52	0.0540	0.9988	4.50	50.03	18.00	2.39	0.5104	46.31	41.81	1.07E+23	1.401	0.9993	0.46
25	96.60	96.52	0.34	1.0000	-6.80	96.96	0.0298	0.9998	4.09	116.21	43.26	5.44	0.4836	58.58	97.04	2.11E+44	1.106	0.9995	10.33
50	190.34	188.20	0.34	0.9997	15.04	189.36	0.0128	0.9998	12.71	227.43	83.27	10.75	0.4969	67.75	190.04	4.61E+30	0.394	0.9998	14.24
75	236.14	234.55	0.31	0.9996	21.10	237.01	0.0057	0.9999	13.92	283.53	101.68	13.55	0.5126	70.56	237.91	8.69E+18	0.198	0.9992	26.00
100	290.86	289.15	0.33	0.9996	24.42	291.15	0.0073	0.9997	22.75	349.04	128.00	16.48	0.4955	73.77	291.94	4.30E+29	0.247	0.9994	26.91

3.3.5. Effect of temperature and activation energy of CIP removal

The interactive effect between the temperature of the CIP solution and CIP removal behavior by O–GO is shown in Figure 3.10. The solution's temperature does not significantly impact the CIP removal. As depicted in Figure 3.10a, the removal efficiency does not vary significantly, and the values still display an excellent value, exceeding 95 %, even though the solution temperature was increased to 65 ºC and maintained for 180 min. It demonstrates that O–GO is stable for CIP removal without being affected by the medium's temperature. Even so, a slight distinction in the removal behavior is noticed at the beginning of the reaction (10 min) and 180 min, as illustrated in Figure 3.10b. At 10-min intervals, increasing the temperature of the solution led to a decrease in the concentration of CIP, indicating an increase in the adsorption of CIP by O–GO. The increase in temperature at the beginning of the reaction has brought more CIP molecules in the bulk solution to move turbulently in contact with the adsorbent and accelerate the diffusion rate of contaminant molecules into the boundary layer and internal pores of the adsorbent. Hiew et al. [103] also reported that an increase in temperature reduces the thickness of the boundary layer around the adsorbent, thus reducing the mass transfer resistance of contaminants in the boundary layer. In addition, this trend suggests that the CIP adsorption process by O–GO at the beginning of the reaction was endothermic, which used energy for the increase in CIP adsorption. However, the nature of CIP removal changed when the reaction time was extended to 180 min, where the concentration of CIP increased as the temperature increased. The high temperature provided sufficient energy input to disrupt the relatively low-strength adsorption bonds between the adsorbent and the contaminant [28]. This factor led to the current CIP concentration at the time interval of 180 min increasing at high temperatures.

In addition, the activation energy (E_a) of CIP adsorption onto O–GO can be determined from the Arrhenius equation as shown in Eq. (3.1)[141], [142]:

$$-\ln k_2 = \frac{E_a}{RT} + \ln A \tag{3.1}$$

Where k_2 (g/mg/min) represents the apparent rate constant obtained from the PSO kinetics model, E_a (kJ/mol) indicates the activation energy of the adsorption, T (K)

denotes the absolute temperature of the solution, R (8.314 J/mol/K) and A (g/mg/min) is defined as the molar gas constant and the Arrhenius exponential factor, respectively. The slope of the linear plot of ln k_2 versus $1/T$ was calculated to define the E_a. The reciprocal of temperature coordinated well with the natural logarithm of the rate constant (R^2 = 0.993), as shown in Figure 3.10c, and the determined E_a value is 17.9 kJ/mol. This E_a value gives a statistical indication of the working removal mechanism of CIP by O–GO either physically (physisorption) or chemically (chemisorption). The low E_a value (<40 kJ/mol) indicates the characteristics of the physisorption removal mechanism, whereas the reaction with a high E_a value (40< E_a <800 kJ/mol) suggests that adsorption occurs by chemisorption [28], [81], [86], [143], [144]. Some researchers used different scales to determine the adsorption mechanism. For instance, Bin et al. [145] and Romero-González et al. [146] determined that the E_a value for chemisorption is greater than 8 kJ/mol. However, the former scale is more relevant and has been most reported. Thus, the E_a value determined in this study suggests that physisorption may affect the operating mechanism. The Van der Waals force can justify this physisorption between the adsorbent and CIP.

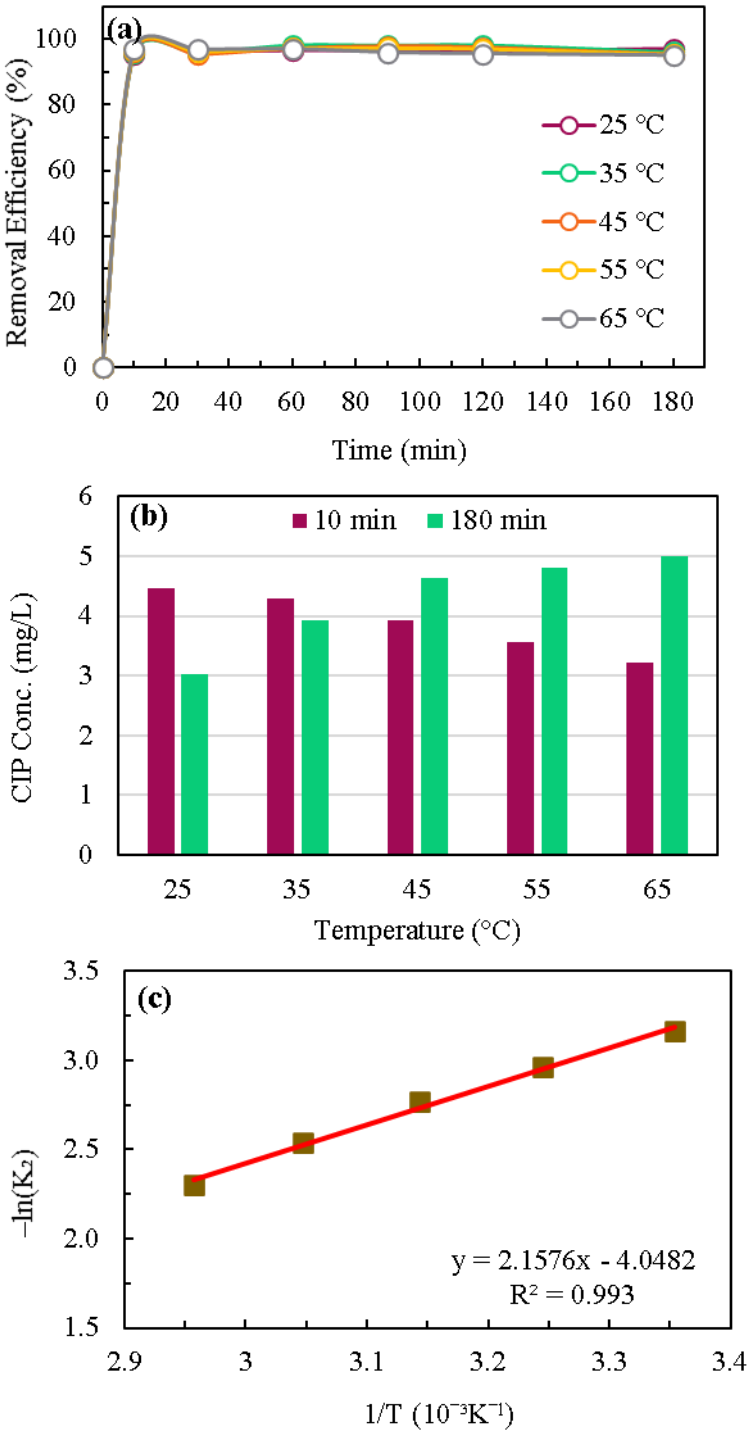

Figure 3.10. Effect of temperature on O–GO performance in CIP removal: (a) kinetics profile; (b) removal profile at the beginning and 180-min interval; (c) Arrhenius plot.

3.4. Desorption analysis

A desorption study is essential for its application in adsorbent regeneration or recycling and is also helpful for comprehending and verifying the CIP removal mechanism.

Therefore, CIP desorption behavior has been explored in this work by implementing a series of batch desorption experiments in various eluents. Figure 3.11a depicts the profiles of CIP desorption capacity in four distinct eluents over 2 h of contact time. The findings indicate that CIP desorption in different eluents occurs in distinct trends. CIP desorption occurred rapidly and was stable in NaOH solution, reaching almost 150 mg/g desorption capacity and equilibrium within 5 min. In comparison, the desorption of CIP began in NaCl solution with a lower capacity in the same period of reaction (5 min), which was recorded as much as 34 mg/g, and gradually rose to 53 mg/g at a 120 min period. However, the CIP desorption capacity in the EtOH solution fluctuated, resulting in a distinct desorption profile trend from other eluents. This trend implies a combination of desorption and adsorption mechanisms occurred during the 120 min reaction. On the other hand, the finding suggests that using DIW as a desorption eluent is impracticable because the desorption capacity recorded a meager value (<1.5 mg/g) throughout the 120 min reaction. These eluents exhibit various desorption effects on CIP because each eluent plays an essential role in breaking the bond between the adsorbent and contaminants, depending on several aspects, including the compatibility of the adsorbent and contaminant, the adsorbent sensitivity to the environment, complexing ability, pH and organic modifier content of eluents [131], [147].

Figure 3.11b depicts the CIP desorption performance by various eluents at 2 h and 24 h reaction intervals. It shows that NaOH has higher CIP desorption efficiency than NaCl, EtOH, and DIW, proving its high suitability for regenerating adsorbent. This finding has also been proven experimentally and strengthens the findings from the kinetic analysis that the adsorption mechanism predominantly contributed to the CIP removal mechanism because >75 % and almost 83 % of adsorbed CIP was desorbed from O–GO in NaOH solution at 2 h and 24 h, respectively. In contrast, the NaCl solution shows a lower CIP desorption efficiency than NaOH, while the EtOH solution only recorded 16 % of desorption efficiency after 24 h reaction, with essentially no desorption occurring at 2 h reaction as in DIW.

The pH factor of the eluents is the most crucial parameter in desorption efficiency because both adsorbent and CIP charge can transform in different pH conditions. Thus, using NaOH as an eluent has contributed to the higher CIP desorption efficiency because the alkaline nature of the solution can deprotonate CIP and O–GO charges to generate CIP^-

and COO^-, respectively, forming electrostatic repulsion to split the bond [148]. This situation promoted desorption while also weakening adsorption, revealing strong agreement with the findings discussed in the section on the effect of pH on CIP removal. In addition, the presence of OH^- ions in large concentrations initiated numerous hydrates that allowed the separation of the soluble bonds of CIP with the adsorbent [147]. NaCl solution containing Cl^- ion is beneficial for the desorption of some complex contaminants because this ion is usually capable of interacting with the O–GO to release CIP molecules [130], [131]. This reason justifies the contribution of NaCl as a desorption agent to CIP desorption. Furthermore, CIP desorption occurred at low efficiency in the EtOH solution because low hydroxyl groups can form hydrogen bond competition with CIP on the O–GO surface [131].

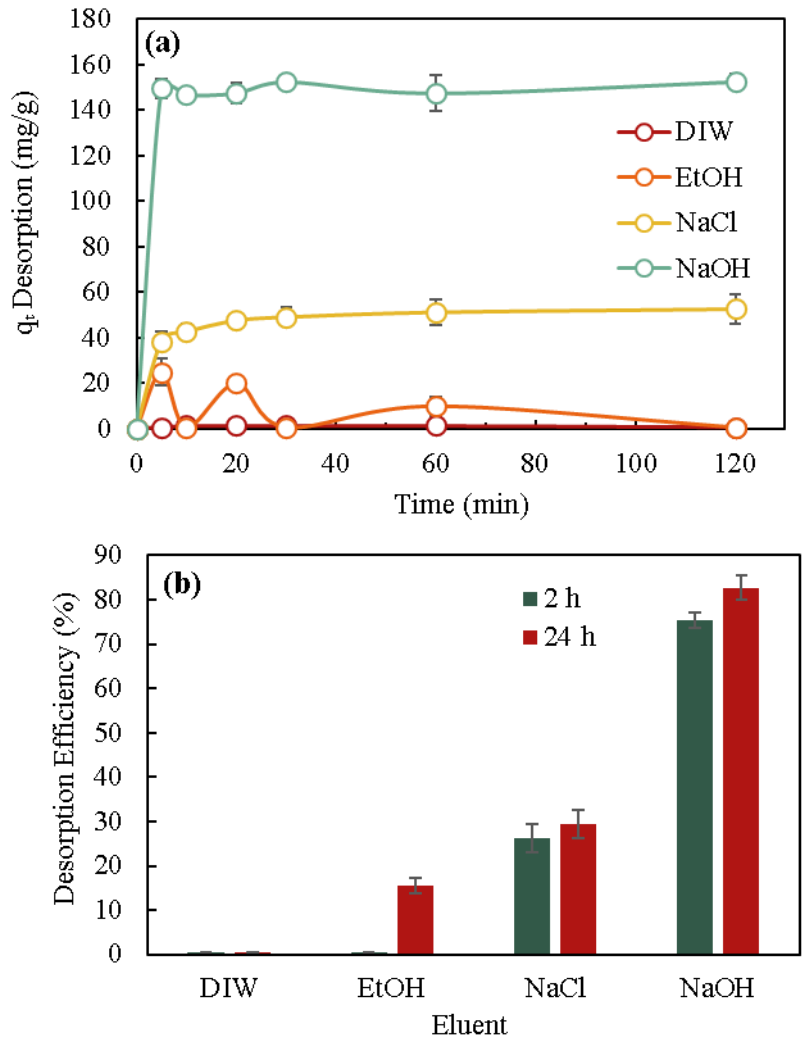

Figure 3.11. CIP desorption analysis of O–GO by different eluents: (a) CIP desorption capacity of O–GO over 3 h of contact time; (b) CIP desorption efficiency of O–GO at 2 h and 24 h.

3.5. Cost analysis

The production cost of a material is essential, especially in today's increasingly challenging global economic situation. Several factors affect the total production cost of GO, such as labor cost, energy, equipment and facilities, logistics and transportation, and production scale. However, the first and most crucial cost factor to consider in figuring out the entire production cost of a product is materials. Therefore, this study analyzed the cost of materials used in GO production and assessed the impact of that cost on the performance of the GO produced. In addition, the present study also emphasizes the synthesis period factor as a means to estimate the GO production costs, owing to its

potential correlation with energy consumption. The duration of material synthesis is directly proportional to the associated energy cost.

Table 3.2 summarizes the material costs for each GO synthesized. O–GO has the lowest material cost (¥95.7583), followed by F–GO (¥117.7771), while S–GO has the highest material cost (¥404.8917). However, the cost figure shown is a preliminary estimation of the material cost for the synthesis, regardless of the GO amount produced. Each synthesized GO has a different dry weight and CIP removal capacity. Thus, to be more accurate in evaluating the relevance of the material cost to the GO performance in CIP removal, the following Eq. (3.2) was used to estimate the material cost for removing 1 mg of CIP from the aqueous.

$$Material\ cost\ of 1\ mg\ CIP\ removal\ = \frac{Material\ cost\ of\ 1\ g\ GO}{q_{e,\ removal}} \tag{3.2}$$

Where $q_{e\ removal}$ is the equilibrium removal capacity (mg/g), and the material cost of 1 g of GO was acquired by dividing the cost of the primary raw materials used in GO synthesis by the weight of GO produced.

Table 3.2. The material costs of each synthesized GO

Raw material	**Price per unit**	**Material Cost**		
		S–GO	F–GO	O–GO
Graphite Powder	9.6000 ¥/g	¥ 9.6000	¥ 9.6000	¥ 9.6000
H_2SO_4	1.4063 ¥/mL	¥ 140.6250	¥ 21.0938	¥ 28.1250
$KMnO_4$	10.0000 ¥/g	¥ 40.0000	¥ 20.0000	¥ 30.0000
H_3PO_4	4.0000 ¥/mL	¥ 0.0000	¥ 16.0000	¥ 0.0000
DIW	0.4167 ¥/mL	¥ 166.6667	¥ 27.0833	¥ 20.8333
H_2O_2	2.4000 ¥/mL	¥ 48.0000	¥ 24.0000	¥ 7.2000
Total		**¥ 404.8917**	**¥ 117.7771**	**¥ 95.7583**

¥ is a unit of Japanese currency (JPY)

Table 3.3 presents the data on GO synthesized using specific techniques, including the dry weight of the resultant GO, the cost of 1 g and the removal capacity of each GO, the processing duration, and the materials cost of each GO per 1 mg of CIP removal. O–GO offers the lowest materials cost per 1 mg of CIP removal, which is just 0.2195 ¥/mg,

compared to S–GO (1.3776 ¥/mg) and F–GO (0.6550 ¥/mg), indicating the use of O–GO for CIP removal from water is more economical. Furthermore, the process optimization implemented in this work also includes time optimization at each stage of the synthesis process, reducing the synthesis time of O–GO. The faster processing time also gives an impression of reducing other expenses, such as power and labor costs, causing this improved approach more favorable for mass production.

Table 3.3. The data of different parameters on the resultant GO

Parameter	**Unit**	**S–GO**	**F–GO**	**O–GO**
Dry weight of resultant GO	g	1.8	1.3	1.5
Material cost per 1 g of GO	¥/g	224.9398	90.5978	63.8389
CIP removal capacity (q_e)	mg/g	163.28	138.32	290.88
Processing duration (approx.)	min	275	120	45
Materials cost per 1 mg of CIP removal	¥/mg	1.3776	0.6550	0.2195

¥ is a unit of Japanese currency (JPY)

3.6. Characterization

FE-SEM observed the surface morphology characteristics of graphite and as-synthesized GO samples, and the corresponding images are shown in Figure 3.12. It is seen in Figure 3.12a that graphite, in its pure form, consists of many smooth-surfaced graphitic carbon sheets with a flaky structure. Whereas Figure 3.12b-d show how the exfoliation and oxidation process ripped off the smooth-surfaced graphite sheet, forming a GO lamellar sheet structure with a significant wrinkled morphology on the graphene basal plane and crumpled at its edges. The sheet-like morphological structures are formed due to oxygenic functional groups attached to the surface [115], [149]. Typically, the monolayer GO sheets have a 0.7–1.2 nm thickness range [108]. There are no significant changes in the morphological characteristics of the GO samples, indicating that all the GO synthesis techniques introduced in this study efficiently turn graphite into GO without any flaws. Although O–GO synthesis consumed less time than synthesizing S–GO and F–GO, this condition did not affect GO morphological quality. On the other hand, using a proper combination of materials and time and a robust mechanical stirring approach increases the quality of the oxidation reaction and exfoliation.

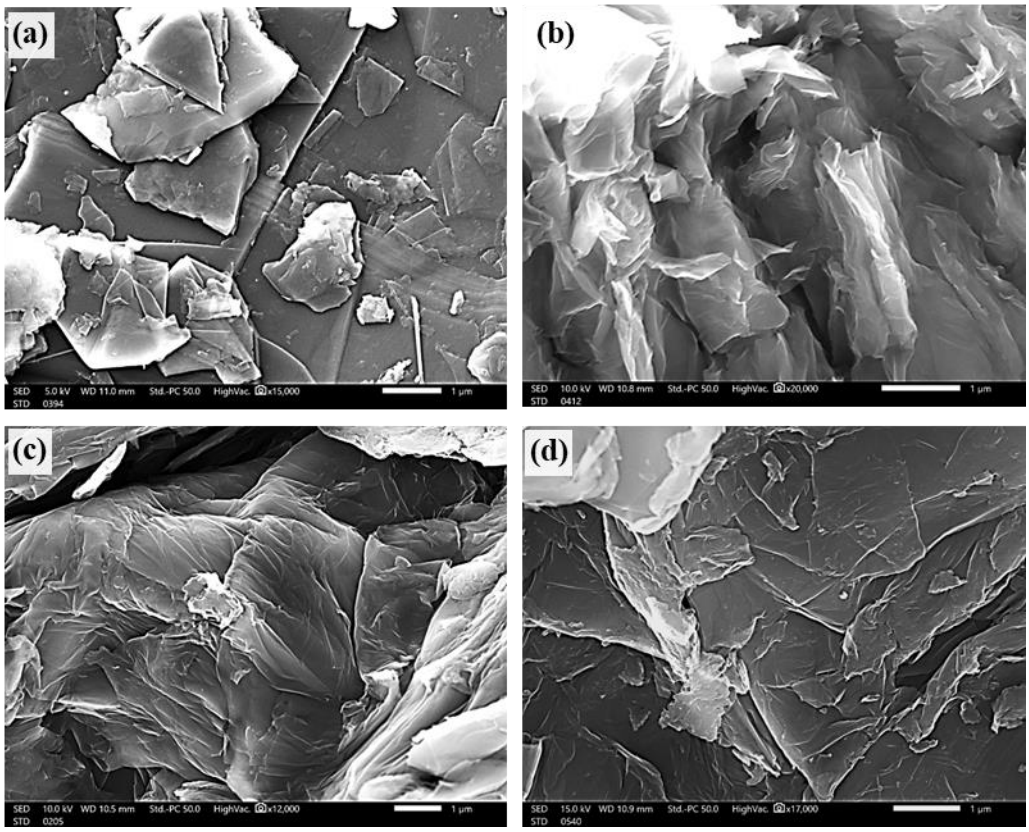

Figure 3.12. SEM images: (a) graphite; (b) S–GO; (c) F–GO; (d) O–GO.

Qualitative findings from morphological observation are also supported by the data from the elemental analysis, which was conducted on the samples using energy-dispersive X-ray spectroscopy (EDS) connected to FE-SEM equipment. According to the elemental data in Table 3.4, O–GO shows the highest oxygen content, 39.15 %, followed by S–GO (35.78 %) and F–GO (32.03%). Oxygen elements presented in GO are due to the formation of oxygenous functional groups in the graphite molecular structure during oxidation [14], [150]. On the other hand, graphite, as the core material of GO, shows no oxygen content and records a carbon content of 100 % because graphite is a non-oxidized material that might not contain or contains a negligible amount of oxygen [151]. This finding confirms that all GO syntheses in this study successfully transform graphite into GO. In addition, the higher oxygen content recorded by O–GO than other samples suggests that the optimized GO synthesis technique is capable of producing GO with high-quality characteristics. Moreover, the lower ratio of carbon content to oxygen (C/O) shown by O–GO is a factor of its high efficiency in adsorbing CIP compared to other samples. This elementary analysis proves that the prolonged synthesis period and the use

of an excessive amount of GO precursor are unnecessary and do not contribute to oxidation efficiency.

Table 3.4. Elemental percentage content and C/O ratio.

Sample	C (%)	O (%)	S (%)	C/O
Graphite	100	-	-	-
S–GO	62.03	35.78	2.19	1.73
F–GO	67.45	32.03	0.52	2.11
O–GO	60.28	39.15	0.57	1.54

Wide-angled XRD analysis was carried out on all GO samples to elucidate their crystal structure and affirm that oxidation has occurred well for GO formation during the syntheses applied in this study. Figure 3.13 shows a pronounced diffraction peak in the XRD patterns of S–GO, F–GO, and O–GO, corresponding to the (001) crystal plane at $2\theta = 9.96^{o}$, 11.8^{o} and 11.54^{o} respectively, confirming the efficacy of the chemical exfoliation and oxidation process in the graphite plane. In addition, all XRD patterns indicate a modest (100) crystal plane of GO peak located at around $2\theta = 42^{o}$, implying that the oxygenic-containing groups were presented to the plane [142]. Ain et al. [152] exploited the same peaks to evaluate oxidation efficacy and discovered nearly the same XRD pattern as O–GO. Moreover, using the Debye-Scherrer equation, the average GO layer thickness of S–GO, F–GO, and O–GO was computed to be 6.85 nm, 5.51 nm, and 8.87 nm, respectively. It was found that the thickness of GO layers varies, with O–GO having a thicker layer than S–GO due to the various water intercalation effect and distinct oxidation impacts on each synthesis may give various oxygen functional group characteristics on the basal plane [116].

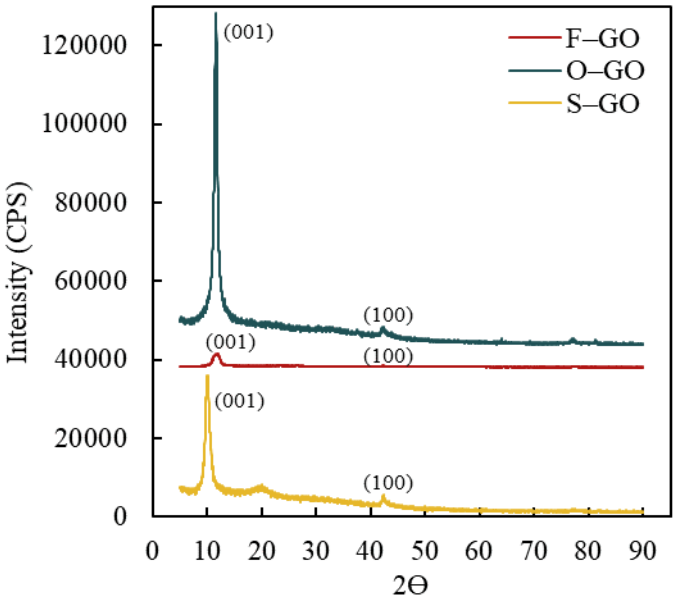

Figure 3.13. XRD patterns of S–GO, F–GO, and O–GO.

3.7. CIP adsorption mechanism

The FTIR spectra characterization can support the adsorption mechanism proposed in the kinetics study and the temperature effect on the CIP removal subtopics. Therefore, FTIR spectra of graphite and O–GO have been gathered in Figure 3.14 to explore the evolution of functional groups and molecular structure transformation on the material's surface after CIP removal activity. By referring to the FTIR spectra of graphite and O–GO, it is found that the chemical exfoliation that occurred during the GO synthesis process transformed the molecular structure by forming several chemical bonds on the GO surface. The new medium absorbance band at 3868 cm^{-1} and broad absorbance bands at 3449 cm^{-1} and 3242 cm^{-1} found in the O–GO's FTIR spectrum correspond to O–H stretching vibration, suggesting the hydroxyl structures were located within graphite interlayers. On the contrary, there is no such functional group in graphite. This kind of oxygenous functional group contributed considerably to the adsorption of CIP. Other than that, the strong absorption peak found at 1615 cm^{-1} represents the ketone group's C=C stretching vibration. Moreover, the strong absorbance bands located at 1760 cm^{-1} and 1040 cm^{-1} correspond to the C=O stretching vibration of the carboxylic compound and the C–O–C stretching vibration associated with the epoxide group, respectively [135]. The FTIR spectra of spent O–GO demonstrating the intensity of the hydroxyl (O–H) and the epoxy (C–O–C) groups are diminishing, and the absorbance bands characteristic change slightly

because the effect of CIP adsorption on the sample surface changes the material's molecular structure [142].

High-density oxygenic functional groups (hydroxyl, carboxyl, and epoxy), resulting from oxidation and functionalization, deposited in the O–GO carbon lattice induced the formation of hydrogen bonds between those functional groups and CIP molecules, thus leading to a more stable and efficacious CIP adsorption potential [103], [153]. The existence of these groups makes the interaction between π-cations and hydrogen, creating an electrostatic attraction mechanism, play a role in complexation on the O–GO surface [142]. In addition, certain bonding provinces at the periphery of O–GO can be engaged in CIP adsorption through π-π interactions between the O–GO's sp2 carbon domains and CIP molecules [11]. Moreover, the advantage of O–GO naturally having a single-layer carbon structure allows all atoms and functional groups to be exposed to the surroundings and easily interact with antibiotic molecules, mainly through π-π interactions between antibiotic molecules and π-electrons of graphene's aromatic ring [113], [154].

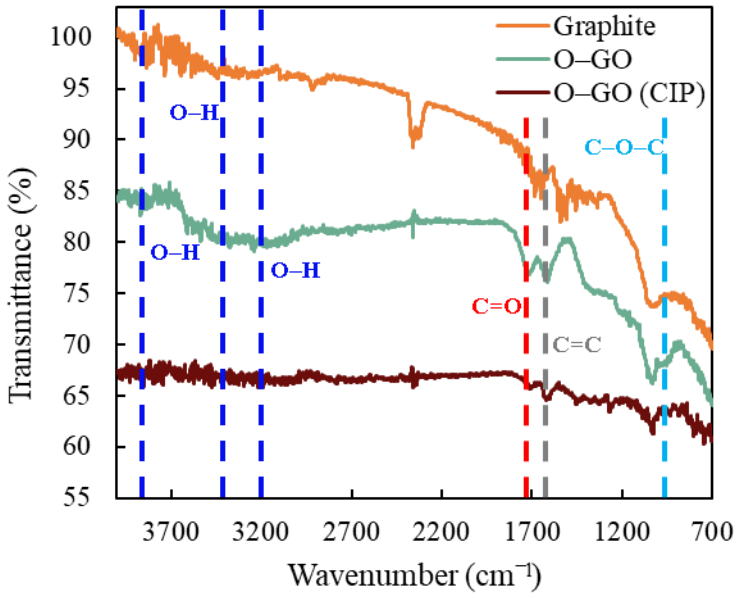

Figure 3.14. FTIR spectra of graphite and O–GO before and after CIP removal.

This page is intentionally left blank.

Chapter 4

Chloramphenicol Removal from Water by Various Precursors to Enhance Graphene Oxide – Iron Nanocomposites

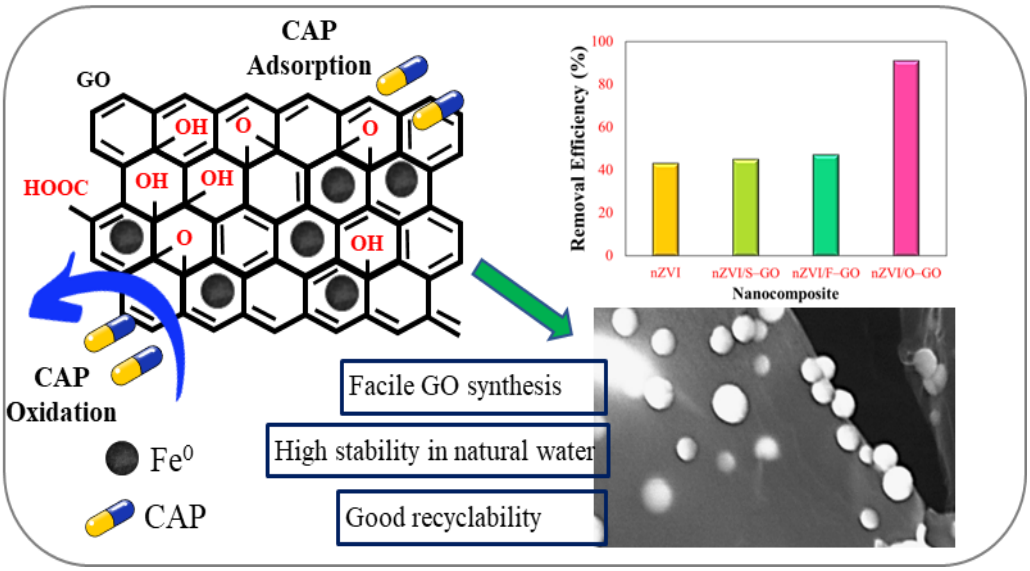

4.1. Characterization

Scanning electron microscopy described the surface morphologies of the nZVI, GO, and nZVI/GO composite materials. The bare nZVI structure, as seen in Figure 4.1a, consists of irregularly formed spherical formations with diameters ranging from 60 to 70 nm. Due to the combination of magnetic and electrostatic interactions among the nanoparticles, these condensed nZVI nanoparticles form an agglomeration with a chain-like structure [49], [90], [128]. On the other hand, the SEM micrographs of as-synthesized S–GO, F–GO, and O–GO are shown in Figure 4.1b–d, revealing a unique lamellar sheet-like morphology with a wrinkled structure on the surface. This morphological result demonstrated that the morphology behavior of the GO samples remained relatively constant despite being manufactured in various ways and using varying amounts of chemicals.

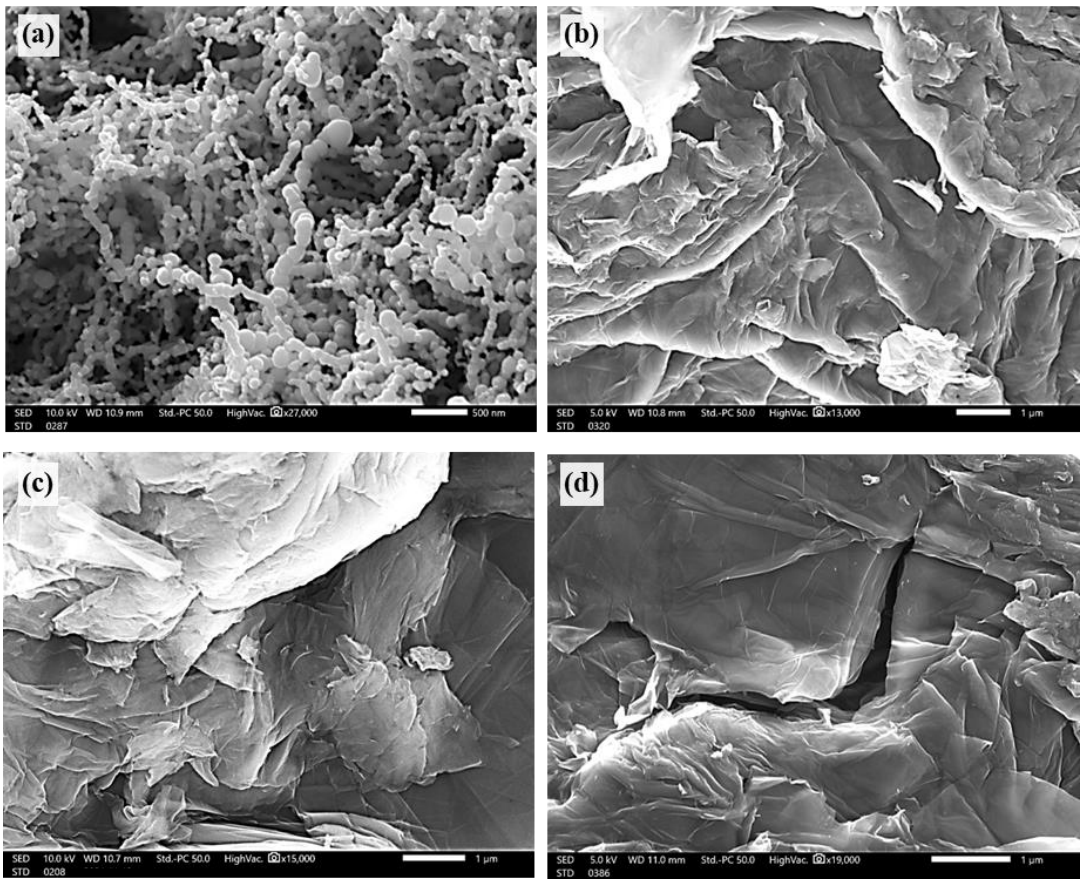

Figure 4.1. SEM images of as-synthesized nanomaterials: (a) nZVI, (b) S–GO, (c) F–GO, (d) O–GO**.**

Moreover, the morphological surface structure of nZVI/GO was affected by the employment of several GO precursors in its synthesis. This factor may be clarified by probing the surface morphology of the nZVI/GO nanocomposite structure produced with various GO precursors. As described, each GO precursor was synthesized using different methods and catalysts. Figure 4.2a-c shows the SEM image of nZVI/GO nanocomposites constructed using S-GO, F-GO, and O-GO as GO components, with the weight ratio of nZVI to GO being 1:1. When S-GO was employed as a precursor, nZVI/GO showed a slight difference in morphology compared to the nZVI/O-GO morphology image. nZVI particles adhere and spread unevenly over the S-GO surface with a mild nZVI agglomeration. Nevertheless, the nZVI/F-GO SEM image demonstrates that when the F-GO precursor was utilized as an nZVI precipitation medium, the nZVI nanoparticles seemed agglomerated and scattered in spotted bunches over the GO surface, exhibiting a coralline look-like morphology. This behavior was brought on by the functionalized F–GO surface utilizing H_3PO_4 to produce many OCFGs, which contributed to the surface's high negative charge density and hydrophilicity and caused nZVI to assemble on the surface of GO fast [115].

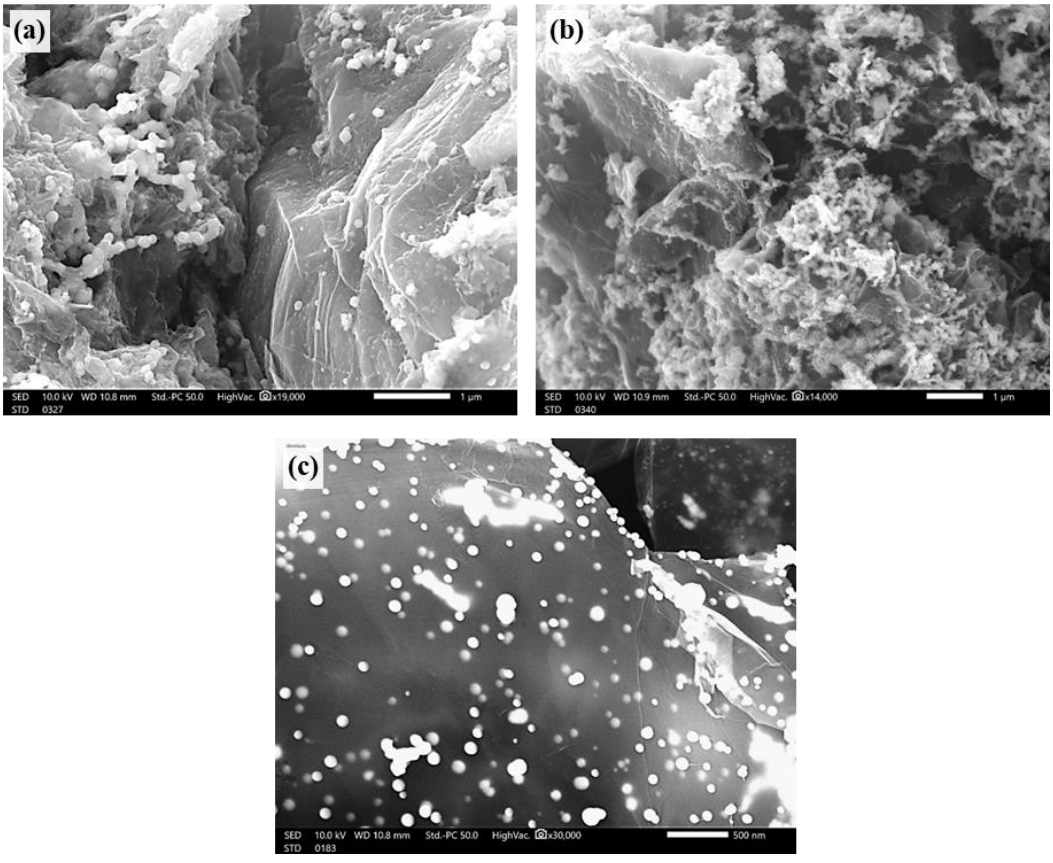

Figure 4.2. SEM images of nZVI/GO nanocomposite by different GO precursors: (a) nZVI/ S–GO-1:1, (b) nZVI/ F–GO-1:1, and (c) nZVI/ O–GO-1:1.

Figure 4.3 display the surface morphology of nZVI/O–GO for various mass ratios. The nZVI particles spread and precipitate evenly on the GO surface without substantial particle aggregation, as shown in the nZVI/O-GO-1:1 morphology in Figure 4.3a. Figure 4.3b indicates the morphological image of nZVI/O-GO-1:2, which depicts a virtually identical view as nZVI/O-GO-1:1 but with the nZVI particles scattered more loosely throughout the GO surface. On the other hand, when the mass ratio of nZVI to GO rises, the density of nZVI particles precipitated on the surface of GO looks likely to grow, and nZVI particle aggregation on the GO surface starts to develop (Figure 4.3c). As illustrated in Figure 4.3d, the nZVI nanoparticles predominated the composite and coated the surface of GO more extensively when their mass was raised by tenfold the amount of GO. This phenomenon caused more enunciated nZVI chains to be visible as an aggregation.

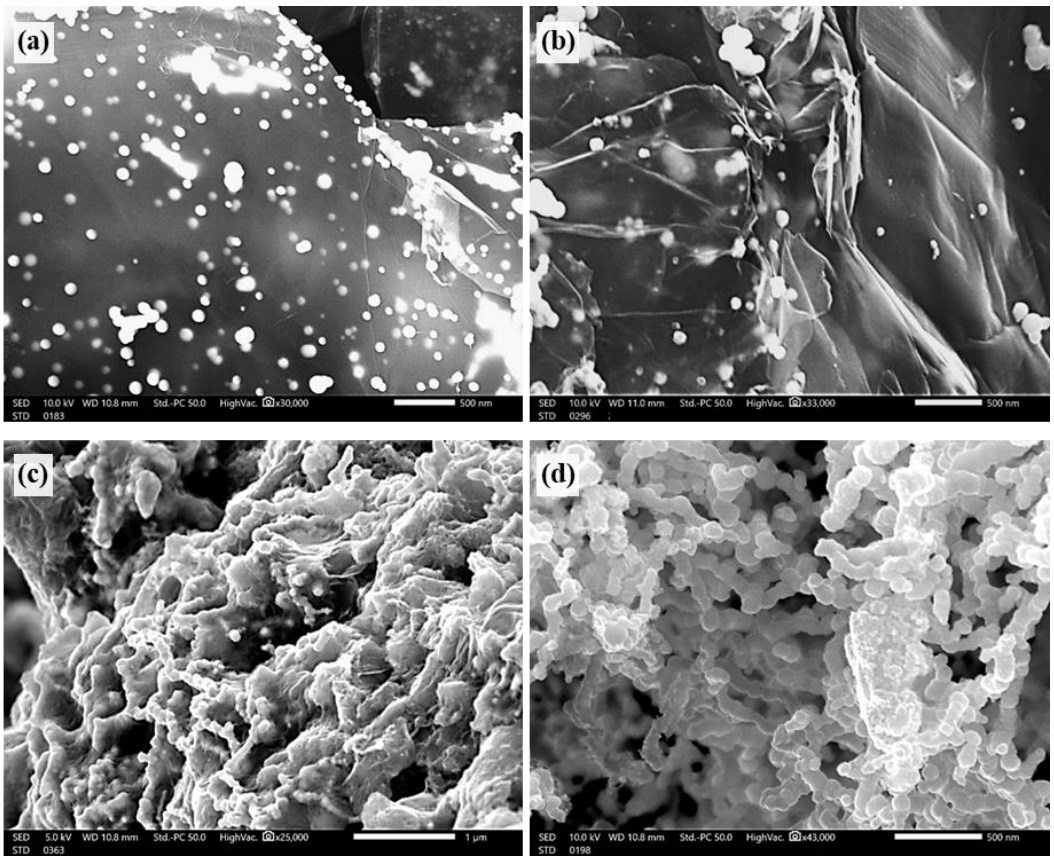

Figure 4.3. SEM images of as-synthesized nanocomposite at different mass ratios: (a) nZVI/O–GO-1:1, (b) nZVI/O–GO-1:2, (c) nZVI/O–GO-2:1, and (d) nZVI/O–GO-10:1.

These findings assist in comprehending the influence of the nanocomposite mass ratio and the GO precursor on the surface morphological behavior of the nZVI/GO

nanocomposite. These results support the idea that the surface of the synthesized GO is affected by the GO synthesis process, which alters the nZVI deposition characteristic. Additionally, a more extraordinary active surface site for the removal interaction between the nZVI/GO and CAP was made possible by the composite mass ratio, which was crucial in ensuring that nZVI particles were effectively disseminated and precipitated on the GO surface without aggregation.

To determine the nanocomposite crystal structure and evaluate the efficiency of the GO synthesis process presented in this paper, a wide-angle (3 – 90º) XRD examination was carried out. At 2θ = 11.24º in the O–GO XRD pattern (Figure 4.4), a prominent peak corresponding to the standard (001) crystal plane of GO is seen, demonstrating the efficacy of this sophisticated synthesis process in oxidizing graphite to create GO. The same peak was used by Ain et al. [152] to assess the effectiveness of GO synthesis in their research. The XRD pattern shown by O–GO matches the XRD pattern of GO that Ahmad et al. [155] reported.

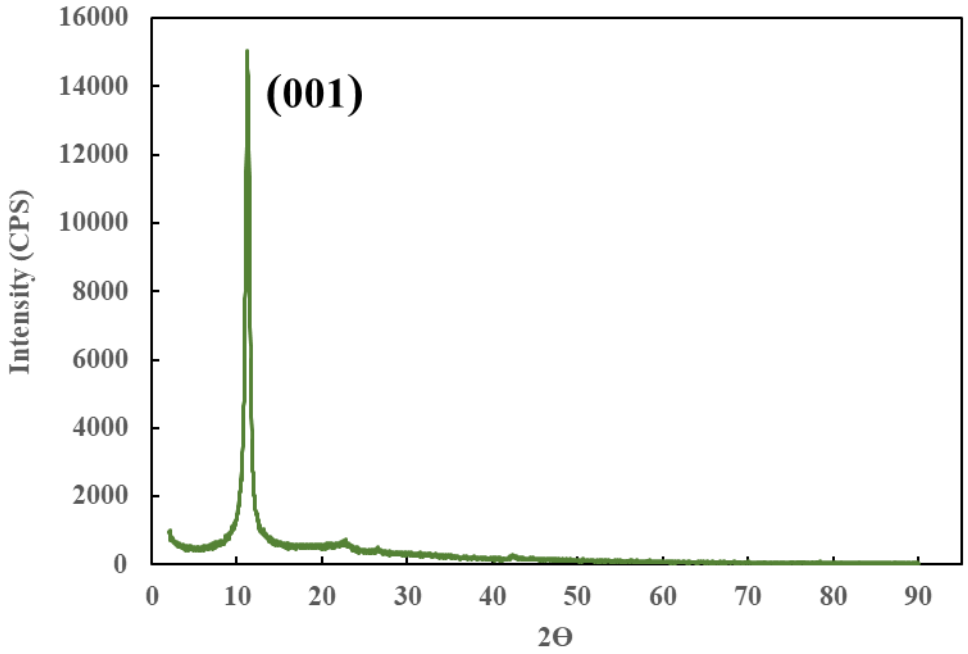

Figure 4.4. XRD pattern of O–GO

The XRD patterns of bare nZVI and nZVI/O–GO at different mass ratios are shown in Figure 4.5. On the XRD pattern of bare nZVI, a strong peak at 2θ = 44.78° was ascribed to the (110) crystal plane, while soft peaks at 2θ = 63.1° and 2θ = 81.98° were allocated

to the (200) and (211) Fe^0 crystal planes, respectively. The appearance of the identical significant peak on the XRD pattern of nZVI/O–GO samples between 2θ of 44.5° to 45.5° revealed that the nZVI particles were generated and precipitated on the O–GO sheets effectively. Due to the more significant concentration of nZVI particles relative to GO, the nZVI particles induced the GO surface to be entirely covered by nZVI particles, which is why the Fe^0 peaks are still clearly visible in the XRD pattern of the nZVI/O–GO-10:1. The lack of a graphitic (G) carbon peak with a crystal plane (002) in the sample's XRD spectrum is explained using a similar argument.

However, when the mass of nZVI declined, the strength of typical nZVI peaks reduced, and at 2θ = 25.5°, graphitic (G) carbon peaks could be detected in the XRD patterns of nZVI/O–GO-2:1, nZVI/O–GO-1:1, and nZVI/O–GO-1:2. The removal of GO peaks and the appearance of graphitic (G) carbon peaks demonstrated that GO had been stripped off entirely, demonstrating the effectiveness of using O–GO precursors to create nZVI/O–GO nanocomposites. The (311) diffraction plane of iron oxide (Fe_3O_4) corresponds to the peak on the XRD pattern of nZVI and nZVI/O–GO at 2θ = 35.5° ± 0.5. Due to nZVI's exceptionally high reactivity, which enabled it to quickly oxidize to produce Fe_3O_4 when in contact with water and oxygen, this peak was present. The peak intensity did, however, decrease as the mass ratio of GO rose, suggesting that the presence of GO as a supporter of nZVI might reduce the corrosion of nZVI and so positively affect nZVI's catalytic activity.

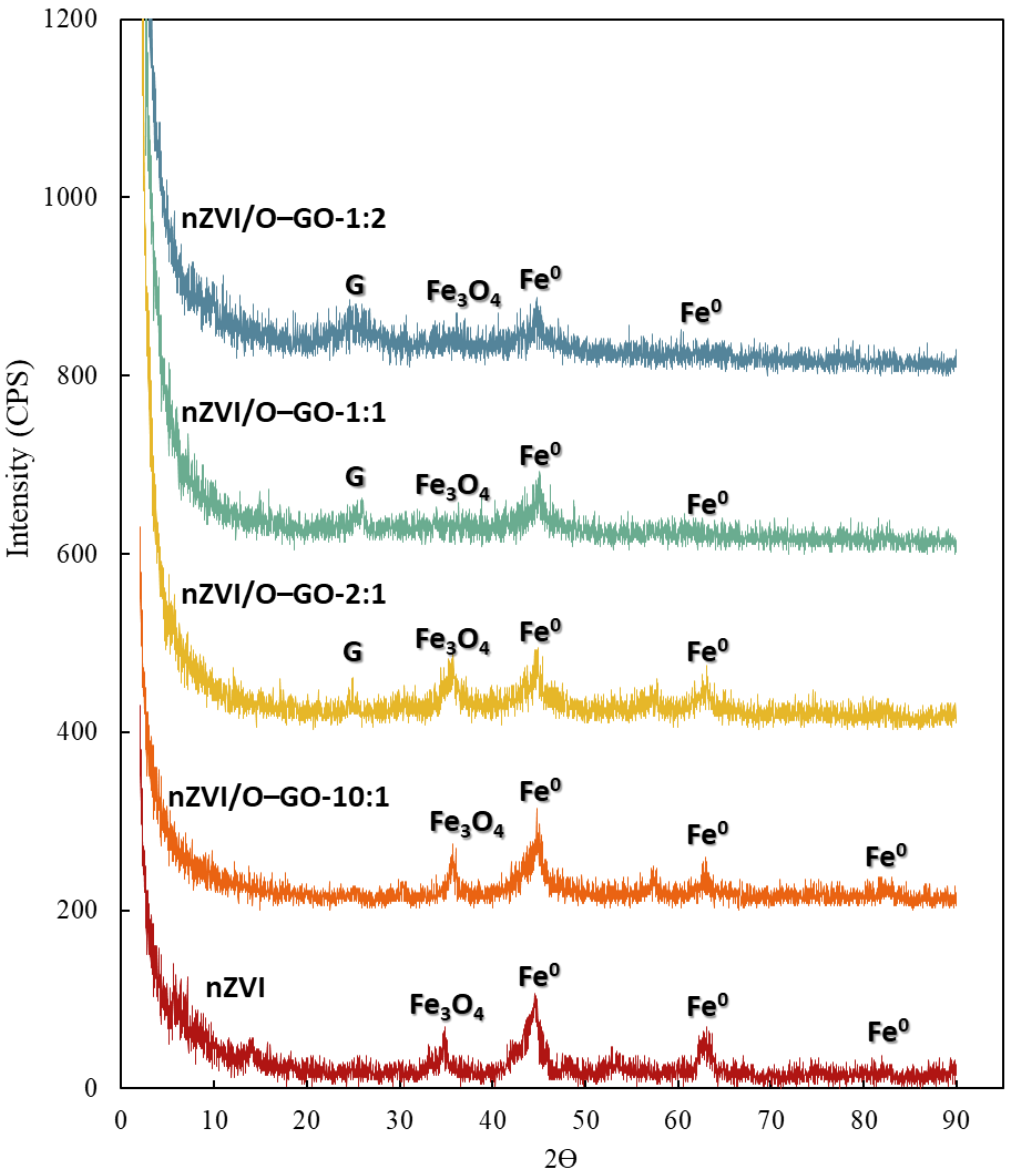

Figure 4.5. XRD patterns of bare nZVI and nZVI/O–GO at various mass ratios.

4.2. Effect of GO precursors on CAP removal behavior

The investigation results into the removal behavior of CAP by nZVI/GO synthesized with different GO precursors are shown in Figure 4.6 as a function of time. The graph illustrates how, in general, GO precursors played a critical function and had a considerable influence on the effectiveness of nZVI/GO in eliminating CAP. It was discovered that employing F-GO as a GO precursor for nZVI/GO produced a greater clearance rate of CAP throughout the first 30 minutes of the reaction than S-GO. At three-hour periods, the elimination efficiency of the S-GO and F-GO precursors peaked at around 45% and 47%, respectively. The significant improvement was attributed to using

O-GO as a precursor in the synthesis of nZVI/GO nanocomposite, which resulted in CAP removal efficiencies of 88% within 30 minutes of reaction and 90% at periods of 3 hours.

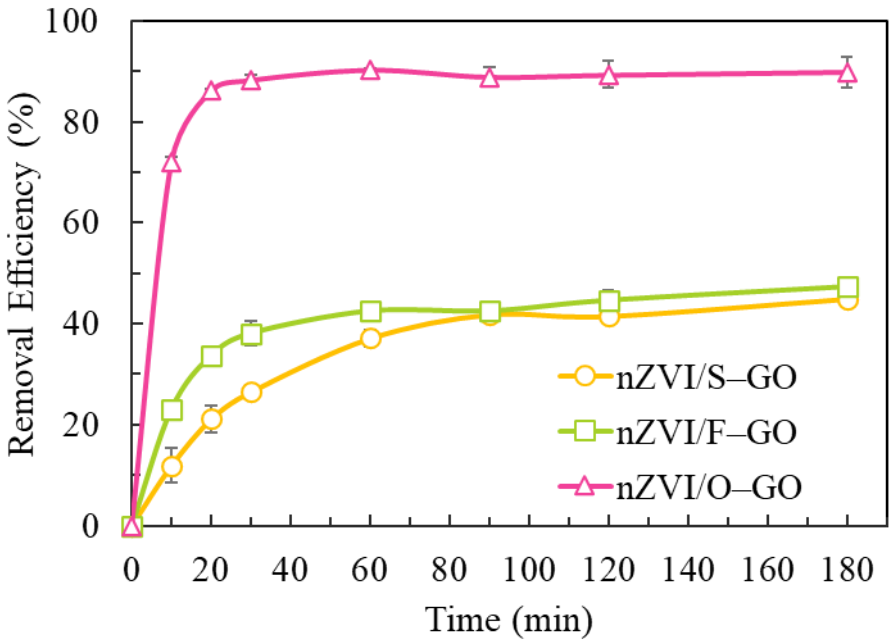

Figure 4.6. The CAP removal efficiency (%) of nZVI/GO using different GO precursor component

These findings support the concept that the CAP removal behavior of nZVI/GO nanocomposite is affected differentially by using various GO precursors. According to the results, additional intercalation catalytic agents generate nZVI/GO nanocomposite with various impacts on the CAP removal behavior when synthesizing the GO. Since the rate and efficiency of CAP removal only slightly increased, using H_3PO_4 as an oxidizing catalyst had no discernible benefit. The first CAP removal by nZVI/F-GO showed a fast rise in removal rate, indicating that H_3PO_4 had a different intercalation impact and affected the reactivity of the GO surface. The GO surface functionalized by H_3PO_4 produces diverse OCFGs, according to Cao et al. [115], which may impact the material's attraction and driving forces. According to this study, the primary thread elimination and time reduction in the GO precursor synthesis did not diminish the material's reactivity. The outstanding removal performance of the nZVI/O-GO composites proved this effect.

Although O-GO was produced without a supplemental oxidation catalyst, the removal impact of nZVI/O-GO was rather significant when compared to nanocomposites

containing GO precursors prepared using a catalytic agent. Finding the optimal ratio of material quantity and main thread duration is the key to producing effective GO precursors without catalysts. Using non-optimal materials results in waste and poor reactivity due to the overabundance of unoxidized graphite after the synthesis process is completed. The exfoliation time is crucial for GO production, not the oxidation period, according to Arabpour et al. [122]. Thus, the O-GO synthesis process combined an appropriate thread period with oxidation-related elements, a high-temperature atmosphere, and high exfoliation intensity by vigorous mechanical stirring, contributing to the structural deformation of the graphite sheet and effective graphite peeling into the GO layers. The outcome is a heterogeneous structure with high-intensity oxidation on both the edge and inside portions, resulting in material reactivity.

O-GO was selected as the most promising GO precursor for producing nZVI/GO nanocomposites from the CAP removal performance and economic perspectives since its synthesis needed no extra catalytic agents, was more time-saving, and even delivered an outstanding CAP removal impact. These aspects made nZVI/O-GO the preferred nanocomposite for further investigation in subsequent studies.

4.3. Effect of mass ratio on CAP removal behavior

The effectiveness of nZVI, O-GO, and nZVI/O-GO in removing CAP was examined in the batch experiments to determine the best beneficial mass ratios of nZVI and O-GO. The CAP removal efficiency of bare nZVI, O-GO, and nZVI/O-GO with various mass ratios is illustrated in Figure 4.7. At the end of the reaction, bare nZVI demonstrated CAP removal performance of up to 45%, whereas O-GO only eliminated CAP by 2%, or its removal impact might be insignificant. Interestingly, the CAP removal has substantially improved with the deposition of nZVI on O-GO. The results indicated that at the beginning of the 20 minutes, CAP was promptly removed from all nZVI and nZVI/GO samples. Then, its removal efficiency plateaued until 3 h, which explains why the CAP removal process remained steady during the reaction and saw nearly no desorption. When the nZVI mass was reduced or the GO mass was raised, the nanocomposite removal performance steadily improved; nZVI/O-GO-1:2 had the maximum removal efficiency of 93%. The nZVI/O-GO-2:1 (87%) and nZVI/O-GO-1:1 (90%) CAP removal efficiencies can be regarded as relatively high and did not significantly differ from the

nZVI/O-GO-1:2 performance, demonstrating that further lowering the mass ratio of nZVI or further raising the mass of GO after these points did not contribute a substantial impact on the CAP removing performance.

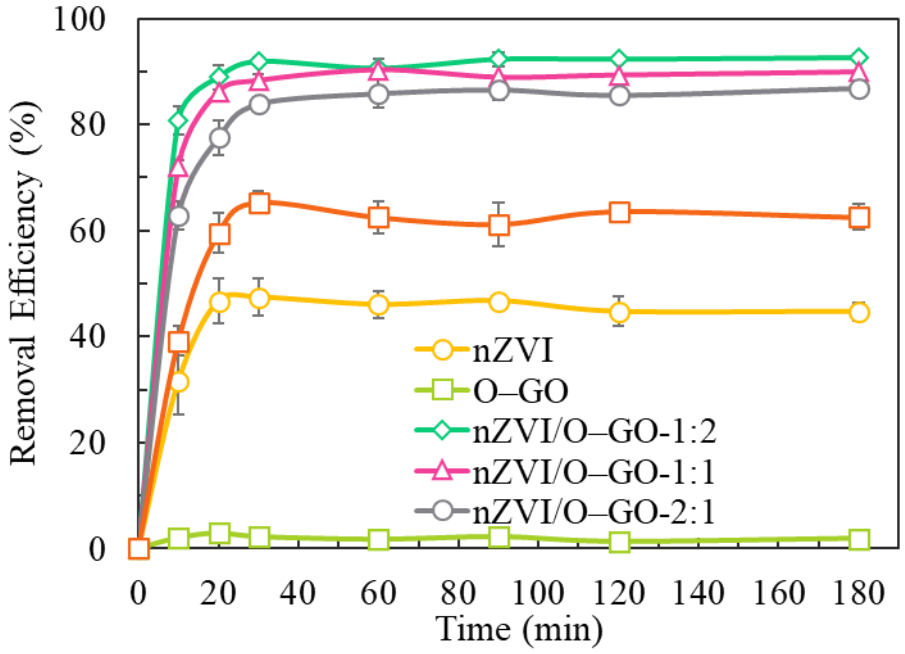

Figure 4.7. The CAP removal efficiency (%) of nZVI/O–GO at different nZVI:GO mass ratio

The existence of ROS generated by a reaction between dissolved nZVI and O_2 could remove CAP, which explains why nZVI's CAP removal efficiency is significantly superior to that of O–GO [156]. More nZVI reactive sites are now accessible due to the separation and precipitation of nZVI on the GO surface, enhancing the contact between the particle and CAP for the removal reaction shown by the nZVI/O-GO. The nanocomposites (nZVI/O-GO-1:1 and nZVI/O-GO-1:2) showed a minor improvement in CAP removal efficiency, but this was due to the decreased capacity of the nZVI, which made CAP removal less effective. It is interesting to note that reducing the mass ratio of nZVI in nanocomposites did not affect the material's performance since the larger mass ratio of O-GO provided its advantages to balance out the nZVI's decreasing influence, enabling the CAP removal efficiency to be increased even further. O-GO possesses a lot of surface area, which prevents nZVI agglomeration, and its oxygenous functional groups provide GO additional reactive regions, both of which enable nZVI to eliminate CAP [157]. In addition, due to their increased electrical conductivity [157] and unique

characteristics for trapping electrons produced by the Fenton reaction [158], crumpled GO sheets provide more ROS for CAP removal.

According to these results, O-GO and nZVI impact the efficiency of CAP removal. Choosing the proper mass ratio of nZVI and O-GO is crucial for outstanding nanocomposite performance in CAP removal by considering the best cost-efficiency and processibility. A nanocomposite with a mass ratio M_{nZVI}: M_{GO} of 1:1 (nZVI/O-GO-1:1) was chosen as the most suitable material for CAP removal and subsequent studies in light of the criteria mentioned. Despite having an excellent CAP removal efficiency, nZVI/O-GO-1:2 was not preferred or valuable due to its lengthy synthesis procedure. Furthermore, the difference between nZVI/O-GO-1:1 (90%) and nZVI/O-GO-1:2 (93%) was marginal and inconsequential.

4.4. Effect of nZVI/O–GO dosage on CAP removal behavior

Through the Fenton system, the nZVI/O-GO dosage might perform an essential function in CAP elimination [157]. The optimal dosage of nanocomposites lowers the cost of treatment and makes it easier to regulate nanoparticles throughout the post-water treatment process [49]. As a result, several batch studies were conducted to determine the optimum nZVI/O-GO dosage for removing CAP from water. The results of these experiments are presented in Figure 4.8. The results demonstrated a considerable improvement in CAP removal effectiveness from 7% to 90% by increasing the nZVI/O-GO dosage from 0.01 to 0.25 g/L. Increased nZVI/O-GO active sites may be contributing to this rise in CAP removal. In addition, increasing the amount of nZVI will increase the ROS that destroys the CAP [61, [62]. The nZVI/O-GO performance did, however, show a modest and negligible improvement when the dosage was progressively raised to 0.5 g/L and 0.75 g/L, with CAP removal efficiencies at 93% and 94%, respectively. In reality, this high-dosage addition of nZVI/O-GO over twice has yet to produce a result commensurate with CAP removal and is not cost-effective. In light of these factors, 0.25 g/L is the dose at which nZVI/O-GO will perform at its peak level.

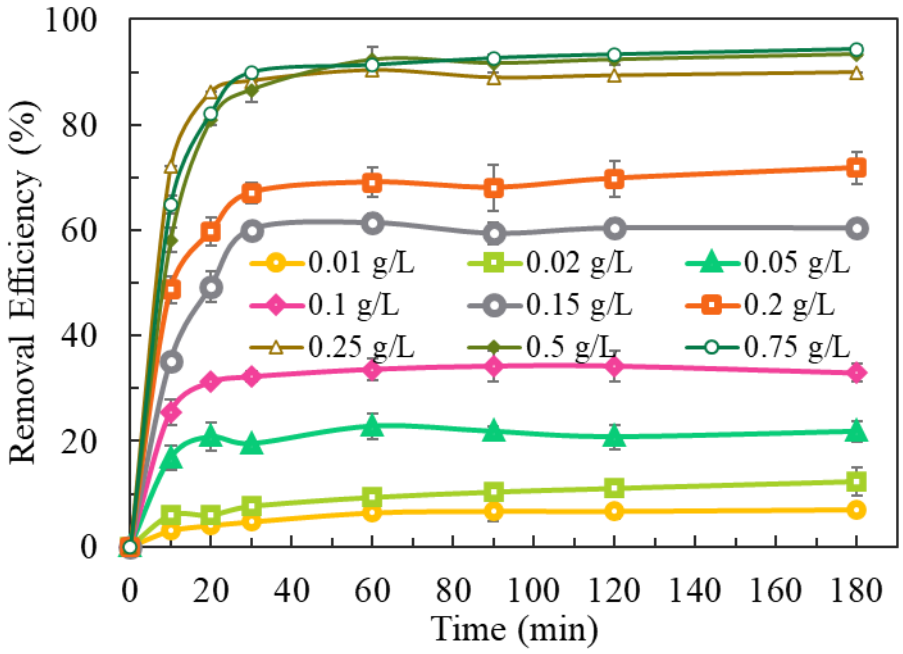

Figure 4.8. The CAP removal efficiency (%) of nZVI/O–GO-1:1 at different dosages

4.5. Effect of initial pH on CAP removal behavior

The CAP solution's initial pH (pH_0) is one of the environmental elements that might impact free radical production and, therefore, affect CAP removal behavior. Batch studies were done to investigate how pH_0 affected the removal of CAP since it is one of the essential factors in determining how well the nanocomposite can remove CAP. The impact of pH_0 on the elimination of CAP by nZVI/O-GO and bare nZVI from pH_0 3.0 to 11.0 after 3 hours of reaction is shown in Figure 4.9. It is evident that the pH_0 of the solution, especially under acidic circumstances, had an impact on CAP removal. Both materials showed a substantial reduction in CAP removal effectiveness at pH_0 3.0 compared to their performance in CAP natural pH_0 solution (pH_0 = 6.2), where nZVI/O-GO reported the lowest CAP removal efficiency of 50%. At the same time, bare nZVI demonstrated essentially no removal. Nevertheless, at greater pH_0 levels, CAP removal efficiency was improved. At pH_0 5.0, nZVI/O-GO and bare nZVI demonstrated the best CAP removal ability, with 91% and 60% removal rates. Intriguingly, the nZVI/O-GO's performance in removing CAP at pH 6.2 showed a negligible difference from the highest removal efficiency of 91% at pH 5.0. The performance of nZVI/O-GO for CAP removal was unaffected by the rise in pH_0 from 6.2 to 11. Conversely, bare nZVI in this pH_0 range exhibited a significant decrease in CAP removal efficiency compared to those in pH_0 5.0.

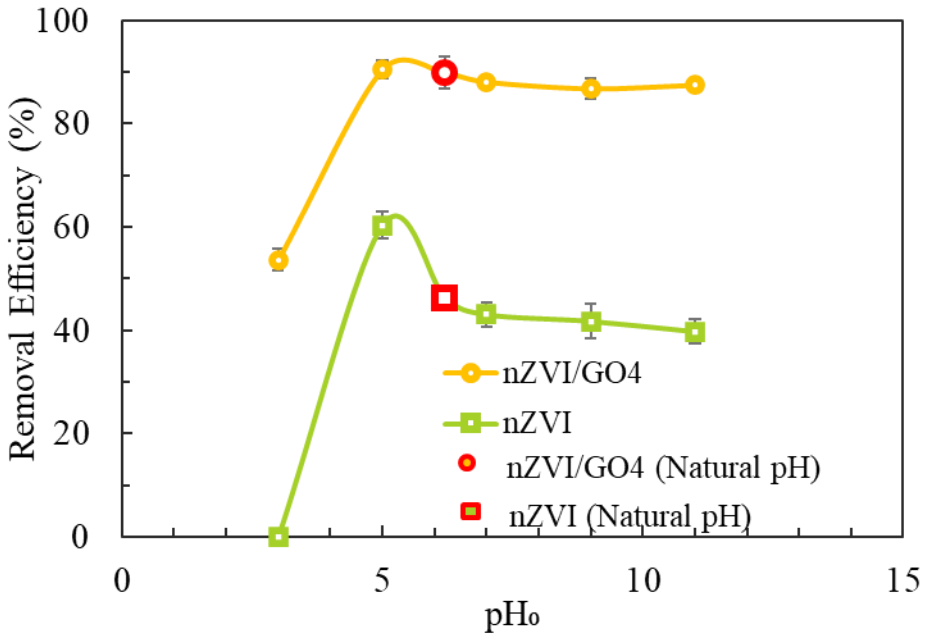

Figure 4.9. The CAP removal efficiency (%) of nZVI and nZVI/O–GO-1:1 at different pH

Changes in pH_0 may affect the reductive abilities of nZVI. Strong acid media causes surface blemishes and the destruction of nZVI particles, forming a salt aqueous. On the other hand, the contact of nZVI with an alkalic aqueous solution leads to severe surface passivation because the thickness of the oxide layer increases. These circumstances impact nZVI's reductive characteristics and prevent electron transfer for CAP removal [156]. Given that essentially minimal removal was shown by bare nZVI in a very acidic aqueous solution (pH_0 = 3), this finding explains why nZVI/O-GO could not enhance CAP removal more favorably. It is interesting to note that the presence of GO in the nanocomposite was able to protect nZVI from the adverse effects brought on by the highly acidic and alkalic conditions due to the unique characteristics of the GO sheets' surface, which having interlayers and was clumped at the edge, providing a protective medium for nZVI particles, preventing a direct reaction with the solution. Thus, even in the CAP solution with pH_0 3.0, nZVI/O-GO could still enhance superior CAP removal than bare nZVI. The efficiency of CAP removal was increased by more aggressively converting nZVI to Fe^{2+} in a low acidic environment (pH_0 = 5). This process prompted additional removal mechanisms, including adsorption and oxidation. Specifically, in high-pH conditions, CAPs with hydroxyl groups generally have a low ionization potential and are readily oxidized [159]. Furthermore, the elimination stability of CAP was aided by the

presence of free radicals brought on by the Fenton reaction's tendency to occur in alkaline circumstances. According to Song et al. [96], alkaline conditions facilitate the production of H_2O_2 for the Fenton reaction.

In particular, for industrial wastewater treatment with variable pH values, nZVI/O-GO is more appropriate than bare nZVI because it provides more extraordinary consistent CAP removal ability in acidic and alkalic environments. nZVI/O-GO was able to eliminate CAP even when employed in very acidic conditions. nZVI/O-GO is more advantageous and perspective than bare nZVI, whose applicability was in a limited pH range, and even the CAP removal efficiency was much lower than that showed by nZVI/O-GO, due to the stability of CAP removal in an environment with a more extended pH range.

4.6. Effect of CAP initial concentration on CAP removal and kinetic analysis

Figure 4.10 shows the impact of CAP initial concentration (varying from 50 to 200 mg/L) at pH_0 5.0 with a dosage of 0.25 g/L nZVI/O-GO. As the initial concentration rose, the removal of CAP was reduced. After 30 minutes of contact time, nZVI/O-GO efficiently removed over 91 % of CAP at initial concentrations of 50 mg/L and 70 mg/L, and almost all CAPs had been effectively removed after 3 h. The CAP removal efficiency slightly decreased to 91% at the 100 mg/L initial concentration. When the initial concentrations of CAP were raised to 150 mg/L and 200 mg/L, respectively, the efficiency of CAP removal continued to decline modestly to 77% and 72%. This removal pattern suggests that the removal performance had an opposite relationship to the initial concentration of CAP, which is consistent with previous studies [84], [141], [145]. The lowered reduction reaction caused by the decreased particles' active site reduced CAP removal efficiency, particularly at high initial concentration solutions [84], [158]. Despite the decrease in CAP removal efficiency, removal rates at high initial concentrations (150 mg/L and 200 mg/L) using this nanocomposite can still be considered high when compared to previous research findings by introducing the catalyst for the removal reaction [160], three-dimensional nanocomposite development approach [156], and other iron-based reinforced composites [161]. This study successfully created a graphene-based nanocomposite capable of efficiently eliminating high-concentration CAP without needing extra degradation catalysts.

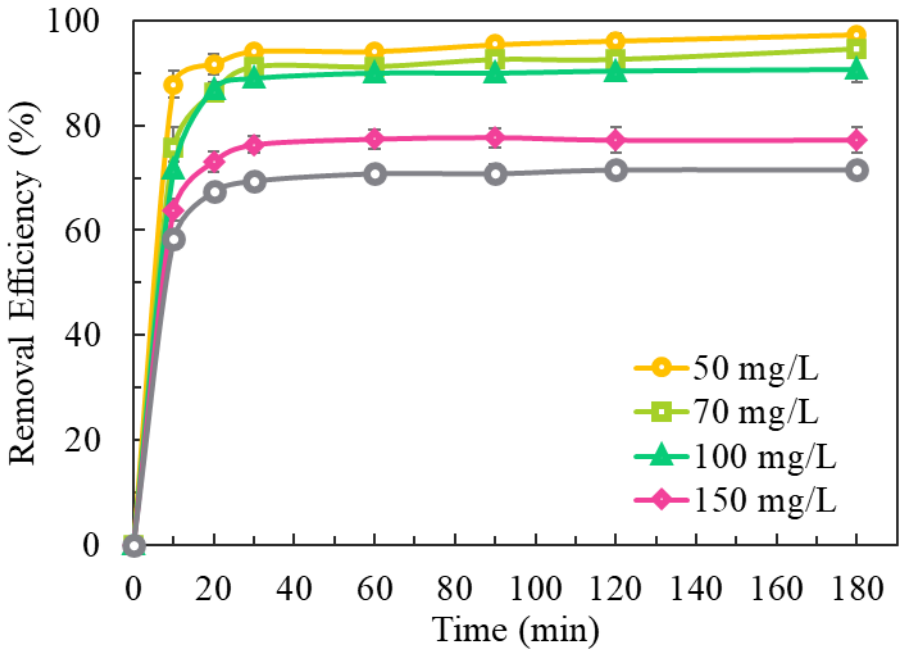

Figure 4.10. The CAP removal efficiency (%) of nZVI/O–GO-1:1 at different initial concentration

Numerous reaction kinetic models have been used to explain CAP removal kinetics data. The outcomes of the kinetics data corresponding with the pseudo-first-order (PFO), pseudo-second-order (PSO), intraparticle diffusion, and Elovich models are shown in Figure 4.11. The CAP removal pattern was precisely matched to the PFO, PSO, and Elovich models but not to the intraparticle diffusion model. The model's regression correlation coefficient (R^2) may also be used to objectively evaluate the model's fit's accuracy. The accuracy of each model employed has also been evaluated statistically using the Akaike information criterion (AIC) model, which aids in deciding the most suitable model. The kinetics parameters, regression correlation coefficients (R^2), and AIC for each model are shown in Table 4.1. The PSO model was more consistent with the data from experiments of CAP removal at low concentrations (50 mg/L and 70 mg/L), as demonstrated by the models' lowest AIC and maximum regression coefficient (R^2) values. In contrast, the PFO model could represent CAPs at high concentrations (100 mg/L, 150 mg/L, and 200 mg/L). The experimental data's consistency with the PFO and PSO models revealed potential elimination procedures involving physisorption and chemisorption, respectively [14], [49].

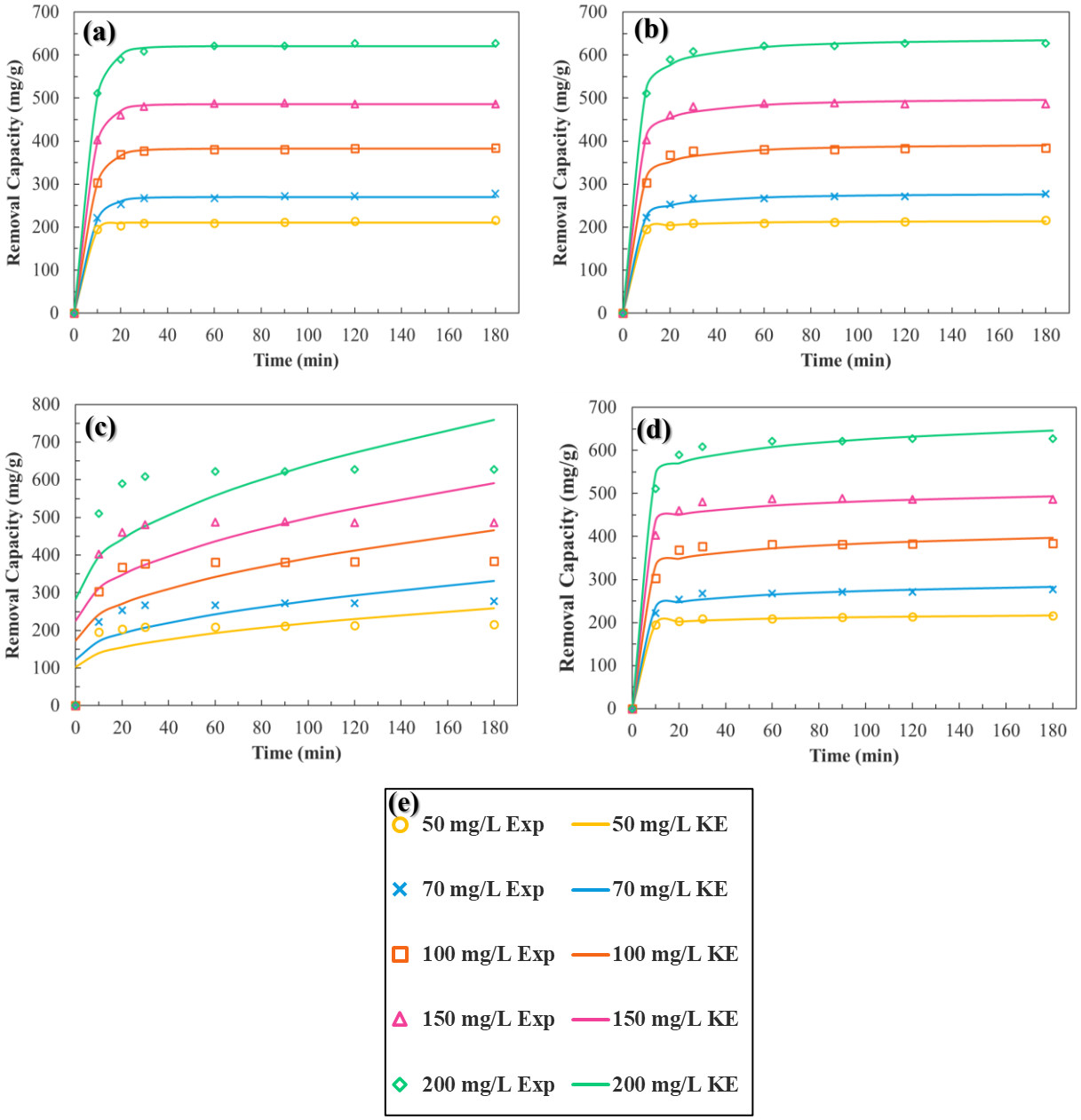

Figure 4.11. Kinetics data fittingness on kinetics model: (a) Pseudo-first-order (PFO); (b) Pseudo-second-order (PSO); (c) Intraparticle diffusion; (d) Elovich models; (e) lagend

Table 4.1. Kinetics analysis data for CAP elimination by 0.25g/L nZVI/O–GO-1:1 by different models

CAP initial concentration ($mg \cdot L^{-1}$)	Pseudo-first-order				Pseudo-second-order				Intraparticle diffusion					Elovich				
	$q_{e,cal}$ ($mg \cdot g^{-1}$)	K_1 (min^{-1})	R^2	AIC_c value	$q_{e,cal}$ ($mg \cdot g^{-1}$)	K_2 ($g \cdot mg^{-1} \cdot min^{-1}$)	R^2	AIC_c value	$q_{e,cal}$ ($mg \cdot g^{-1}$)	C_{intra} ($mg \cdot g^{-1}$)	K_{intra} ($mg \cdot g^{-1} \cdot min^{1/2}$)	R^2	AIC_c value	$q_{e,cal}$ ($mg \cdot g^{-1}$)	α ($mg \cdot g^{-1} \cdot min^{-1}$)	β ($mg \cdot g^{-1}$)	R^2	AIC_c value
50	210.93	0.25	0.9979	29.2	215.21	0.0044	0.9996	15.2	258.18	103.28	11.55	0.4730	73.5	216.80	7.71E+12	0.15	0.9993	20.7
70	270.53	0.17	0.9980	32.8	280.59	0.0015	0.9983	31.3	331.73	121.82	15.65	0.5360	76.3	282.47	3.49E+06	0.06	0.9923	43.5
100	382.20	0.16	0.9999	15.9	395.94	0.0010	0.9945	46.3	465.34	173.30	21.77	0.5199	82.1	396.90	7.55E+06	0.05	0.9842	54.8
150	485.50	0.17	0.9994	32.7	501.37	0.0009	0.9977	43.4	591.63	224.76	27.34	0.5082	86.1	494.00	9.40E+09	0.05	0.9894	55.6
200	620.97	0.17	0.9992	38.6	642.75	0.0007	0.9983	45.0	759.00	283.56	35.44	0.5219	89.8	645.97	2.46E+07	0.03	0.9913	57.8

4.7. Effect of solution temperature on CAP removal and thermodynamic analysis

The impact of solution temperatures (25 ºC, 35 ºC, 45 ºC, and 55 ºC) on nZVI/O-GO's behavior in removing CAP is demonstrated in Figure 4.12. The removal efficiencies at such temperatures during the 3 h period were 91–92%. These results indicate that the CAP removal behavior was not considerably affected by raising the solution temperature, evidenced by the negligible and insignificant shifts in removal efficiencies at the end of the experiment. This trend is consistent with the findings of Nguyen et al. [158] for oxytetracycline (pharmaceutical contaminant) removal by reduced graphene oxide-supported bimetallic Pd/nZVI nanocomposites, wherein the removal efficiencies at different solution temperatures reached a similar value after 2 h of reaction. However, at the beginning of the 30 min., variations in CAP removal behavior are noticeable. The pace of CAP removal has increased as temperatures have risen. According to previous studies [141], [158], the elimination of oxytetracycline and CAP showed the same tendency. The temperature increases in the first 30 minutes sped up the iron's corrosion response and increased the free radicals required to remove CAP [158]. As a result, the rate of CAP removal is strongly correlated with the solution temperature, especially early in the reaction.

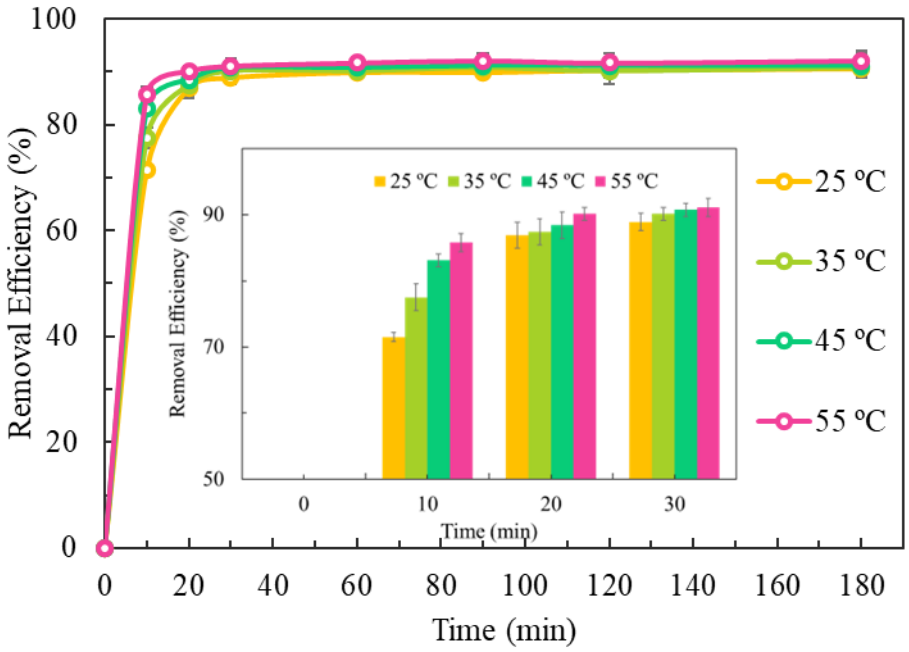

Figure 4.12. Effect of solution temperatures on CAP removal behavior of nZVI/O–GO-1:1

$\Delta H°$, $\Delta G°$, and $\Delta S°$ are useful thermodynamic variables for expressing the removal process's heat change, feasibility, and spontaneity, respectively. The third thermodynamic principle can be used to get the value of ΔG° from Eq. (2.19), while Van't Hoff plotting (*ln Kd* versus 1/*T*), as illustrated in Figure 4.13, can determine the value of $\Delta H°$ and $\Delta S°$ via its slope and interception. Table 4.2 lists the computed thermodynamic parameters at various temperatures (ranging from 25 to 55 °C). The CAP adsorption by nZVI/O-GO was confirmed endothermic by the rising trend of K_d with temperature. A convincing argument for the thermodynamic viability and spontaneous reaction mechanism between CAP and the nanocomposite was provided by the negative sign given by $\Delta G°$ for the nZVI/O-GO at all reaction temperature levels. As the temperature rose, $G°$ became more hostile, indicating that CAP adsorption rose. In addition, a positive result of ΔH° (4.7379 kJ mol^{-1}) indicated that the CAP was removed by endothermic adsorption from the nanocomposite. Furthermore, $\Delta S°$ (46.0415 kJ $mol^{-1}K^{-1}$) displays a positive value that reflects an increase in the unpredictability of the CAP/nanocomposite connection for the adsorption process. The results of Wu et al. [162] for the CAP removal by activated carbon/nZVI nanocomposite align with this tendency. Furthermore, the magnitude of ΔG° varied between 20 and 80 kJ/mol at various temperatures, and that $\Delta H°$ was less than 20 kJ/mol might suggest that the removal of CAP involves the physisorption process.

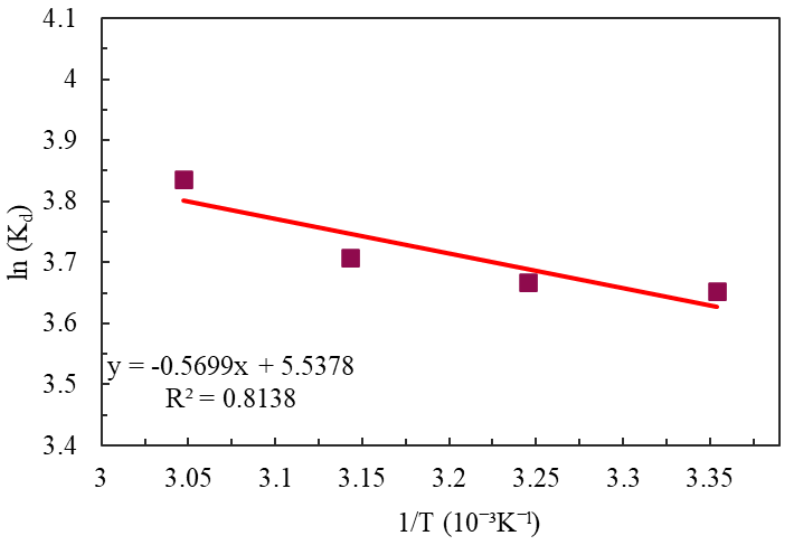

Figure 4.13. Van't Hoff plotting of nZVI/O–GO-1:1

Table 4.2. Parameters of thermodynamic analysis for the removal of CAP by nZVI/O–GO-1:1.

Temperature, (K)	Thermodynamic equilibrium constant, (K_d)	Gibbs free energy change, (ΔG°) (kJ mol^{-1})	Enthalpy change, (ΔH°) (kJ mol^{-1})	Entropy change, (ΔS°) (kJ mol^{-1} K^{-1})
298.15	38.571	-9.0539	4.7379	46.0415
308.15	39.143	-9.3953		
318.15	40.741	-9.8060		
328.15	46.333	-10.4651		

4.8. Iron ion leaching

For both nZVI and nZVI/O-GO-1:1 with the dose of 0.25 g/L, the total dissolved iron, ferrous (Fe^{2+}), and ferric (Fe^{3+}) concentrations in CAP solutions at pH 5 were recorded within 3 hours to evaluate the iron ion leaching. According to Figure 4.14a, nZVI/O-GO-1:1 had a lower rate of total iron leaching than nZVI. The nZVI/O-GO-1:1 nanocomposite's release of electrons due to the solid/liquid reaction was adequate for the reductive breakdown of CAP despite the slower rate of iron leaching. Fe^{2+} concentration for nZVI fell consistently after 30 min and dramatically after 60 min of reaction, as shown in Figure 4.14b. Even while the concentration of Fe^{2+} for nZVI/O-GO-1:1 did not drop suddenly, it remained almost constant and lasted up to 180 minutes of reaction, as shown in Figure 4.14c. These patterns are consistent with previous research [28], [128]. The crumpled GO sheets provide unique characteristics for capturing ions and inhibiting them from flowing into the solution, which leads to much fewer leached ions found in the nZVI/O-GO-1:1 system than in the bare nZVI system.

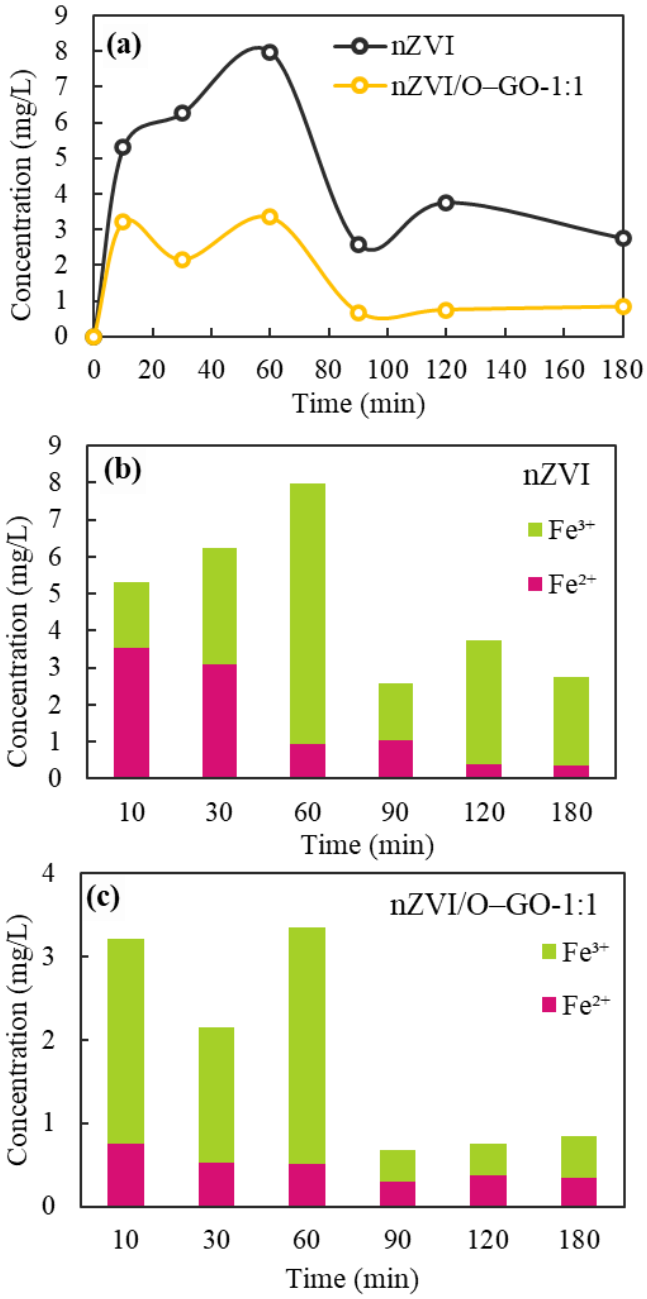

Figure 4.14. Iron leaching in CAP solution: (a) Total iron leaching by bare nZVI and nZVI/O–GO-1:1; (b) Ferrous and ferric iron leaching by bare nZVI; (c) Ferrous and ferric iron leaching by nZVI/O–GO-1:1

4.9. Desorption analysis and proposed CAP removal mechanism

Several desorption experiments were carried out to understand and pinpoint the CAP removal process by determining the CAP desorption capability from the nZVI/O-GO-1:1

surface. The CAP desorption trends for the four distinct eluents during the three hours contact period are shown in Figure 4.15a. With a longer contact time, the concentration of CAP desorbed from nZVI/O-GO-1:1 rose until it plateaued. Equilibrium of CAP desorption was reached in 30 min with NaCl, ethanol, and deionized water as eluents and in 1 h with NaOH solution.

The CAP desorption capacity of nZVI/O-GO-1:1 during 24 h in four different eluents is shown in Figure 4.15b. The figure demonstrates that NaOH, NaCl, ethanol, and deionized water all had desorption capacities of 7.39 mg/g, 5.7 mg/g, and 1.71 mg/g at 24-hour intervals, respectively. NaOH had the largest desorption capacity of CAP from the surface of nZVI/O-GO-1:1 at 18.21 mg/g. These eluents displayed various desorption outcomes because each eluent may break the constrained adsorbate bonds with different composites, depending on various contaminant and adsorbent types [147]. The CAP desorption capacity of NaOH and NaCl used as eluents was greater than that of other eluents because these two solutions are ionic compounds composed of Na+, OH^-, and Cl^-, often used as desorption agents for complex pollutants. The separation of the CAP soluble bonds into solution was made possible by the capacity of OH^- to generate numerous hydrates. In the system, Cl^- ions may also engage with the active region of the adsorbent, releasing CAP molecules [49]. Likewise, the system's pH was raised, and the desorption reaction's reactivity was boosted by adding OH^- [49].

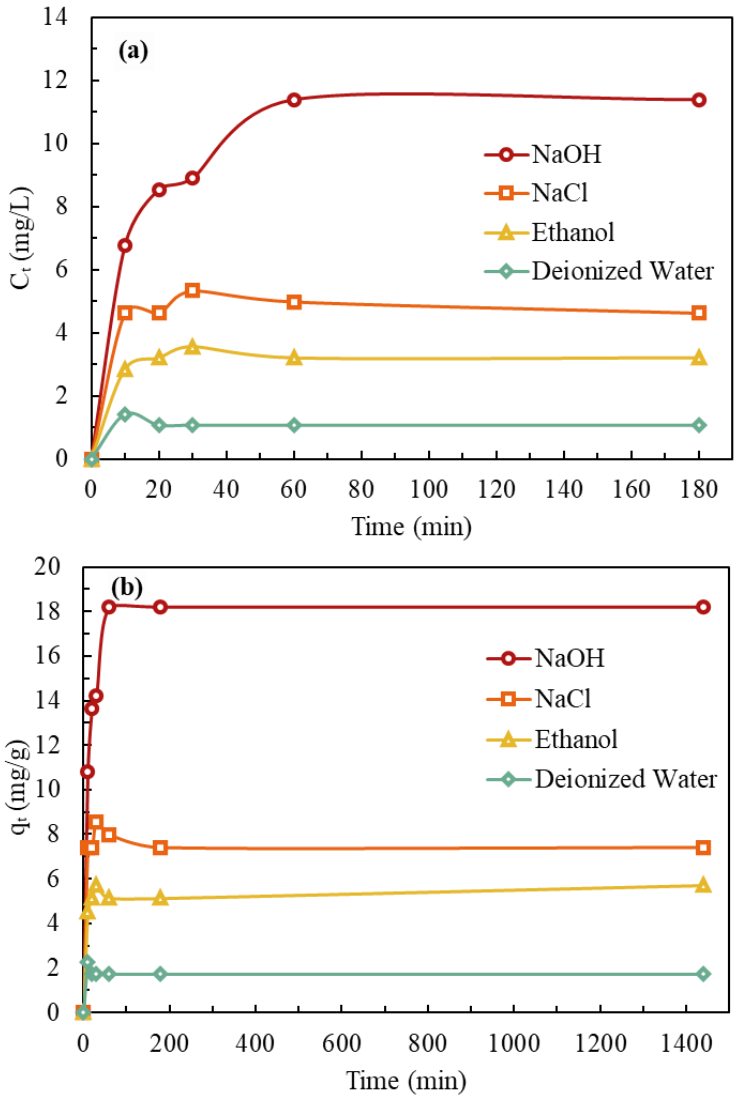

Figure 4.15. Desorption analysis of nZVI/O–GO-1:1: (a) eluents' CAP desorption profiles over the three hours of contact time; (b) CAP desorption capacity throughout 24 hours.

In addition to the kinetics study that was previously addressed, the findings of the desorption study also amply demonstrated that the adsorption mechanism had little role in CAP removal. To control the whole process, the quantity removed by this technique needs to be more significant. This claim is backed up by the CAP desorption performance displayed in Figure 4.16a, which indicates that nZVI/O-GO-1:1 had a poor desorption efficiency (less than 5%) in all investigated eluents and that oxidation was primarily responsible for CAP removal. More than 96% of CAP may be desorbed from GO in NaOH and NaCl solutions (Figure 4.16b), making GO a more efficient CAP adsorbent than bare nZVI. However, with desorption efficiencies of just 18% and 5%, respectively,

ethanol and deionized water as eluent were not beneficial to the desorption process of CAP from GO. However, the CAP desorption process for the bare nZVI proceeded slowly, with the maximum desorption efficiency for any of the tested eluents being 8.5%. Furthermore, in deionized water, CAP desorption by nZVI was undetectable. This result demonstrates that the adsorption process is wholly included in GO and that GO, as one of the nZVI/GO nanocomposite components, contributed more to the removal of CAP through the adsorption mechanism than to nZVI.

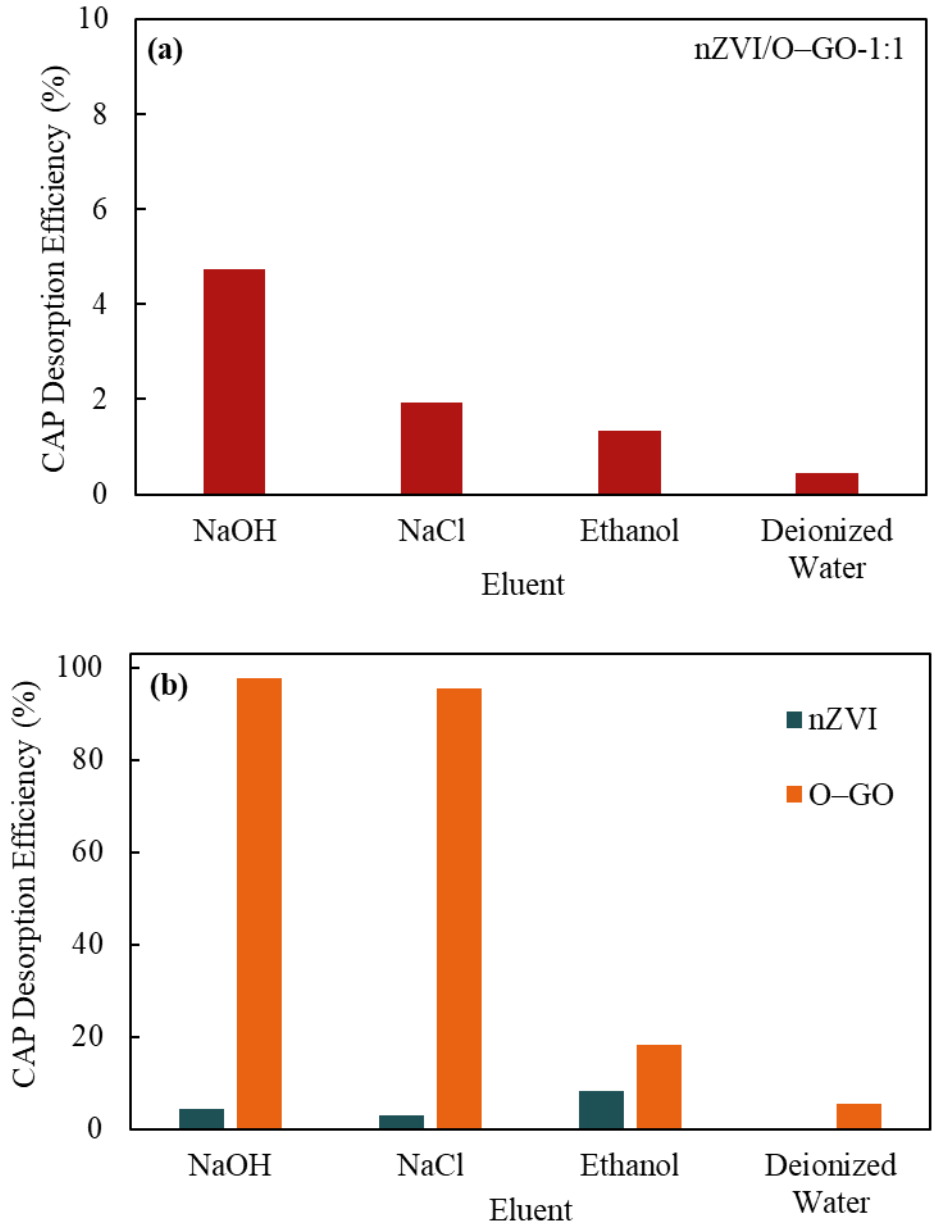

Figure 4.16. CAP desorption efficiency: (a) nZVI/O–GO-1:1; (b) bare nZVI and O–GO

The FTIR analysis was carried out to explore the alterations in surface functional groups on nZVI/O-GO-1:1 before and after the CAP removal activity to discover possible removal processes. As described in Figure 4.17, the peak in the nZVI/O-GO-1:1 spectrum at 3275 cm^{-1} was brought on by the O-H stretching vibration caused by moisture, indicating that the hydroxyl frameworks were present inside graphite interlayers. Moreover, the stretching modes of the C=O group, the O=C-O carboxyl, and the C-O epoxide were responsible for the peaks at 1556 cm^{-1}, 1375 cm^{-1}, and 1042 cm^{-1}, respectively. After the CAP was removed, the spectra of the spent nZVI/O-GO-1:1 underwent a slight transformation, which signifies that a portion of the CAP was removed by adsorption onto the surface of the nZVI/O-GO-1:1.

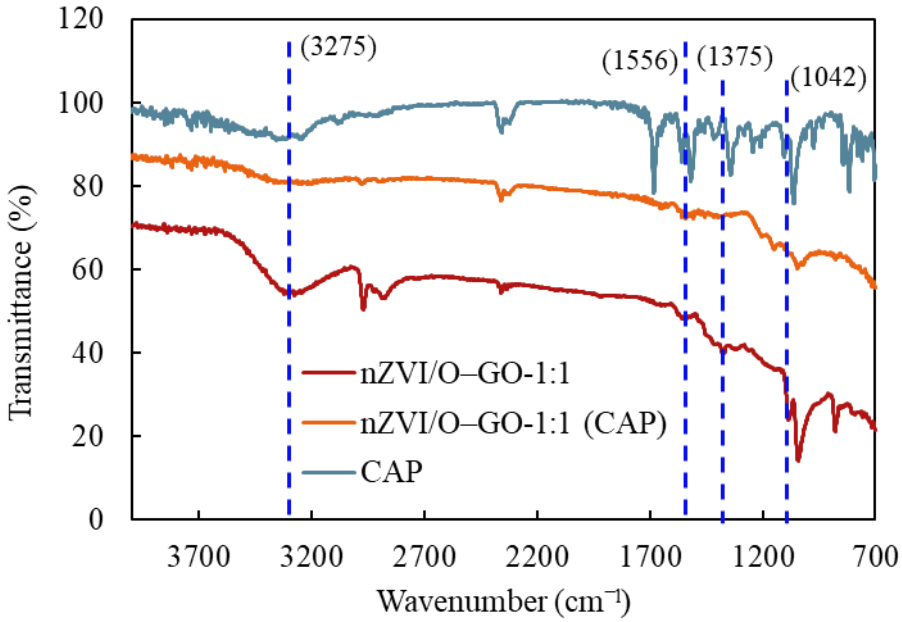

Figure 4.17. FTIR spectra of nZVI/O–GO-1:1 before and after CAP removing activity in water.

According to desorption experiments and FTIR spectra, the surface of GO was the only place where an adsorption process removed CAP. This occurrence happened due to the nanocomposite containing GO and OCFGs that might react with the CAP to promote removal behavior. Since the active surface was more probable to establish a bind with nZVI, CAP removal via adsorption was negligible. By generating free radicals that oxidized CAP, the nZVI oxidation process helped remove the remaining amounts of CAP. An SEM image of wasted nZVI/O-GO-1:1 and an EDX analysis could be used to support

these processes. The chlorine (Cl) signal is apparent in the EDX spectrum, as shown in Figure 4.18a**,** indicating the fact that the CAP element has been adsorbed by nZVI/O-GO-1:1 on the GO surface as evidenced by the needle-like and barbed image structure on the material's surface, as shown in Figure 4.18b. Due to the high reactivity of nZVI, which oxidized to create magnetite (Fe_3O_4) when interacting with oxygen in the air during the test, an oxygen (O) peak appears in the EDX spectra. In contrast, the peaks of the Fe and C elements suggest the purity of the nZVI/O–GO-1:1 produced and the deposition of nZVI on the surface of the GO.

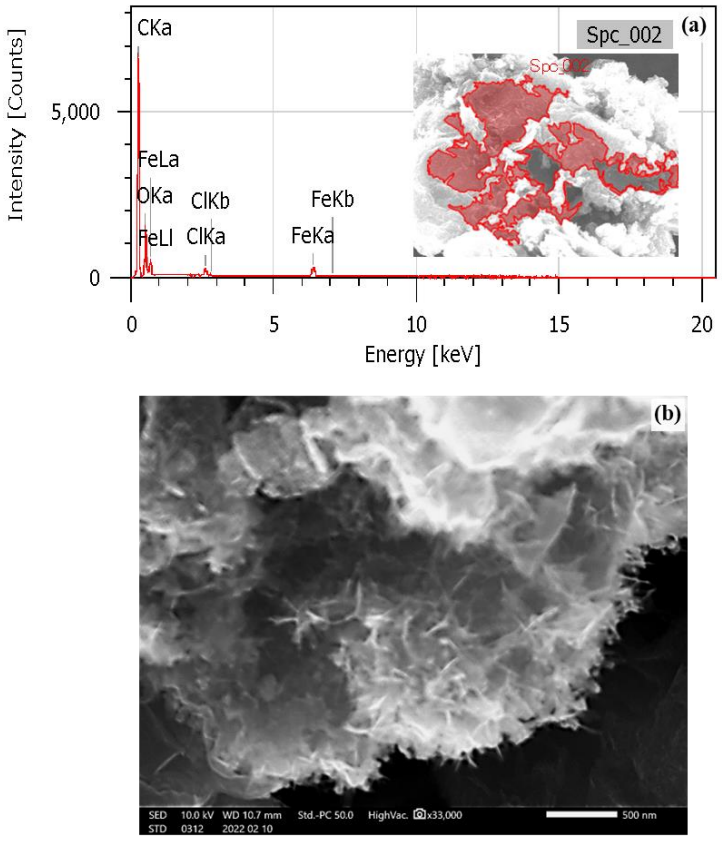

Figure 4.18. Spent nZVI/O–GO-1:1 sample (a) EDS analysis; (b) SEM image

The perceived activation energy, E_a (kJ/mol), was calculated using an analysis of statistics to confirm the participation of nZVI oxidation in the elimination of CAP. The Arrhenius plot for the elimination of CAP by nZVI/O-GO-1:1 is depicted in Figure 4.19. The activation energy (E_a) was computed via the Arrhenius equation, represented by Eq. (4.1) [141].

$$-\ln\ k_2 = \frac{E_a}{RT} + \ln A \qquad (4.1)$$

The k in the equation is the apparent rate constant of CAP removal determined by the pseudo-second-order kinetics model. A represents the pre-exponential component, R is the universal gas constant and T for absolute temperature. For the elimination of CAP, the computed E_a value of nZVI/O-GO-1:1 was 33.33 kJ/mol. E_a varies between 10 and 13 kJ/mol for diffusion-controlled reactions [141]. Thus, a higher E_a shown by nZVI/O-GO-1:1 reveals that the intrinsic chemical reaction instead of the mass transfer controls the CAP removal.

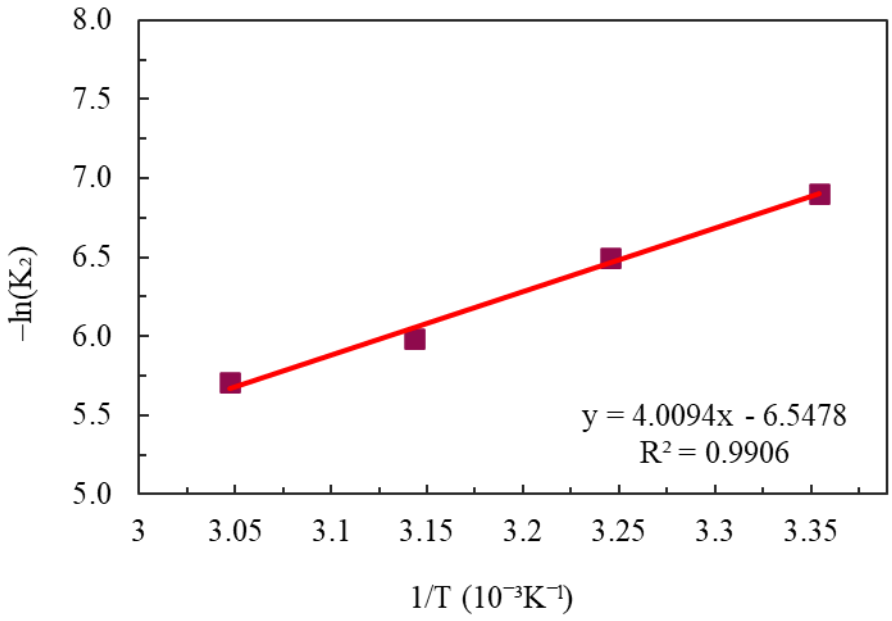

Figure 4.19. Arrhenius plot of CAP removal by nZVI/O–GO-1:1

4.10. Stability and recyclability of GO/nZVI nanocomposite and its practical implication

Figure 4.20 shows the nZVI/O-GO-1:1 XRD patterns before and after (spent) the reaction with CAP. The peaks of the crystal structure can be recognized in both samples, but they vary to some extent. In the XRD pattern of the spent sample, the Fe^0 peak remains detectable at 44.78° and 63.1°, whereas the graphitic (G) peak corresponding with the crystallographic plane (002) can be seen at 25.5°. These peaks indicate that the nZVI/O-GO-1:1 nanocomposite retained its stability after reacting for over 3 h with an

exceptionally concentrated CAP solution. Fe_3O_4 is accountable for the significant and low-intensity peaks visible at 25.7° and 57.5°, created due to Fe^0 corrosion and iron ion leaching during the CAP removal process. This result is consistent with Xing et al. [84], who eliminated atrazine using an nZVI/GO nanocomposite. Furthermore, using Scherrer's equation, it was discovered that the average crystal size of nZVI/O-GO-1:1 was 4.97 nm and expanded to 12.14 nm when it interacted with CAP.

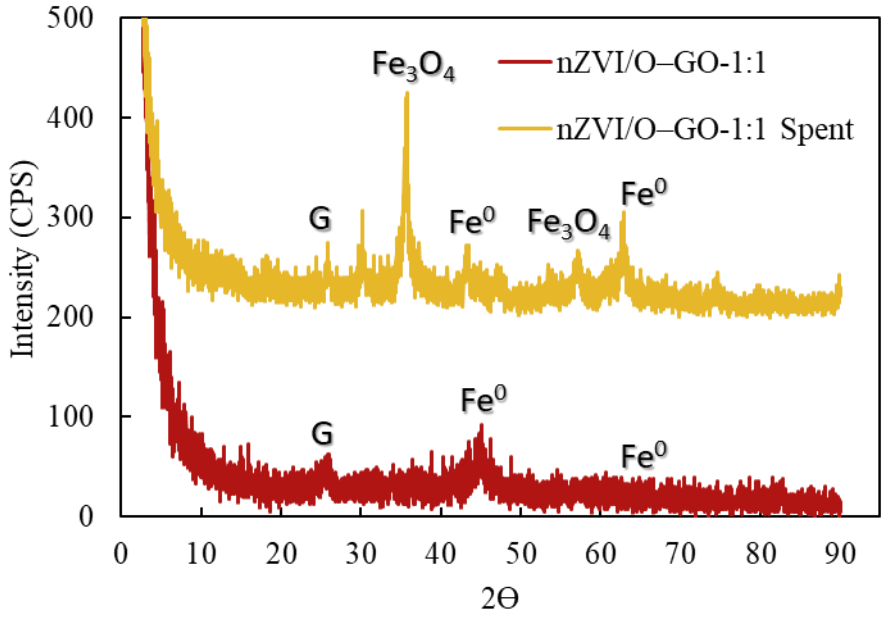

Figure 4.20. XRD patterns of nZVI/O–GO-1:1 before and after the reaction with CAP

One feature that demonstrates the material's resilience in the real world of the wastewater treatment business is its recycling capacity to facilitate the purification of contaminated water. In order to evaluate the recyclability of nZVI/O-GO-1:1, the reusability experiment was conducted by producing and reusing the nanocomposite. The used nZVI and nZVI/O-GO-1:1 were vacuum filtered and sonicated in 1M NaOH at 45°C for 30 minutes in the present investigation. The collected regenerated particles were then vacuum-filtered, cleaned with ethanol and deionized water, dried, and reused in a manner similar to the first recycling. Three regeneration cycles were used to assess the recyclability of nZVI and nZVI/O-GO-1:1, and the results are presented in Figure 4.21. The results show that when the recycle number grew, the removal efficiency of nZVI and nZVI/O-GO-1:1 diminished. Nevertheless, nZVI/O-GO-1:1 performed CAP removal considerably better than nZVI following regeneration and reuse. With an 82% CAP

removal effectiveness in the first recycling, nZVI/O-GO-1:1 still showed impressive CAP removal capabilities. For the subsequent recycling, the CAP removal performance declined; the third recycle showed a 51% CAP removal efficiency. However, bare nZVI demonstrated a considerable decline in CAP removal efficacy after its first recycling, and its removal efficiency was only about one-fourth of what had been seen before recycling. The pattern documented by earlier studies [162] aligns with the nZVI recyclability pattern for CAP removal. The iron leaching and oxidation caused by the solid-solution interaction, which reduced the amount of exposed active sites on the nZVI interface for CAP removal, were among the factors attributed to the lowering trend. The slower ion leaching and oxidation of nZVI caused by GO's involvement as an attachment medium made nZVI more recyclable than bare nZVI. The efficiency of CAP removal diminished when they were recycled due to the possibility of particle loss and severe corrosion during the regeneration process. This result shows that nZVI/O-GO-1:1, even recycled, has outstanding stability and application supremacy for CAP removal.

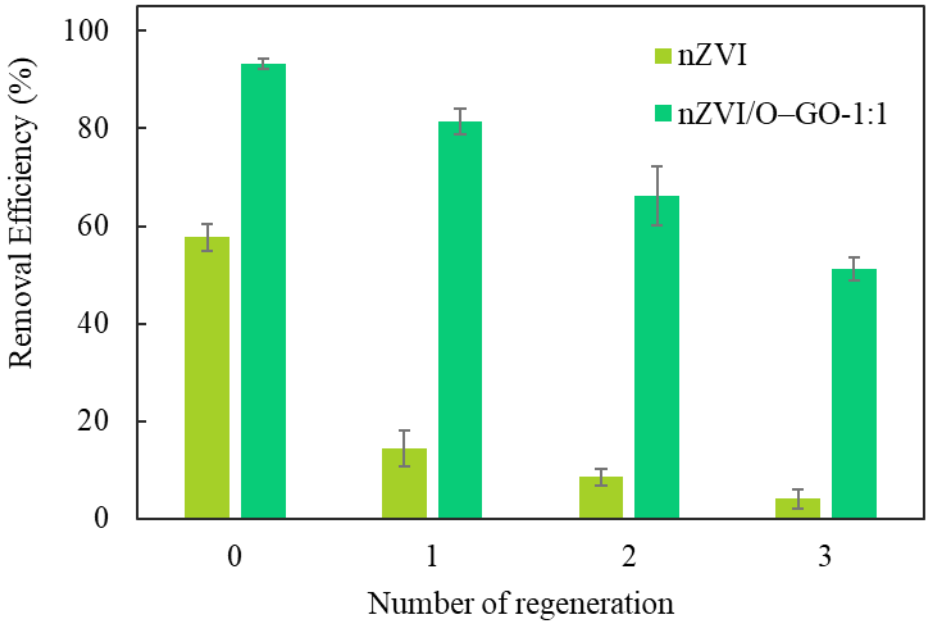

Figure 4.21. Regeneration of bare nZVI and nZVI/O–GO-1:1 in CAP removal

Batch studies investigated the practical feasibility nZVI/O-GO-1:1 for CAP removal in natural aqueous environments. The experiments used natural surface water collected from the Ushikubi River in Fukuoka City, Japan. Figure 4.22 illustrates the efficiency of nZVI/O-GO-1:1 in eliminating 20 mg/L of CAP from natural surface water across

varying periods (1 hour and 24 hours) and dosages. The empirical evidence suggests that a reduced quantity of nanocomposite does not yield any advantageous outcomes in removing CAP. Conversely, it was observed that the elimination efficacy of CAP exhibited a significant surge upon elevating the dosage to 0.15 g/L. The efficacy of CAP removal from the aqueous environment was enhanced with an upsurge in nanocomposite dosage, resulting in the effective elimination of over 95% of CAP within 1 hour at a dosage of 0.5 g/L. The nanocomposite dosage of 0.25 g/L can eliminate all CAP present in natural surface water within 24 hours. The limited removal efficiency observed at low dosages can be attributed to the restricted functionality of the substance and the limited number of active sites available on its surface for the removal of CAP, particularly in the presence of various other contaminants in the water matrix. Consequently, the augmentation of the dosage resulted in a higher number of active sites on the material's surface, leading to the removal of the CAP. The previous observation aligns with the pattern observed in the experiment, wherein the efficacy of CAP removal demonstrates an upward trend in correlation with the dosage increment. The results indicate that using nZVI/O-GO in a 1:1 ratio is a highly feasible approach for removing CAP in an aqueous environment.

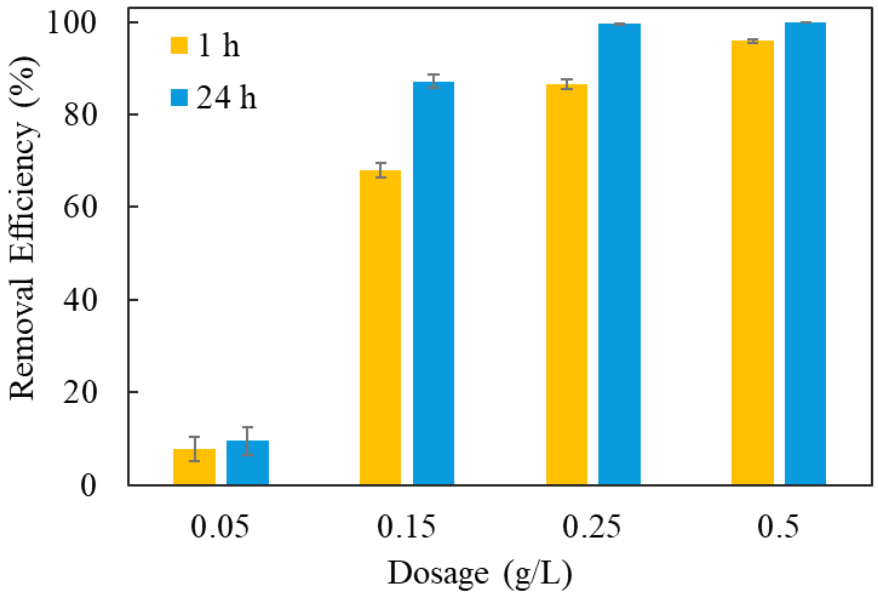

Figure 4.22. The performance of nZVI/O–GO-1:1 in removing CAP from natural surface water at different time intervals and dosages

Chapter 5

Conclusions and Recommendations

5.1. Major Findings and Conclusion

Antibiotics have emerged as contaminants that have raised concerns within the global community over the past two decades. The extensive utilization of antibiotics without stringent regulation, aggravated by their misuse in the agricultural industry, has led to active antibiotic residues in water sources. The existence of this substance in aquatic environments poses a significant risk to both human well-being and ecological systems, leading to severe environmental contamination. Thus, the environmental issue has garnered the attention and curiosity of scholars to investigate alternative approaches for eliminating antibiotics from the environment.

The present study was conducted to address the antibiotic waste contamination issue in water. Specifically, the study sought to apply material engineering and nanotechnology approaches by utilizing a combination of GO and nZVI and to report the findings thereof. Despite extensive research on the applications of GO and nZVI in various fields over the past few decades, their potential for treating water contaminated with antibiotic residues still needs to be explored. This chapter encompasses the primary outcomes of the investigation as well as potential avenues for future research.

The present study yielded significant outcomes, which can be summarized as follows:

I. This present study has found that the parameters of the GO production process through the chemical synthesis method substantially influence the performance of GO in removing CIP from contaminated water. These parameters encompass the aspects of the chemical used, the existence of the catalyst, and the reaction's duration in each phase. Utilizing an indeterminate amalgamation of parameters may result in the excessive oxidation or insufficient oxidation of graphite, thereby impacting both the cost of production and the efficacy of GO in eliminating CIP from aqueous solutions.

II. Facile GO chemical synthesis was successfully developed by empirically optimizing the parameters of each synthesis stage based on a time and chemical-saving protocol and considering the excellent CIP removal performance of the produced GO. The optimal synthesis conditions in the H_2SO_4 intercalated graphite transformation stage are achieved by intercalating 1 g of graphite with 20 mL of

H_2SO_4 for 10 min reaction time. Then, the optimal conditions in the graphite oxide transformation stage are using 3 g of $KMnO_4$ at a reaction temperature below 4 °C for 10 min, followed by a reaction at a controlled temperature of 38 °C for 20 min. 50 mL of DIW and a 5 min reaction period are ideal and adequate in the GO transformation stage. Lastly, the optimal synthesis condition in the reduction stage is attained using 3 mL of H_2O_2.

III. Although the optimized GO synthesis process uses minimal chemicals and reaction time compared to conventional syntheses, the morphological attributes of the resulting GO exhibited no flaws. This optimized synthesis produced GO with a lamellar sheet structure with a distinctive wrinkled morphology on the graphene basal plane and crumpled at its edges, consistent with the characteristic morphology observed in GO produced by conventional methods.

IV. The optimized synthesis of GO yields superior quality GO (O–GO) in terms of CIP removal compared to conventional synthesis methods. The study demonstrated that O-GO exhibited a removal efficiency of 72% compared to the performance shown by S–GO and F–GO, which displayed removal efficiencies of 34% and 40%, respectively, when administered at a dosage of 0.25 g/L against a CIP aqueous concentration of 100 mg/L.

V. From a material cost perspective, the O–GO's most cost-effective CIP removal was at a dosage of 0.6 g/L and 0.25 g/L for high (greater than 75 mg/L) and low (less than 50 mg/L) CIP concentrations, respectively. The optimal removal efficiency of GO for CIP is attainable at medium with an initial pH value between 5 and 9, with a removal rate of 97-98%. The reaction temperature was found to have no significant impact on the CIP removal performance.

VI. The kinetic analysis determined that the CIP removal was better suited to the Elovich and PFO model when the CIP concentrations were low, whereas the PSO model was better suited for high concentrations. The findings obtained from the kinetics analysis, FTIR analysis, and desorption experiments collectively suggest that the potential mechanism of CIP removal may involve a combination of physisorption and chemisorption processes.

VII. The O-GO exhibits a notable capacity for CIP desorption, indicating a promising potential for its application in regeneration and reuse. The desorption capacity of CIP by O-GO was significantly high within a brief reaction period of 10 minutes upon employing 1 M NaOH as the desorption eluent. The desorption efficiency of CIP was observed to be greater than 75% and nearly 83% after 2 and 24 h of reaction, respectively.

VIII. The outcomes indicate that O-GO presents the lowest materials cost per 1 mg of CIP removal, with a material cost of only 0.2195 ¥/mg. In contrast, S-GO and F-GO have materials costs of 1.3776 ¥/mg and 0.6550 ¥/mg, respectively. The optimized synthesis of O-GO requires a shorter processing duration, suggesting that it is a more economical choice for CIP removal from water.

IX. The GO precursor utilized in the fabrication of nZVI/GO nanocomposite substantially impacts its morphological characteristics. Incorporating O-GO as a precursor of nZVI/GO nanocomposite is beneficial to nZVI as the morphology of this material demonstrates that nZVI nanoparticles have been precipitated uniformly on the GO surface without any significant particle aggregation. However, the nZVI particles exhibit aggregation and dispersion tendencies, resulting in a spotted clustering pattern that forms a coralline structure in the nZVI/GO nanocomposite morphology utilizing S-GO and F-GO as GO precursors.

X. The GO precursor significantly impacted the capability of the nZVI/GO to remove CAP. The nZVI/GO nanocomposite synthesized with O-GO as a precursor exhibited superior removal efficiency, achieving a 90% removal rate. In contrast, nZVI/GO synthesized with S-GO and F-GO demonstrated lower removal efficiencies, approximately 45%, and 47%, after 3 hours of reaction, respectively.

XI. From an economic perspective, optimization of CAP removal conditions suggested that a 1:1 nanocomposite mass ratio of nZVI to O-GO at a dosage of 0.25 g/L was the optimal CAP removal condition for achieving up to 90% elimination of 100 mg/L CAP in a natural solution pH and 91% in initial pH 5.

XII. The findings of the kinetics study indicate that the removal of CAP at low concentrations exhibited perfect compatibility with the PSO model. In contrast, high concentrations were observed to correspond with the PFO model.

XIII. Based on a set of thermodynamics analyses, kinetics assessments, and desorption tests, it can be inferred that the adsorption and oxidation mechanism facilitated the elimination of CAP by nZVI/O-GO-1:1. The role of the GO component in the nZVI/O-GO nanocomposite system is recognized to be significant in the elimination of CAP via the mechanism of adsorption.

The Table 5.1 presents comparative data on the performance of removing ciprofloxacin and chloramphenicol exhibited by the nanomaterials introduced in this study in relation to the performance of other materials reported in previous studies. The Optimized GO and nZVI/O-GO nanocomposite showed excellent antibiotic removal performance, with over 90% removal efficiency for antibiotics with high initial concentration. The materials introduced in this study have significant potential for large-scale development and could be widely used in water treatment contaminated with antibiotics due to the material cost-effectiveness achieved through synthesis optimization.

Table 5.1. Material performance comparison for ciprofloxacin and chloramphenicol removal from aqueous solution.

Antibiotics	Material	Antibiotic Concentration (mg/L)	Dosage (g/L)	Removal capacity (mg/g)	Removal Efficiency (%)	Ref.
CIP	Optimized GO	100	0.6	164	97	This study
	Conventional GO	20	0.02	145	14.5	[135]
	Multi-walled carbon nanotubes	150	0.5	192	64	[163]
	nZVI–Magnesium Hydroxide	100	0.5	192	96.31	[49]
	nZVI and 0.3 mM Oxalate	100	0.3	319.13	95.74	[28]
	nZVI	100	0.3	150.13	45.04	[28]
	Zinc Oxide–Jack Fruit Peel Activated Carbon	50	0.3	146.66	88	[164]
	Biochar decorated with Nickel sulfide (NiS)	100	2	20	40	[165]
	Polyvinylpyrrolidone (PVP) and nZVI with copper (Cu)	100	1	87.7	87.7	[166]
CAP	nZVI–O-GO	100	0.25	384.05	91	This study
	nZVI–Activated Carbon	97	0.2	329.8	68	[65]
	nZVI–Carbon nanotubes (CnT)	97	0.2	465.6	96	[65]
	Biochar–supported Cobalt (II,III) oxide (Co_3O_4) composite (Incorporated with peroxymonosulfate, 10 mM)	30	0.2	145.5	97	[159]
	Sulfide-nZVI (activated persulfate PS, 3 mM)	20	0.1	196	98	[160]
	nZVI activated peroxymonosulfate system (PMS, 0.2 mM)	10	0.5	19	95	[167]

5.2. Recommendation

Based on the significant findings mentioned earlier, the followings recommendations are put forth:

I. Before using this nanomaterial in a pilot project or an already-existing water treatment unit facility, disruption studies and its practical application in laboratory settings are imperative to be conducted. It is essential to consider the impact of environmental interference on removal efficiency when designing treatment equipment or process and estimating the necessary treatment dosage.

II. The effectiveness of this particular nanomaterial is notable in its exclusive capacity to eliminate CIP and CAP from aqueous solutions. Examining the performance of this nanomaterial in aqueous environments containing elevated levels of medical pollutants, such as those found in hospital and pharmaceutical industry effluents, would yield significant advantages.

III. This investigation exclusively employs nZVI in conjunction with GO to fabricate magnetic nanocomposites, with the primary function of the GO being to prevent nZVI agglomeration. Examining the efficacy of graphene oxide (GO) as a supporting material for other magnetic substances, such as copper, or utilizing GO to fabricate a nanocomposite with a 3-component matrix composite would yield more tremendous advantages in water treatment applications.

5.3. Future Work

This work constitutes the subsequent research phase to pursue the further achievement of this doctoral thesis.

5.3.1. Proposal background

The exceptional physical and chemical properties of Graphene Oxide (GO) have garnered significant attention in various scientific and technological domains. This material exhibits immense potential for utilization in various applications, including but not

limited to energy storage devices, field effect transistors (FET), water purification, sensors, and transparent conductive films.

The synthesis of GO is primarily facilitated by using graphite powder as its precursor. Graphite is found in three distinct forms in its natural state: amorphous, crystalline flakes, and crystal lumps or veins. Graphite can be categorized into two types: natural graphite and synthetic graphite. Graphite can be manufactured from graphitization by utilizing hydrocarbon precursors. Numerous natural substances exhibit elevated levels of hydrocarbon compounds. Palm products are considered to be materials with high carbon content. This palm-derived commodity can potentially serve as a viable graphite source in the production of graphene oxide (GO).

Malaysia is recognized as a leading global producer of palm oil commodities. Consequently, a substantial quantity of palm waste, including empty fruit bunches (EFB), palm kernel shells (PKS), palm leaves, and stems, are generated in conjunction with palm oil production. Palm oil manufacturing produced approximately 23 million tons of palm waste in 2017. Therefore, utilizing this waste as a precursor for GO confers significant advantages. The combination of GO derived from palm oil waste and nZVI can yield highly suitable nanocomposites in the water treatment domain.

Accordingly, the proposed project is titled “Removal of Emerging Antibiotic Contaminants from Aquatic Environments by Bio-Graphene Oxide Magnetic Nanocomposites.”

5.3.2. Aim of the proposed research

By considering the advantages of GO, this research aims to employ this Bio-GO incorporate with nZVI producing magnetic Bio-Graphene Oxide nanocomposites to eliminate the antibiotic contaminant from environment water.

5.3.3. Expected results and impacts

I. Using palm waste as a graphite source in producing effective GO-nZVI base nanocomposite in water treatment application.

II. Produce an innovative, effective, and better Bio-GO nZVI-based nanocomposite to efficiently remove antibiotic contaminants from water.

III. Contemplating the magnetic separation of the Bio-GO nZVI-based nanocomposite upon completion of the removal activity.

IV. Extraordinary efficiency in treating water contaminated with antibiotics by the specified Bio-GO nZVI-based nanocomposite, particularly when optimal treatment conditions are met.

V. Developing a Bio-GO nZVI-based nanocomposite material that is cost-effective and highly efficient for removing antibiotics from aquatic environments.

References

[1] "Drinking-water." https://www.who.int/news-room/fact-sheets/detail/drinking-water (accessed Mar. 14, 2023).

[2] WHO and UNICEF, *Progress on drinking water, sanitation and hygiene: 2017 update and SDG baselines.* 2017.

[3] C. Lee Goi, "The river water quality before and during the Movement Control Order (MCO) in Malaysia," *Case Stud. Chem. Environ. Eng.*, vol. 2, p. 100027, Sep. 2020, doi: 10.1016/J.CSCEE.2020.100027.

[4] "Ending preventable deaths from pneumonia and diarrhoea by 2025." https://www.who.int/news/item/10-04-2013-ending-preventable-deaths-from-pneumonia-and-diarrhoea-by-2025 (accessed Mar. 14, 2023).

[5] M. B. Ahmed, J. L. Zhou, H. H. Ngo, and W. Guo, "Adsorptive removal of antibiotics from water and wastewater: Progress and challenges," *Sci. Total Environ.*, vol. 532, pp. 112–126, Nov. 2015, doi: 10.1016/J.SCITOTENV.2015.05.130.

[6] S. M. Praveena *et al.*, "Pharmaceuticals residues in selected tropical surface water bodies from Selangor (Malaysia): Occurrence and potential risk assessments," *Sci. Total Environ.*, vol. 642, pp. 230–240, Nov. 2018, doi: 10.1016/J.SCITOTENV.2018.06.058.

[7] S. Fekadu, E. Alemayehu, R. Dewil, and B. Van der Bruggen, "Pharmaceuticals in freshwater aquatic environments: A comparison of the African and European challenge," *Sci. Total Environ.*, vol. 654, pp. 324–337, Mar. 2019, doi: 10.1016/J.SCITOTENV.2018.11.072.

[8] M. Ashfaq *et al.*, "Occurrence, spatial variation and risk assessment of pharmaceuticals and personal care products in urban wastewater, canal surface water, and their sediments: A case study of Lahore, Pakistan," *Sci. Total Environ.*, vol. 688, pp. 653–663, Oct. 2019, doi: 10.1016/J.SCITOTENV.2019.06.285.

[9] WHO, *Safe Water, Better Health*. 2019.

[10] M. fang Li *et al.*, "Performance of magnetic graphene oxide/diethylenetriaminepentaacetic acid nanocomposite for the tetracycline and ciprofloxacin adsorption in single and binary systems," *J. Colloid Interface Sci.*, vol. 521, pp. 150–159, Jul. 2018, doi: 10.1016/J.JCIS.2018.03.003.

[11] X. Wang, R. Yin, L. Zeng, and M. Zhu, “A review of graphene-based nanomaterials for removal of antibiotics from aqueous environments,” *Environ. Pollut.*, vol. 253, pp. 100–110, 2019, doi: 10.1016/j.envpol.2019.06.067.

[12] “Contaminants of Emerging Concern.” https://portal.ct.gov/DEEP/Remediation--Site-Clean-Up/Contaminants-of-Emerging-Concern/Contaminants-of-Emerging-Concern (accessed Mar. 27, 2023).

[13] S. H. Joo, Y. Liang, M. Kim, J. Byun, and H. Choi, “Microplastics with adsorbed contaminants: Mechanisms and Treatment,” *Environ. Challenges*, vol. 3, p. 100042, Apr. 2021, doi: 10.1016/J.ENVC.2021.100042.

[14] A. M. E. Khalil, F. A. Memon, T. A. Tabish, D. Salmon, S. Zhang, and D. Butler, “Nanostructured porous graphene for efficient removal of emerging contaminants (pharmaceuticals) from water,” *Chem. Eng. J.*, vol. 398, no. May, p. 125440, 2020, doi: 10.1016/j.cej.2020.125440.

[15] “Dealing with Emerging Contaminants: Types and Specific.” https://www.cascade-env.com/resources/blogs/dealing-with-emerging-contaminants/ (accessed Mar. 27, 2023).

[16] M. Achparaki *et al.*, “Classification, Potential Routes and Risk of Emerging Pollutants/ Contaminant,” *Intech*, p. 13, 2012, [Online]. Available: http://dx.doi.org/10.1039/C7RA00172J%0Ahttps://www.intechopen.com/books/advanced-biometric-technologies/liveness-detection-in-biometrics%0Ahttp://dx.doi.org/10.1016/j.colsurfa.2011.12.014.

[17] Mohd Faizul Idham, O. Falyouna, and O. Eljamal, “Effect of Graphene Oxide Synthesis Method on The Adsorption Performance of Pharmaceutical Contaminants,” *Proc. Int. Exch. Innov. Conf. Eng. Sci.*, vol. 7, pp. 232–239, 2021, doi: 10.5109/4738593.

[18] Y.-L. Cheng *et al.*, “We are IntechOpen , the world ’ s leading publisher of Open Access books Built by scientists , for scientists TOP 1 %,” *Intech*, vol. 11, no. tourism, p. 13, 2016, [Online]. Available: https://www.intechopen.com/books/advanced-biometric-technologies/liveness-detection-in-biometrics.

[19] H. K. Bayabil, F. T. Teshome, and Y. C. Li, “Emerging Contaminants in Soil and Water,” *Front. Environ. Sci.*, vol. 10, no. March, pp. 1–8, 2022, doi: 10.3389/fenvs.2022.873499.

[20] V. K. Parida, D. Saidulu, A. Majumder, A. Srivastava, B. Gupta, and A. K. Gupta,

"Emerging contaminants in wastewater: A critical review on occurrence, existing legislations, risk assessment, and sustainable treatment alternatives," *J. Environ. Chem. Eng.*, vol. 9, no. 5, p. 105966, Oct. 2021, doi: 10.1016/J.JECE.2021.105966.

[21] H. Guo *et al.*, "A comprehensive insight into plasma-catalytic removal of antibiotic oxytetracycline based on graphene-TiO2-Fe3O4 nanocomposites," *Chem. Eng. J.*, vol. 425, p. 130614, Dec. 2021, doi: 10.1016/J.CEJ.2021.130614.

[22] G. Kesavan and S. Chen, "Manganese oxide anchored on carbon modified halloysite nanotubes: An electrochemical platform for the determination of chloramphenicol," *Colloids Surfaces A Physicochem. Eng. Asp.*, vol. 615, no. December 2020, p. 126243, 2021, doi: 10.1016/j.colsurfa.2021.126243.

[23] L. M. Bexfield, P. L. Toccalino, K. Belitz, W. T. Foreman, and E. T. Furlong, "Hormones and Pharmaceuticals in Groundwater Used As a Source of Drinking Water Across the United States," *Environ. Sci. Technol.*, vol. 53, no. 6, pp. 2950–2960, Mar. 2019, doi: 10.1021/ACS.EST.8B05592.

[24] X. Qu, P. J. J. Alvarez, and Q. Li, "Applications of nanotechnology in water and wastewater treatment," *Water Res.*, vol. 47, no. 12, pp. 3931–3946, 2013, doi: 10.1016/j.watres.2012.09.058.

[25] M. Gu, Q. Sui, U. Farooq, X. Zhang, Z. Qiu, and S. Lyu, "Degradation of phenanthrene in sulfate radical based oxidative environment by nZVI-PDA functionalized rGO catalyst," *Chem. Eng. J.*, vol. 354, pp. 541–552, Dec. 2018, doi: 10.1016/J.CEJ.2018.08.039.

[26] M. fang Li, Y. guo Liu, G. ming Zeng, N. Liu, and S. bo Liu, "Graphene and graphene-based nanocomposites used for antibiotics removal in water treatment: A review," *Chemosphere*, vol. 226, pp. 360–380, 2019, doi: 10.1016/j.chemosphere.2019.03.117.

[27] N. Ninwiwek, P. Hongsawat, P. Punyapalakul, and P. Prarat, "Removal of the antibiotic sulfamethoxazole from environmental water by mesoporous silica-magnetic graphene oxide nanocomposite technology: Adsorption characteristics, coadsorption and uptake mechanism," *Colloids Surfaces A Physicochem. Eng. Asp.*, vol. 580, p. 123716, Nov. 2019, doi: 10.1016/J.COLSURFA.2019.123716.

[28] O. Falyouna *et al.*, "Promotion of ciprofloxacin adsorption from contaminated solutions by oxalate modified nanoscale zerovalent iron particles," *J. Mol. Liq.*, vol. 359, p. 119323, Aug. 2022, doi: 10.1016/J.MOLLIQ.2022.119323.

[29] T. E. of E. Britannica, "Pharmaceutical industry | Definition, Overview, History,

Characteristics, Examples, & Facts | Britannica." https://www.britannica.com/technology/pharmaceutical-industry (accessed Mar. 28, 2023).

[30] T. E. of E. Britannica, "Pharmaceutical | therapeutic substance | Britannica." https://www.britannica.com/technology/pharmaceutical (accessed Mar. 29, 2023).

[31] T. K. Kasonga, M. A. A. Coetzee, I. Kamika, V. M. Ngole-Jeme, and M. N. Benteke Momba, "Endocrine-disruptive chemicals as contaminants of emerging concern in wastewater and surface water: A review," *J. Environ. Manage.*, vol. 277, p. 111485, Jan. 2021, doi: 10.1016/J.JENVMAN.2020.111485.

[32] A. Majumder, A. K. Gupta, P. S. Ghosal, and M. Varma, "A review on hospital wastewater treatment: A special emphasis on occurrence and removal of pharmaceutically active compounds, resistant microorganisms, and SARS-CoV-2," *J. Environ. Chem. Eng.*, vol. 9, no. 2, p. 104812, Apr. 2021, doi: 10.1016/J.JECE.2020.104812.

[33] N. H. Tran, M. Reinhard, and K. Y. H. Gin, "Occurrence and fate of emerging contaminants in municipal wastewater treatment plants from different geographical regions-a review," *Water Res.*, vol. 133, pp. 182–207, Apr. 2018, doi: 10.1016/J.WATRES.2017.12.029.

[34] S. K. Behera, H. W. Kim, J. E. Oh, and H. S. Park, "Occurrence and removal of antibiotics, hormones and several other pharmaceuticals in wastewater treatment plants of the largest industrial city of Korea," *Sci. Total Environ.*, vol. 409, no. 20, pp. 4351–4360, Sep. 2011, doi: 10.1016/J.SCITOTENV.2011.07.015.

[35] E. Koumaki, C. Noutsopoulos, D. Mamais, G. Fragkiskatos, and A. Andreadakis, "Fate of emerging contaminants in high-rate activated sludge systems," *Int. J. Environ. Res. Public Health*, vol. 18, no. 2, pp. 1–16, 2021, doi: 10.3390/ijerph18020400.

[36] Y. Cabeza, L. Candela, D. Ronen, and G. Teijon, "Monitoring the occurrence of emerging contaminants in treated wastewater and groundwater between 2008 and 2010. The Baix Llobregat (Barcelona, Spain)," *J. Hazard. Mater.*, vol. 239–240, pp. 32–39, Nov. 2012, doi: 10.1016/J.JHAZMAT.2012.07.032.

[37] J. L. Wilkinson *et al.*, "Pharmaceutical pollution of the world ' s rivers," vol. 119, no. 8, pp. 1–10, 2022, doi: 10.1073/pnas.2113947119/-/DCSupplemental.Published.

[38] "Antibiotics - NHS." https://www.nhs.uk/conditions/antibiotics/ (accessed Apr. 04,

2023).

[39] “Antibiotics: MedlinePlus.” https://medlineplus.gov/antibiotics.html (accessed Apr. 04, 2023).

[40] E. Baralla, M. P. Demontis, F. Dessì, and M. V. Varoni, “An overview of antibiotics as emerging contaminants: Occurrence in bivalves as biomonitoring organisms,” *Animals*, vol. 11, no. 11, pp. 1–17, 2021, doi: 10.3390/ani11113239.

[41] M. Bashimam and H. El-Zein, “Pharmaceutical cocrystal of antibiotic drugs: A comprehensive review,” *Heliyon*, vol. 8, no. 12, p. e11872, Dec. 2022, doi: 10.1016/J.HELIYON.2022.E11872.

[42] F. Lu and D. Astruc, “Nanomaterials for removal of toxic elements from water,” *Coord. Chem. Rev.*, vol. 356, pp. 147–164, Feb. 2018, doi: 10.1016/J.CCR.2017.11.003.

[43] A. P. Cuzziol Boccioni, G. García-Effron, P. M. Peltzer, and R. C. Lajmanovich, “Effect of glyphosate and ciprofloxacin exposure on enteric bacteria of tadpoles,” *Rev. Argent. Microbiol.*, Jan. 2023, doi: 10.1016/J.RAM.2022.08.004.

[44] F. Akram, M. Imtiaz, and I. ul Haq, “Emergent crisis of antibiotic resistance: A silent pandemic threat to 21st century,” *Microb. Pathog.*, vol. 174, p. 105923, Jan. 2023, doi: 10.1016/J.MICPATH.2022.105923.

[45] O. Falyouna *et al.*, “Synthesis of hybrid magnesium hydroxide/magnesium oxide nanorods [Mg(OH)2/MgO] for prompt and efficient adsorption of ciprofloxacin from aqueous solutions,” *J. Clean. Prod.*, vol. 342, p. 130949, Mar. 2022, doi: 10.1016/J.JCLEPRO.2022.130949.

[46] H. M. Hamadeen and E. A. Elkhatib, “New nanostructured activated biochar for effective removal of antibiotic ciprofloxacin from wastewater: Adsorption dynamics and mechanisms,” *Environ. Res.*, vol. 210, p. 112929, Jul. 2022, doi: 10.1016/J.ENVRES.2022.112929.

[47] S. Bin Zaman, M. A. Hussain, R. Nye, V. Mehta, K. T. Mamun, and N. Hossain, “A Review on Antibiotic Resistance: Alarm Bells are Ringing,” *Cureus*, vol. 9, no. 6, 2017, doi: 10.7759/cureus.1403.

[48] WHO, “Antibiotic resistance.” https://www.who.int/en/news-room/fact-sheets/detail/antibiotic-resistance (accessed Apr. 04, 2023).

[49] O. Falyouna, I. Maamoun, K. Bensaida, A. Tahara, Y. Sugihara, and O. Eljamal, “Encapsulation of iron nanoparticles with magnesium hydroxide shell for remarkable removal of ciprofloxacin from contaminated water,” *J. Colloid*

Interface Sci., vol. 605, pp. 813–827, Jan. 2022, doi: 10.1016/J.JCIS.2021.07.154.

[50] A. M. Chávez, F. J. Beltrán, J. López, F. Javier Rivas, and P. M. Álvarez, "On the importance of reactions in the proximity of the gas–water interface: Application to direct ozone reactions of antibiotics in water," *Chem. Eng. J.*, vol. 458, p. 141408, Feb. 2023, doi: 10.1016/J.CEJ.2023.141408.

[51] M. S. de Ilurdoz, J. J. Sadhwani, and J. V. Reboso, "Antibiotic removal processes from water & wastewater for the protection of the aquatic environment - a review," *J. Water Process Eng.*, vol. 45, p. 102474, Feb. 2022, doi: 10.1016/J.JWPE.2021.102474.

[52] C. A. Igwegbe, S. N. Oba, C. O. Aniagor, A. G. Adeniyi, and J. O. Ighalo, "Adsorption of ciprofloxacin from water: A comprehensive review," *J. Ind. Eng. Chem.*, vol. 93, pp. 57–77, Jan. 2021, doi: 10.1016/J.JIEC.2020.09.023.

[53] X. Wang, Y. Xie, W. Tong, W. Hu, Y. Wang, and Y. Zhang, "Photochemical degradation of chloramphenicol over jarosite/oxalate system: Performance and mechanism investigation," *J. Environ. Chem. Eng.*, vol. 9, no. 1, p. 104570, 2021, doi: 10.1016/j.jece.2020.104570.

[54] M. Yadav, V. Ganesan, R. Gupta, D. K. Yadav, and P. K. Sonkar, "Cobalt oxide nanocrystals anchored on graphene sheets for electrochemical determination of chloramphenicol," *Microchem. J.*, vol. 146, no. January, pp. 881–887, 2019, doi: 10.1016/j.microc.2019.02.025.

[55] L. M. Nguyen, N. T. T. Nguyen, T. T. T. Nguyen, T. T. Nguyen, D. T. C. Nguyen, and T. V. Tran, "Occurrence, toxicity and adsorptive removal of the chloramphenicol antibiotic in water: a review," *Environ. Chem. Lett.*, vol. 20, no. 3, pp. 1929–1963, 2022, doi: 10.1007/s10311-022-01416-x.

[56] H. Guo, Z. Li, Y. Zhang, N. Jiang, H. Wang, and J. Li, "Degradation of chloramphenicol by pulsed discharge plasma with heterogeneous Fenton process using Fe3O4 nanocomposites," *Sep. Purif. Technol.*, vol. 253, no. July, p. 117540, 2020, doi: 10.1016/j.seppur.2020.117540.

[57] C. Li *et al.*, "Degradation of chloramphenicol by chlorine and chlorine dioxide in a pilot-scale water distribution system," *Sep. Purif. Technol.*, vol. 211, no. October 2018, pp. 564–570, 2019, doi: 10.1016/j.seppur.2018.10.019.

[58] F. Görmez, Ö. Görmez, B. Gözmen, and D. Kalderis, "Degradation of chloramphenicol and metronidazole by electro-Fenton process using graphene oxide-Fe3O4 as heterogeneous catalyst," *J. Environ. Chem. Eng.*, vol. 7, no. 2, p.

102990, 2019, doi: 10.1016/j.jece.2019.102990.

[59] R. Gusain, N. Kumar, and S. S. Ray, “Recent advances in carbon nanomaterial-based adsorbents for water purification,” *Coord. Chem. Rev.*, vol. 405, p. 213111, Feb. 2020, doi: 10.1016/J.CCR.2019.213111.

[60] J. Lin *et al.*, “Removal of chloramphenicol antibiotics in natural and engineered water systems: Review of reaction mechanisms and product toxicity,” *Sci. Total Environ.*, vol. 850, p. 158059, Dec. 2022, doi: 10.1016/J.SCITOTENV.2022.158059.

[61] I. Amildon Ricardo, V. A. B. Paiva, C. E. S. Paniagua, and A. G. Trovó, “Chloramphenicol photo-Fenton degradation and toxicity changes in both surface water and a tertiary effluent from a municipal wastewater treatment plant at near-neutral conditions,” *Chem. Eng. J.*, vol. 347, no. April, pp. 763–770, 2018, doi: 10.1016/j.cej.2018.04.169.

[62] Y. fei Zhang *et al.*, “Strategies to enhance the reactivity of zero-valent iron for environmental remediation: A review,” *J. Environ. Manage.*, vol. 317, p. 115381, Sep. 2022, doi: 10.1016/J.JENVMAN.2022.115381.

[63] Y. Meng, X. Chen, D. Ai, T. Wei, Z. Fan, and B. Wang, “Sulfur-doped zero-valent iron supported on biochar for tetracycline adsorption and removal,” *J. Clean. Prod.*, vol. 379, no. P2, p. 134769, 2022, doi: 10.1016/j.jclepro.2022.134769.

[64] Y. Cheng, H. Dong, and T. Hao, “CaCO3 coated nanoscale zero-valent iron (nZVI) for the removal of chromium(VI) in aqueous solution,” *Sep. Purif. Technol.*, vol. 257, no. September 2020, p. 117967, 2021, doi: 10.1016/j.seppur.2020.117967.

[65] J. Xu, X. Liu, Z. Cao, W. Bai, Q. Shi, and Y. Yang, “Fast degradation, large capacity, and high electron efficiency of chloramphenicol removal by different carbon-supported nanoscale zerovalent iron,” *J. Hazard. Mater.*, vol. 384, p. 121253, Feb. 2020, doi: 10.1016/J.JHAZMAT.2019.121253.

[66] J. Yu, X. Hou, X. Hu, H. Yuan, J. Wang, and C. Chen, “Efficient degradation of chloramphenicol by zero-valent iron microspheres and new insights in mechanisms,” *Appl. Catal. B Environ.*, vol. 256, no. February, p. 117876, 2019, doi: 10.1016/j.apcatb.2019.117876.

[67] X. Liu *et al.*, “Insight into the kinetics and mechanism of removal of aqueous chlorinated nitroaromatic antibiotic chloramphenicol by nanoscale zero-valent iron,” *Chem. Eng. J.*, vol. 334, pp. 508–518, Feb. 2018, doi: 10.1016/J.CEJ.2017.10.060.

[68] K. Pandey, S. Sharma, and S. Saha, “Advances in design and synthesis of stabilized zero-valent iron nanoparticles for groundwater remediation,” *J. Environ. Chem. Eng.*, vol. 10, no. 3, p. 107993, Jun. 2022, doi: 10.1016/J.JECE.2022.107993.

[69] J. Qu *et al.*, “Green synthesis of hydrophilic activated carbon supported sulfide nZVI for enhanced Pb(II) scavenging from water: Characterization, kinetics, isotherms and mechanisms,” *J. Hazard. Mater.*, vol. 403, no. July 2020, p. 123607, 2021, doi: 10.1016/j.jhazmat.2020.123607.

[70] B. D. Yirsaw, M. Megharaj, Z. Chen, and R. Naidu, “Environmental application and ecological significance of nano-zero valent iron,” *J. Environ. Sci.*, vol. 44, pp. 88–98, Jun. 2016, doi: 10.1016/J.JES.2015.07.016.

[71] P. Wang, F. Fu, and T. Liu, “A review of the new multifunctional nano zero-valent iron composites for wastewater treatment: Emergence, preparation, optimization and mechanism,” *Chemosphere*, vol. 285, p. 131435, Dec. 2021, doi: 10.1016/J.CHEMOSPHERE.2021.131435.

[72] C. Yu, J. C. Shao, W. J. Sun, and X. N. Yu, “Treatment of lead contaminated water using synthesized nano-iron supported with bentonite/graphene oxide,” *Arab. J. Chem.*, vol. 13, no. 1, pp. 3474–3483, 2020, doi: 10.1016/j.arabjc.2018.11.019.

[73] E. C. Engineering, “Chemical Engineering Journal Effect of different sulfur precursors on efficient chromium (VI) removal by zeolite supporting sulfide nano zero-valent iron ZSM-5 Graphical Abstract,” no. Vi.

[74] R. Eljamal, O. Eljamal, A. M. E. Khalil, B. B. Saha, and N. Matsunaga, “Improvement of the chemical synthesis efficiency of nano-scale zero-valent iron particles,” *J. Environ. Chem. Eng.*, vol. 6, no. 4, pp. 4727–4735, Aug. 2018, doi: 10.1016/J.JECE.2018.06.069.

[75] I. Maamoun, R. Eljamal, O. Falyouna, K. Bensaida, Y. Sugihara, and O. Eljamal, “Insights into kinetics, isotherms and thermodynamics of phosphorus sorption onto nanoscale zero-valent iron,” *J. Mol. Liq.*, vol. 328, p. 115402, 2021, doi: 10.1016/j.molliq.2021.115402.

[76] M. Stefaniuk, P. Oleszczuk, and Y. S. Ok, “Review on nano zerovalent iron (nZVI): From synthesis to environmental applications,” *Chem. Eng. J.*, vol. 287, pp. 618–632, Mar. 2016, doi: 10.1016/J.CEJ.2015.11.046.

[77] X. Li and L. Liu, “Recent advances in nanoscale zero-valent iron/oxidant system as a treatment for contaminated water and soil,” *J. Environ. Chem. Eng.*, vol. 9, no. 5, p. 106276, Oct. 2021, doi: 10.1016/J.JECE.2021.106276.

[78] X. Peng *et al.*, “New insights into the activity of a biochar supported nanoscale zerovalent iron composite and nanoscale zero valent iron under anaerobic or aerobic conditions,” *RSC Adv.*, vol. 7, no. 15, pp. 8755–8761, 2017, doi: 10.1039/C6RA27256H.

[79] J. Suazo-Hernández *et al.*, “Synthesis and characterization of zeolite-based composites functionalized with nanoscale zero-valent iron for removing arsenic in the presence of selenium from water,” *J. Hazard. Mater.*, vol. 373, no. October 2018, pp. 810–819, 2019, doi: 10.1016/j.jhazmat.2019.03.125.

[80] H. Tang *et al.*, “Recent advances in nanoscale zero-valent iron-based materials: Characteristics, environmental remediation and challenges,” *J. Clean. Prod.*, vol. 319, p. 128641, Oct. 2021, doi: 10.1016/J.JCLEPRO.2021.128641.

[81] Q. Jiang *et al.*, “Graphene-like carbon sheet-supported nZVI for efficient atrazine oxidation degradation by persulfate activation,” *Chem. Eng. J.*, vol. 403, no. July 2020, p. 126309, 2021, doi: 10.1016/j.cej.2020.126309.

[82] Y. Hua *et al.*, “Effect of bicarbonate on aging and reactivity of nanoscale zerovalent iron (nZVI) toward uranium removal,” *Chemosphere*, vol. 201, pp. 603–611, 2018, doi: 10.1016/j.chemosphere.2018.03.041.

[83] H. Wu *et al.*, “Polyethylene glycol-stabilized nano zero-valent iron supported by biochar for highly efficient removal of Cr(VI),” *Ecotoxicol. Environ. Saf.*, vol. 188, p. 109902, Jan. 2020, doi: 10.1016/J.ECOENV.2019.109902.

[84] R. Xing, J. He, P. Hao, and W. Zhou, “Graphene oxide-supported nanoscale zero-valent iron composites for the removal of atrazine from aqueous solution,” *Colloids Surfaces A Physicochem. Eng. Asp.*, vol. 589, p. 124466, Feb. 2020, doi: 10.1016/J.COLSURFA.2020.124466.

[85] J. Zhang, Q. Zhu, and Z. Xing, “Preparation of new materials by ethylene glycol modification and Al(OH)3 coating NZVI to remove sulfides in water,” *J. Hazard. Mater.*, vol. 390, no. September 2019, 2020, doi: 10.1016/j.jhazmat.2020.122049.

[86] O. Eljamal, T. Shubair, A. Tahara, Y. Sugihara, and N. Matsunaga, “Iron based nanoparticles-zeolite composites for the removal of cesium from aqueous solutions,” *J. Mol. Liq.*, vol. 277, pp. 613–623, 2019, doi: 10.1016/j.molliq.2018.12.115.

[87] X. Li, L. Ai, and J. Jiang, “Nanoscale zerovalent iron decorated on graphene nanosheets for Cr(VI) removal from aqueous solution: Surface corrosion retard induced the enhanced performance,” *Chem. Eng. J.*, vol. 288, pp. 789–797, Mar.

2016, doi: 10.1016/J.CEJ.2015.12.022.

[88] X. Wang, A. Wang, M. Lu, and J. Ma, “Synthesis of magnetically recoverable Fe0/graphene-TiO2 nanowires composite for both reduction and photocatalytic oxidation of metronidazole,” *Chem. Eng. J.*, vol. 337, no. December 2017, pp. 372–384, 2018, doi: 10.1016/j.cej.2017.12.090.

[89] K. Liu, F. Li, J. Cui, S. Yang, and L. Fang, “Simultaneous removal of Cd(II) and As(III) by graphene-like biochar-supported zero-valent iron from irrigation waters under aerobic conditions: Synergistic effects and mechanisms,” *J. Hazard. Mater.*, vol. 395, p. 122623, Aug. 2020, doi: 10.1016/J.JHAZMAT.2020.122623.

[90] J. Li, M. Fan, M. Li, and X. Liu, “Cr(VI) removal from groundwater using double surfactant-modified nanoscale zero-valent iron (nZVI): Effects of materials in different status,” *Sci. Total Environ.*, vol. 717, p. 137112, 2020, doi: 10.1016/j.scitotenv.2020.137112.

[91] P. Li, D. Huang, J. Huang, J. Tang, P. Zhang, and F. Meng, “Development of magnetic porous carbon nano-fibers for application as adsorbents in the enrichment of trace Sudan dyes in foodstuffs,” *J. Chromatogr. A*, vol. 1625, 2020, doi: 10.1016/j.chroma.2020.461305.

[92] M. L. Tran, C. H. Nguyen, T. T. Van Tran, and R. S. Juang, “One-pot synthesis of bimetallic Pt/nZVI nanocomposites for enhanced removal of oxytetracycline: Roles of morphology changes and Pt catalysis,” *J. Taiwan Inst. Chem. Eng.*, vol. 111, pp. 130–140, 2020, doi: 10.1016/j.jtice.2020.05.001.

[93] G. Gopal, H. Sankar, C. Natarajan, and A. Mukherjee, “Tetracycline removal using green synthesized bimetallic nZVI-Cu and bentonite supported green nZVI-Cu nanocomposite: A comparative study,” *J. Environ. Manage.*, vol. 254, no. June 2019, p. 109812, 2020, doi: 10.1016/j.jenvman.2019.109812.

[94] I. Maamoun, O. Eljamal, T. Shubair, H. Noutsuka, B. B. Saha, and N. Matsunaga, “Integrating nano-scale zero valent iron (nZVI) in phosphorus removal from aqueous solution through porous media: packed-column experiment,” *Proc. Int. Exch. Innov. Conf. Eng. Sci.*, vol. 3, pp. 25–30, 2017.

[95] R. Yadav and C. K. Dixit, “Synthesis, characterization and prospective applications of nitrogen-doped graphene: A short review,” *J. Sci. Adv. Mater. Devices*, vol. 2, no. 2, pp. 141–149, Jun. 2017, doi: 10.1016/J.JSAMD.2017.05.007.

[96] X. Song, H. Zhang, Z. Bian, and H. Wang, “In situ electrogeneration and activation of H2O2 by atomic Fe catalysts for the efficient removal of chloramphenicol,” *J.*

Hazard. Mater., vol. 412, no. December 2020, p. 125162, 2021, doi: 10.1016/j.jhazmat.2021.125162.

[97] H. Gu, Y. Gao, M. Xiong, D. Zhang, W. Chen, and Z. Xu, "Removal of nitrobenzene from aqueous solution by graphene/biochar supported nanoscale zero-valent-iron: Reduction enhancement behavior and mechanism," *Sep. Purif. Technol.*, vol. 275, p. 119146, Nov. 2021, doi: 10.1016/J.SEPPUR.2021.119146.

[98] H. Dong *et al.*, "Stabilization of nanoscale zero-valent iron (nZVI) with modified biochar for Cr(VI) removal from aqueous solution," *J. Hazard. Mater.*, vol. 332, pp. 79–86, Jun. 2017, doi: 10.1016/J.JHAZMAT.2017.03.002.

[99] O. J. Ajala, J. O. Tijani, M. T. Bankole, and A. S. Abdulkareem, "A critical review on graphene oxide nanostructured material: Properties, Synthesis, characterization and application in water and wastewater treatment," *Environ. Nanotechnology, Monit. Manag.*, vol. 18, p. 100673, Dec. 2022, doi: 10.1016/J.ENMM.2022.100673.

[100] C. Li, X. Chen, L. Shen, and N. Bao, "Revisiting the Oxidation of Graphite: Reaction Mechanism, Chemical Stability, and Structure Self-Regulation," *Cite This ACS Omega*, vol. 5, p. 3404, 2020, doi: 10.1021/acsomega.9b03633.

[101] R. Ghorbani, S. Behrangi, H. Aghajani, A. Taghizadeh Tabrizi, and N. Abdian, "Application of synthesized porous 3D graphene structure for electrochemical hydrogen storage," *Mater. Sci. Eng. B*, vol. 268, p. 115139, Jun. 2021, doi: 10.1016/J.MSEB.2021.115139.

[102] S. Singh *et al.*, "Novel insights into graphene oxide-based adsorbents for remediation of hazardous pollutants from aqueous solutions: A comprehensive review," *J. Mol. Liq.*, vol. 369, p. 120821, Jan. 2023, doi: 10.1016/J.MOLLIQ.2022.120821.

[103] B. Y. Z. Hiew *et al.*, "Adsorptive removal of diclofenac by graphene oxide: Optimization, equilibrium, kinetic and thermodynamic studies," *J. Taiwan Inst. Chem. Eng.*, vol. 98, pp. 150–162, 2019, doi: 10.1016/j.jtice.2018.07.034.

[104] D. C. Marcano *et al.*, "Improved synthesis of graphene oxide," *ACS Nano*, vol. 4, no. 8, pp. 4806–4814, 2010, doi: 10.1021/nn1006368.

[105] G. Wang, B. Wang, J. Park, J. Yang, X. Shen, and J. Yao, "Synthesis of enhanced hydrophilic and hydrophobic graphene oxide nanosheets by a solvothermal method," *Carbon N. Y.*, vol. 47, no. 1, pp. 68–72, 2009, doi: 10.1016/j.carbon.2008.09.002.

[106] Z. Niu, G. K. Murakonda, R. Jarubula, and M. Dai, “Fabrication of Graphene oxide-Fe3O4 nanocomposites for application in bone regeneration and treatment of leukemia,” *J. Drug Deliv. Sci. Technol.*, vol. 63, no. 219, p. 102412, 2021, doi: 10.1016/j.jddst.2021.102412.

[107] P. Arabkhani, H. Javadian, A. Asfaram, and M. Ateia, “Decorating graphene oxide with zeolitic imidazolate framework (ZIF-8) and pseudo-boehmite offers ultra-high adsorption capacity of diclofenac in hospital effluents,” *Chemosphere*, vol. 271, p. 129610, 2021, doi: 10.1016/j.chemosphere.2021.129610.

[108] W. Peng, H. Li, Y. Liu, and S. Song, “A review on heavy metal ions adsorption from water by graphene oxide and its composites,” *J. Mol. Liq.*, vol. 230, pp. 496–504, 2017, doi: 10.1016/j.molliq.2017.01.064.

[109] T. Liu, N. Graham, and W. Yu, “Evaluation of a novel composite chitosan-graphene oxide membrane for NOM removal during water treatment,” *J. Environ. Chem. Eng.*, vol. 9, no. 4, p. 105716, 2021, doi: 10.1016/j.jece.2021.105716.

[110] X. Shan, X. Guo, Y. Yin, Y. Miao, and H. Dong, “Surface modification of graphene oxide by goethite with enhanced tylosin photocatalytic activity under visible light irradiation,” *Colloids Surfaces A Physicochem. Eng. Asp.*, vol. 520, pp. 420–427, 2017, doi: 10.1016/j.colsurfa.2017.01.077.

[111] M. Minale, Z. Gu, A. Guadie, D. M. Kabtamu, Y. Li, and X. Wang, “Application of graphene-based materials for removal of tetracyclines using adsorption and photocatalytic-degradation: A review,” *J. Environ. Manage.*, vol. 276, no. August, p. 111310, 2020, doi: 10.1016/j.jenvman.2020.111310.

[112] D. R. Dreyer, S. Park, C. W. Bielawski, and R. S. Ruoff, “The chemistry of graphene oxide,” *Chem. Soc. Rev.*, vol. 39, no. 1, pp. 228–240, 2010, doi: 10.1039/b917103g.

[113] M. F. Idham, “Antibiotics Removal from Aqueous Environments : A Mini Review on Graphene Oxide-based Nanomaterials Application,” *Proc. Int. Exch. Innov. Conf. Eng. Sci.*, vol. 8, pp. 340–346, 2022, doi: https://doi.org/10.5109/5909114.

[114] X. Liu *et al.*, “Graphene oxide-based materials for efficient removal of heavy metal ions from aqueous solution: A review,” *Environ. Pollut.*, vol. 252, pp. 62–73, 2019, doi: 10.1016/j.envpol.2019.05.050.

[115] M. li Cao, Y. Li, H. Yin, and S. Shen, “Functionalized graphene nanosheets as absorbent for copper (II) removal from water,” *Ecotoxicol. Environ. Saf.*, vol. 173, no. February, pp. 28–36, 2019, doi: 10.1016/j.ecoenv.2019.02.011.

[116] Y. A. R. Lebron *et al.*, "Graphene oxide for efficient treatment of real contaminated water by mining tailings: Metal adsorption studies to Paraopeba river and risk assessment," *Chem. Eng. J. Adv.*, vol. 2, no. July, p. 100017, 2020, doi: 10.1016/j.ceja.2020.100017.

[117] L. Han *et al.*, "Graphene oxide-induced formation of a boron-doped iron oxide shell on the surface of NZVI for enhancing nitrate removal," *Chemosphere*, vol. 252, 2020, doi: 10.1016/j.chemosphere.2020.126496.

[118] Y. Sun, Y. Yang, M. Yang, F. Yu, and J. Ma, "Response surface methodological evaluation and optimization for adsorption removal of ciprofloxacin onto graphene hydrogel," *J. Mol. Liq.*, vol. 284, pp. 124–130, 2019, doi: 10.1016/j.molliq.2019.03.118.

[119] R. Yuan, J. Yuan, Y. Wu, L. Chen, H. Zhou, and J. Chen, "Efficient synthesis of graphene oxide and the mechanisms of oxidation and exfoliation," *Appl. Surf. Sci.*, vol. 416, pp. 868–877, 2017, doi: 10.1016/j.apsusc.2017.04.181.

[120] R. Muzyka, M. Kwoka, Ł. Smędowski, N. Díez, and G. Gryglewicz, "Oxidation of graphite by different modified Hummers methods," *New Carbon Mater.*, vol. 32, no. 1, pp. 15–20, Feb. 2017, doi: 10.1016/S1872-5805(17)60102-1.

[121] H. L. F., C. P. Tan, Z. R.M., and N. H. Nur, "Effect of sonication time and heat treatment on the structural and physical properties of chitosan/graphene oxide nanocomposite films," *Food Packag. Shelf Life*, vol. 28, no. April 2020, p. 100663, 2021, doi: 10.1016/j.fpsl.2021.100663.

[122] A. Arabpour, S. Dan, and H. Hashemipour, "Preparation and optimization of novel graphene oxide and adsorption isotherm study of methylene blue," *Arab. J. Chem.*, vol. 14, no. 3, p. 103003, Mar. 2021, doi: 10.1016/j.arabjc.2021.103003.

[123] M. J. Yoo and H. B. Park, "Effect of hydrogen peroxide on properties of graphene oxide in Hummers method," *Carbon N. Y.*, vol. 141, pp. 515–522, 2019, doi: 10.1016/j.carbon.2018.10.009.

[124] O. Akhavan and E. Ghaderi, "Photocatalytic Reduction of Graphene Oxide Nanosheets on TiO2 Thin Film for Photoinactivation of Bacteria in Solar Light Irradiation," *J. Phys. Chem. C*, vol. 113, no. 47, pp. 20214–20220, Oct. 2009, doi: 10.1021/jp906325q.

[125] N. Nirmala *et al.*, "Removal of toxic metals from wastewater environment by graphene-based composites: A review on isotherm and kinetic models, recent trends, challenges and future directions," *Sci. Total Environ.*, vol. 840, p. 156564,

Sep. 2022, doi: 10.1016/J.SCITOTENV.2022.156564.

[126] M. Z. Kassaee, E. Motamedi, and M. Majdi, “Magnetic Fe3O4-graphene oxide/polystyrene: Fabrication and characterization of a promising nanocomposite,” *Chem. Eng. J.*, vol. 172, no. 1, pp. 540–549, 2011, doi: 10.1016/j.cej.2011.05.093.

[127] R. Eljamal, I. Maamoun, K. Bensaida, G. Yilmaz, Y. Sugihara, and O. Eljamal, “A novel method to improve methane generation from waste sludge using iron nanoparticles coated with magnesium hydroxide,” *Renew. Sustain. Energy Rev.*, vol. 158, p. 112192, Apr. 2022, doi: 10.1016/J.RSER.2022.112192.

[128] I. Maamoun, O. Eljamal, R. Eljamal, O. Falyouna, and Y. Sugihara, “Promoting aqueous and transport characteristics of highly reactive nanoscale zero valent iron via different layered hydroxide coatings,” *Appl. Surf. Sci.*, vol. 506, no. October 2019, p. 145018, 2020, doi: 10.1016/j.apsusc.2019.145018.

[129] H. Adel Niaei and M. Rostamizadeh, “Adsorption of metformin from an aqueous solution by Fe-ZSM-5 nano-adsorbent: Isotherm, kinetic and thermodynamic studies,” *J. Chem. Thermodyn.*, vol. 142, p. 106003, 2020, doi: 10.1016/j.jct.2019.106003.

[130] N. A. Ahammad, M. A. Zulkifli, M. A. Ahmad, B. H. Hameed, and A. T. Mohd Din, “Desorption of chloramphenicol from ordered mesoporous carbon-alginate beads: Effects of operating parameters, and isotherm, kinetics, and regeneration studies,” *J. Environ. Chem. Eng.*, vol. 9, no. 1, p. 105015, 2021, doi: 10.1016/j.jece.2020.105015.

[131] M. F. Idham, O. Falyouna, R. Eljamal, I. Maamoun, and O. Eljamal, “Chloramphenicol removal from water by various precursors to enhance graphene oxide–iron nanocomposites,” *J. Water Process Eng.*, vol. 50, no. October, p. 103289, 2022, doi: 10.1016/j.jwpe.2022.103289.

[132] A. M. Dimiev and J. M. Tour, “Mechanism of Graphene Oxide Formation,” *ACS Nano*, vol. 8, no. 3, pp. 3060–3068, Mar. 2014, doi: 10.1021/nn500606a.

[133] B. Y. Z. Hiew *et al.*, “Review on synthesis of 3D graphene-based configurations and their adsorption performance for hazardous water pollutants,” *Process Saf. Environ. Prot.*, vol. 116, pp. 262–286, 2018, doi: 10.1016/j.psep.2018.02.010.

[134] M. fang Li *et al.*, “Cu(II)-influenced adsorption of ciprofloxacin from aqueous solutions by magnetic graphene oxide/nitrilotriacetic acid nanocomposite: Competition and enhancement mechanisms,” *Chem. Eng. J.*, vol. 319, pp. 219–

228, Jul. 2017, doi: 10.1016/J.CEJ.2017.03.016.

[135] H. Chen, B. Gao, and H. Li, “Removal of sulfamethoxazole and ciprofloxacin from aqueous solutions by graphene oxide,” *J. Hazard. Mater.*, vol. 282, pp. 201–207, 2015, doi: 10.1016/j.jhazmat.2014.03.063.

[136] C. H. Nguyen, M. L. Tran, T. T. Van Tran, and R. S. Juang, “Efficient removal of antibiotic oxytetracycline from water by Fenton-like reactions using reduced graphene oxide-supported bimetallic Pd/nZVI nanocomposites,” *J. Taiwan Inst. Chem. Eng.*, vol. 000, pp. 1–10, 2021, doi: 10.1016/j.jtice.2021.02.001.

[137] S. Jamali Alyani, A. Ebrahimian Pirbazari, F. Esmaeili Khalilsaraei, N. Asasian Kolur, and N. Gilani, “Growing Co-doped TiO2 nanosheets on reduced graphene oxide for efficient photocatalytic removal of tetracycline antibiotic from aqueous solution and modeling the process by artificial neural network,” *J. Alloys Compd.*, vol. 799, pp. 169–182, 2019, doi: 10.1016/j.jallcom.2019.05.175.

[138] Y. Gao *et al.*, “Adsorption and removal of tetracycline antibiotics from aqueous solution by graphene oxide,” *J. Colloid Interface Sci.*, vol. 368, no. 1, pp. 540–546, 2012, doi: 10.1016/j.jcis.2011.11.015.

[139] O. Eljamal, J. Okawauchi, K. Hiramatsu, and M. Harada, “Phosphorus sorption from aqueous solution using natural materials,” *Environ. Earth Sci.*, vol. 68, no. 3, pp. 859–863, 2013, doi: 10.1007/s12665-012-1789-6.

[140] N. A. Husin, N. M. Hashim, N. Yahaya, M. Miskam, M. Raoov, and N. N. M. Zain, “Exploring magnetic particle surface embedded with imidazole-based deep eutectic solvent for diclofenac removal from pharmaceutical wastewater samples,” *J. Mol. Liq.*, vol. 332, p. 115809, 2021, doi: 10.1016/j.molliq.2021.115809.

[141] Y. Yang, L. Xu, and J. Wang, “An enhancement of singlet oxygen generation from dissolved oxygen activated by three-dimensional graphene wrapped nZVI-doped amorphous Al species for chloramphenicol removal in the Fenton-like system,” *Chem. Eng. J.*, vol. 425, p. 131497, Dec. 2021, doi: 10.1016/J.CEJ.2021.131497.

[142] H. Deb *et al.*, “Kinetics & dynamic studies of dye adsorption by porous graphene nano-adsorbent for facile toxic wastewater remediation,” *J. Water Process Eng.*, vol. 47, p. 102818, Jun. 2022, doi: 10.1016/J.JWPE.2022.102818.

[143] T. Shubair, O. Eljamal, A. M. E. Khalil, A. Tahara, and N. Matsunaga, “Novel application of nanoscale zero valent iron and bimetallic nano-Fe/Cu particles for the treatment of cesium contaminated water,” *J. Environ. Chem. Eng.*, vol. 6, no. 4, pp. 4253–4264, Aug. 2018, doi: 10.1016/J.JECE.2018.06.015.

[144] M. S. Nas, M. H. Calimli, H. Burhan, M. Yılmaz, S. D. Mustafov, and F. Sen, “Synthesis, characterization, kinetics and adsorption properties of Pt-Co@GO nano-adsorbent for methylene blue removal in the aquatic mediums using ultrasonic process systems,” *J. Mol. Liq.*, vol. 296, 2019, doi: 10.1016/j.molliq.2019.112100.

[145] Q. Bin *et al.*, “Superior trichloroethylene removal from water by sulfide-modified nanoscale zero-valent iron/graphene aerogel composite,” *J. Environ. Sci.*, vol. 88, pp. 90–102, Feb. 2020, doi: 10.1016/J.JES.2019.08.011.

[146] J. Romero-González, J. R. Peralta-Videa, E. Rodriíguez, S. L. Ramirez, and J. L. Gardea-Torresdey, “Determination of thermodynamic parameters of Cr(VI) adsorption from aqueous solution onto Agave lechuguilla biomass,” *J. Chem. Thermodyn.*, vol. 37, no. 4, pp. 343–347, Apr. 2005, doi: 10.1016/J.JCT.2004.09.013.

[147] H. Patel, “Review on solvent desorption study from exhausted adsorbent,” *J. Saudi Chem. Soc.*, vol. 25, no. 8, p. 101302, Aug. 2021, doi: 10.1016/J.JSCS.2021.101302.

[148] D. Lu *et al.*, “Adsorption and desorption behaviors of antibiotic ciprofloxacin on functionalized spherical MCM-41 for water treatment,” *J. Clean. Prod.*, vol. 264, p. 121644, Aug. 2020, doi: 10.1016/J.JCLEPRO.2020.121644.

[149] F. Y. Kong, Y. Luo, J. W. Zhang, J. Y. Wang, W. W. Li, and W. Wang, “Facile synthesis of reduced graphene oxide supported Pt-Pd nanocubes with enhanced electrocatalytic activity for chloramphenicol determination,” *J. Electroanal. Chem.*, vol. 781, pp. 389–394, 2016, doi: 10.1016/j.jelechem.2016.06.018.

[150] Y. Yang, L. Xu, W. Li, W. Fan, S. Song, and J. Yang, “Adsorption and degradation of sulfadiazine over nanoscale zero-valent iron encapsulated in three-dimensional graphene network through oxygen-driven heterogeneous Fenton-like reactions,” *Appl. Catal. B Environ.*, vol. 259, no. July, p. 118057, 2019, doi: 10.1016/j.apcatb.2019.118057.

[151] A. Romero, M. P. Lavin-Lopez, L. Sanchez-Silva, J. L. Valverde, and A. Paton-Carrero, “Comparative study of different scalable routes to synthesize graphene oxide and reduced graphene oxide,” *Mater. Chem. Phys.*, vol. 203, pp. 284–292, 2018, doi: 10.1016/j.matchemphys.2017.10.013.

[152] Q. T. Ain, S. H. Haq, A. Alshammari, M. A. Al-Mutlaq, and M. N. Anjum, “The systemic effect of PEG-nGO-induced oxidative stress in vivo in a rodent model,”

Beilstein J. Nanotechnol., vol. 10, pp. 901–911, 2019, doi: 10.3762/BJNANO.10.91.

[153] A. Razaq, F. Bibi, X. Zheng, R. Papadakis, S. H. M. Jafri, and H. Li, "Review on Graphene-, Graphene Oxide-, Reduced Graphene Oxide-Based Flexible Composites: From Fabrication to Applications," *Materials (Basel).*, vol. 15, no. 3, 2022, doi: 10.3390/ma15031012.

[154] H. Karimi-Maleh *et al.*, "The role of magnetite/graphene oxide nano-composite as a high-efficiency adsorbent for removal of phenazopyridine residues from water samples, an experimental/theoretical investigation," *J. Mol. Liq.*, vol. 298, 2020, doi: 10.1016/j.molliq.2019.112040.

[155] A. Ahmad *et al.*, "Graphene oxide selenium nanorod composite as a stable electrode material for energy storage devices," *Appl. Nanosci.*, vol. 10, no. 4, pp. 1243–1255, 2020, doi: 10.1007/s13204-019-01204-0.

[156] Y. Yang, L. Xu, H. Shen, and J. Wang, "Construction of three-dimensional reduced graphene oxide wrapped nZVI doped with Al2O3 as the ternary Fenton-like catalyst: Optimization, characterization and catalytic mechanism," *Sci. Total Environ.*, vol. 780, p. 146576, Aug. 2021, doi: 10.1016/J.SCITOTENV.2021.146576.

[157] M. Gu, Q. Sui, U. Farooq, X. Zhang, Z. Qiu, and S. Lyu, "Enhanced degradation of trichloroethylene in oxidative environment by nZVI/PDA functionalized rGO catalyst," *J. Hazard. Mater.*, vol. 359, pp. 157–165, Oct. 2018, doi: 10.1016/J.JHAZMAT.2018.07.013.

[158] C. H. Nguyen, M. L. Tran, T. T. Van Tran, and R. S. Juang, "Efficient removal of antibiotic oxytetracycline from water by Fenton-like reactions using reduced graphene oxide-supported bimetallic Pd/nZVI nanocomposites," *J. Taiwan Inst. Chem. Eng.*, vol. 119, pp. 80–89, Feb. 2021, doi: 10.1016/J.JTICE.2021.02.001.

[159] H. Xu, Y. Zhang, J. Li, Q. Hao, X. Li, and F. Liu, "Heterogeneous activation of peroxymonosulfate by a biochar-supported Co3O4 composite for efficient degradation of chloramphenicols," *Environ. Pollut.*, vol. 257, p. 113610, 2020, doi: 10.1016/j.envpol.2019.113610.

[160] G. Wu *et al.*, "Removal of chloramphenicol by sulfide-modified nanoscale zero-valent iron activated persulfate: Performance, salt resistance, and reaction mechanisms," *Chemosphere*, vol. 286, p. 131876, Jan. 2022, doi: 10.1016/J.CHEMOSPHERE.2021.131876.

[161] Z. Zhang *et al.*, "Combining ferrate(VI) with thiosulfate to oxidize chloramphenicol: Influencing factors and degradation mechanism," *J. Environ. Chem. Eng.*, vol. 9, no. 1, p. 104625, 2021, doi: 10.1016/j.jece.2020.104625.

[162] Y. Wu, Q. Yue, Z. Ren, and B. Gao, "Immobilization of nanoscale zero-valent iron particles (nZVI) with synthesized activated carbon for the adsorption and degradation of Chloramphenicol (CAP)," *J. Mol. Liq.*, vol. 262, pp. 19–28, 2018, doi: 10.1016/j.molliq.2018.04.032.

[163] F. Yu, S. Sun, S. Han, J. Zheng, and J. Ma, "Adsorption removal of ciprofloxacin by multi-walled carbon nanotubes with different oxygen contents from aqueous solutions," *Chem. Eng. J.*, vol. 285, pp. 588–595, 2016, doi: 10.1016/j.cej.2015.10.039.

[164] N. Magesh, A. A. Renita, R. Siva, N. Harirajan, and A. Santhosh, "Adsorption behavior of fluoroquinolone(ciprofloxacin) using zinc oxide impregnated activated carbon prepared from jack fruit peel: Kinetics and isotherm studies," *Chemosphere*, vol. 290, p. 133227, Mar. 2022, doi: 10.1016/J.CHEMOSPHERE.2021.133227.

[165] A. B. Azzam, Y. A. Tokhy, F. M. El Dars, and A. A. Younes, "Construction of porous biochar decorated with NiS for the removal of ciprofloxacin antibiotic from pharmaceutical wastewaters," *J. Water Process Eng.*, vol. 49, p. 103006, Oct. 2022, doi: 10.1016/J.JWPE.2022.103006.

[166] L. Chen, T. Yuan, R. Ni, Q. Yue, and B. Gao, "Multivariate optimization of ciprofloxacin removal by polyvinylpyrrolidone stabilized NZVI/Cu bimetallic particles," *Chem. Eng. J.*, vol. 365, no. February, pp. 183–192, 2019, doi: 10.1016/j.cej.2019.02.051.

[167] C. Tan, Y. Dong, D. Fu, N. Gao, J. Ma, and X. Liu, "Chloramphenicol removal by zero valent iron activated peroxymonosulfate system: Kinetics and mechanism of radical generation," *Chem. Eng. J.*, vol. 334, pp. 1006–1015, Feb. 2018, doi: 10.1016/J.CEJ.2017.10.020.